Stellar Dynamical Measurements of Supermassive Black Hole Masses and Implications for Host Galaxy Demographics

by

Jacob Pilawa

A dissertation submitted in partial satisfaction of the

requirements for the degree of

Doctor of Philosophy

in

Astrophysics

in the

Graduate Division

of the

University of California, Berkeley

Committee in charge:

Professor Chung-Pei Ma, Chair
Professor Daniel Weisz
Professor Daniel Kasen

Summer 2026

Stellar Dynamical Measurements of Supermassive Black Hole Masses and Implications for Host Galaxy Demographics

Abstract

Stellar Dynamical Measurements of Supermassive Black Hole Masses and Implications for Host Galaxy Demographics

by

Jacob Pilawa

Doctor of Philosophy in Astrophysics

University of California, Berkeley

Professor Chung-Pei Ma, Chair

Supermassive black holes are found at the centers of massive galaxies, and their masses are observed to correlate with properties of their hosts. These empirical relations connect physical scales that differ by many orders of magnitude and provide important constraints on the joint evolution of black holes and galaxies. The most massive black holes in the local Universe are especially important for calibrating these relations, but they are also among the most difficult to measure. Their host galaxies are rare, spatially extended, and often structurally complex, requiring detailed observations and flexible dynamical models to separate the mass of the central black hole from the stellar and dark matter components of the galaxy.

This dissertation presents new measurements and tests of supermassive black hole masses in nearby massive elliptical galaxies, with an emphasis on using triaxial Schwarzschild orbit models. These models are needed because the most massive early-type galaxies often show photometric and kinematic signatures of intrinsically non-axisymmetric structure. The triaxial Schwarzschild orbit modeling approach is flexible enough to represent such shapes by building the stellar distribution function from a weighted library of stellar trajectories. Within that framework, the central black hole, stellar mass, dark matter, orbital structure, and intrinsic galaxy shape can be constrained simultaneously.

The first part of this dissertation applies triaxial orbit modeling to the massive elliptical galaxy NGC 2693. This chapter combines *HST* imaging of the stellar light distribution with spatially resolved stellar kinematics from integral-field spectroscopy, covering both the region near the black hole and the extended stellar halo. NGC 2693 appears close to axisymmetric in several projected properties, but the best-fitting dynamical models indicate that it is intrinsically triaxial. Comparisons with axisymmetric orbit models and Jeans models show how assumptions about intrinsic shape can affect the inferred black hole mass and motivate the use of more general dynamical models for massive early-type galaxies.

The second part of this dissertation tests the reliability of the triaxial Schwarzschild modeling framework using simulated galaxy observations. I generate mock kinematic datasets for a suite of triaxial galaxy models with known mass components and intrinsic shapes, then analyze them with the same parameter inference machinery used for real galaxies. These tests show that the modeling framework can accurately recover black hole masses, stellar mass-to-light ratios, dark matter content, intrinsic shapes, and internal orbital structures from realistic mock data. I also examine whether explicit model-complexity penalties improve the parameter inference and find that, for these triaxial tests, the standard likelihood-based approach already recovers the input galaxy properties well.

The third part of this dissertation applies triaxial stellar-dynamical modeling to NGC 315, a massive radio galaxy with an existing black hole mass measurement from CO gas dynamics. Using spatially resolved stellar kinematics from the MASSIVE survey, this chapter provides an independent stellar-dynamical measurement of the black hole mass and finds that the galaxy is intrinsically triaxial. NGC 315 is therefore an important cross-check between two major approaches to black hole mass measurement: modeling the motions of stars and modeling the motions of molecular gas. A comparison with the small sample of galaxies that have both kinds of measurements shows no statistically significant offset between the two methods with the data currently available.

The final part of this dissertation turns from individual dynamical measurements to black hole demographics across the sky. I construct a large low-redshift galaxy catalog by combining WISExSuperCOSMOS and 2MPZ, using WISE mid-infrared photometry and photometric redshifts to estimate homogeneous stellar masses for the entire sample. These stellar masses are then connected to inferred supermassive black hole masses through black hole–host-galaxy scaling relations. The resulting catalog is designed to support studies of the local black hole mass function and to help identify candidate host galaxies for supermassive black hole binaries detected by pulsar timing arrays. Together, the work in this dissertation improves both direct black hole mass measurements in individual massive galaxies and population-level estimates of the black holes most relevant for the nanohertz gravitational-wave sky.

To my family and friends

Contents

List of Figures

List of Tables

Acknowledgments

I would like to start by thanking my advisor, Professor Chung-Pei Ma. I am immensely grateful for the support, patience, guidance, and knowledge you have provided me over the last six years. You have helped me grow so much as both a scientist and as a person, and I will continue to hold your wisdom and advice near as I start the next chapter of my life. Thank you as well to Professors Daniel Weisz and Daniel Kasen for serving on both my qualifying exam and dissertation committees, and for your valuable feedback and support throughout my time in graduate school.

I have had the pleasure to work with and learn from a number of collaborators and co-authors during my time in graduate school, including Professor Jonelle Walsh, Professor Jenny Greene, and Professor John Blakeslee. I am also particularly thankful to Emily Liepold and Matthew Quenneville for useful discussions – about both research and life – throughout the last six years.

I truly would not be where I'm at today without the support of the many teachers and mentors I have had throughout the years. Thank you in particular to Professor Karen Harpp, Professor Tom Balonek, Professor Jonathan Levine, Professor Comsin Ilie, Professor Daniel Dale, Father Larry Ober, Justin Shaw, and George Valley for believing in me and inspiring me to pursue my dreams.

Thank you to my friends, in particular Pat and Jacob, for helping me make it through the high-highs and low-lows of the last six (actually, nearly fourteen at this point) years. The time we've shared together, including late night calls on Discord and Skype, have meant more to me than you will ever know.

Thank you to my family – Dad, Kim, Kayley, Douglas, Sasha, Eva, Wyatt, Carol, and Neil. You have all made so many sacrifices to get me to this point, and I am grateful beyond words for your unconditional love and support. I am so happy to be able to celebrate this with you all, and I know Neil is here with us celebrating, too.

And lastly, thank you to Hannah. You have been there with me and for me every single step of the way. So many difficult days were made so much easier knowing that I could come home to your comfort and love. I wouldn't want anyone else by my side.

Chapter 1

Introduction

Over the last several decades, observations of nearby galaxies have shown that supermassive black holes (SMBHs) are a normal, perhaps nearly ubiquitous, component of the centers of galaxies. The evidence now spans many complementary regimes: the resolved stellar orbits around Sagittarius A* in the Milky Way, maser and gas dynamics in nearby galaxies, stellar dynamical measurements in early-type galaxies, and event-horizon-scale imaging of M87* and Sagittarius A* [115, 54, 55, 175]. Although the black hole dominates the gravitational potential only within a small central region, SMBH masses are observed to correlate strongly with properties of the much larger host galaxy. The most widely used examples include the $M_{\rm BH}$–σ relation, which connects black hole mass to stellar velocity dispersion, and the $M_{\rm BH}$–$M_{\rm bulge}$ and $M_{\rm BH}$–$L_{\rm bulge}$ relations, which connect black hole mass to the stellar mass and luminosity of the host galaxy [60, 63, 116, 75, 118, 93, 151].

These empirical relations are striking because they link physical scales that differ by many orders of magnitude. The central black hole is dynamically important inside a sphere of influence of order

$$r_{\rm SOI} \equiv \frac{GM_{\rm BH}}{\sigma^2}, \tag{1.1}$$

while the host galaxy correlations involve stellar motions, light profiles, and masses measured over kiloparsec scales. This connection points to a coupled history between SMBHs and their host galaxies, but both the physical origin of the relations and their exact amplitude and slope remain uncertain. This uncertainty is greatest at the high-mass end, where the most massive black holes are intrinsically rare, their host galaxies often exhibit diffuse central light profiles and complex structures, and robust mass measurements require both demanding observations and computationally expensive dynamical modeling.

Several physical arguments help explain why such large-scale correlations might arise. Broadly, these arguments connect SMBH growth either to the regulation of gas in the host galaxy or to the accumulated assembly history of the galaxy and its black hole. In the first picture, the black hole and bulge grow from a common gas supply, and the energy or momentum released by accretion can affect how much gas remains available for further star formation and black hole growth. In feedback-regulated models, accretion continues until

radiation, winds, or jets inject enough energy or momentum into the surrounding gas to compete with the binding energy of the bulge. This connects the final black hole mass to the depth of the host potential and can produce scaling with velocity dispersion and bulge mass [164, 91, 93].

Galaxy merging provides a complementary route. Repeated mergers add black hole mass and stellar mass together, and statistical averaging can tighten an initially broad black-hole–galaxy mass relation [131]. This process is especially relevant for massive elliptical galaxies, whose late growth is often associated with dry mergers that add mass to the galaxy without much new star formation. In such systems, stellar mass and luminosity may continue to grow while velocity dispersion evolves more slowly, so the high-mass end need not follow a simple extrapolation of the relations measured at lower masses. Additional dynamical measurements, particularly for the most massive nearby galaxies, are therefore needed to determine the slopes, scatter, and possible curvature of the scaling relations and to clarify what aspects of galaxy evolution they actually trace.

The high-mass local population is also becoming increasingly important beyond traditional galaxy dynamics. Pulsar timing arrays (PTAs) are increasingly sensitive to nanohertz gravitational waves, a frequency range where inspiraling SMBH binaries are expected to be key sources. Recent PTA results have reported evidence for a stochastic gravitational-wave background and have begun to constrain individual binary SMBH signals [1, 2]. The nearest and most massive galaxies are natural places to search for the loudest binaries, so accurate black hole demographics support both galaxy-evolution studies and gravitational-wave source identification.

1.1 Photometric Observations of Galaxies

Photometry is the most direct observational entry point into the structure of a galaxy. At the broadest level, photometric imaging measures the amount of light emitted by a galaxy within a chosen wavelength range. If the distance to the galaxy is known, that flux can be converted into a luminosity, and the luminosity can be related to stellar mass through a stellar mass-to-light ratio. Even this relatively simple measurement is already central to black hole studies, because total luminosities and stellar masses are among the host-galaxy properties that enter SMBH scaling relations. Photometric quantities also underlie several classical galaxy relations, including the Kormendy relation between effective radius and surface brightness, the Faber–Jackson relation between luminosity and velocity dispersion, and the Fundamental Plane connecting size, surface brightness, and stellar velocity dispersion [92, 57, 46].

At a more detailed level, the projected light distribution carries information about the formation and dynamical state of the galaxy. If a galaxy were intrinsically axisymmetric, its projected isophotes would have a common position angle. A photometric position angle that changes with radius is therefore a direct signature of a projected structure more complex than a single aligned axisymmetric figure [15]. The shapes of the isophotes provide another clue. Deviations from perfect ellipses are commonly quantified with Fourier coefficients, especially

the lowest-order coefficient a_4: negative values correspond to boxy isophotes, while positive values correspond to disky isophotes. Luminous elliptical galaxies tend to be rounder and more boxy, whereas less luminous ellipticals are more frequently flattened and disky [11, 56]. These trends connect directly to galaxy assembly, with boxy, slowly rotating systems commonly associated with dry merger histories and disky systems more often retaining ordered rotational structure. Projection effects can also hide intrinsic triaxiality, so an image without an obvious isophotal twist can still correspond to a non-axisymmetric galaxy.

The same images also provide the radial surface-brightness profiles used to build stellar mass models. Several analytic functions have been developed for this purpose over the past several decades. A historically important model for elliptical galaxies is the de Vaucouleurs profile, which is the $n = 4$ case of the more general Sérsic profile [187, 160]:

$$I(R) = I_e \exp\left[-b_n\left(\left(\frac{R}{R_e}\right)^{1/n} - 1\right)\right], \tag{1.2}$$

where R_e is the effective radius, I_e is the intensity at that radius, n is the Sérsic index, and b_n is chosen so that R_e encloses half of the total light. The Sérsic index controls the concentration of the profile and has long been used as a compact way to describe galaxy structure.

The most massive ellipticals often require a more nuanced description. Their central surface brightness profiles can fall below the inward extrapolation of a Sérsic profile fit to larger radii, producing partially depleted stellar cores. These cores are commonly interpreted as the result of binary SMBHs ejecting stars from the central region during dry mergers, motivating the Core-Sérsic profile: an outer Sérsic-like profile joined to an inner power-law-like core [7, 123, 70, 69]. The break radius in these models has itself been found to correlate with SMBH mass, providing another link between the central black hole and the galaxy-scale light profile [69, 49, 177].

Rather than using the Sérsic or core-Sérsic profiles described above as the dynamical input, this dissertation uses a Multi-Gaussian Expansion (MGE) as the primary photometric representation for dynamical modeling. The MGE method represents the projected surface brightness as a sum of two-dimensional Gaussian components [30],

$$\Sigma(x', y') = \sum_{j=1}^{N} \frac{L_j}{2\pi\sigma_j'^2 q_j'} \exp\left[-\frac{1}{2\sigma_j'^2}\left(x_j'^2 + \frac{y_j'^2}{q_j'^2}\right)\right], \tag{1.3}$$

where L_j, σ_j', and q_j' are the luminosity, projected dispersion, and projected axis ratio of the jth Gaussian component. This parameterization is flexible enough to fit realistic galaxy images while remaining convenient for two additional reasons. First, Gaussian components can be convolved with Gaussian point-spread functions analytically, and second, for assumed viewing geometry they can be deprojected into three-dimensional luminosity densities that enter directly into dynamical models.

The deprojection step is central and intrinsically non-unique. Observations collapse a three-dimensional stellar distribution into a two-dimensional image on the sky. To recover a three-dimensional luminosity density, one must assume something about the galaxy's intrinsic shape and viewing direction. In axisymmetric models this usually reduces to an inclination angle. In triaxial models, a larger space of intrinsic axis ratios and viewing angles must be considered. The photometric model therefore defines the stellar contribution to the gravitational potential explored by the dynamical models.

1.2 Spectroscopic Observations and Stellar Kinematics

Spectroscopy, on the other hand, measures flux as a function of wavelength rather than only integrated light through a broad filter, and as a result, provides a much richer set of information beyond photometric measurements alone. Galaxy spectra can be used to infer stellar populations, chemical abundances, gas emission, dust attenuation, and, most important for this dissertation, the motions of stars within the galaxy.

The kinematic information comes from Doppler shifts. Absorption features in a stellar spectrum are shifted to shorter or longer wavelengths depending on the line-of-sight velocity of the star. For nearby stars, individual velocities can sometimes be measured directly. In external galaxies, the individual stars are generally unresolved. The observed spectrum in a spatial aperture is therefore the luminosity-weighted sum of many stellar spectra, each shifted by the line-of-sight velocity of its star.

Integral-field spectroscopy turns this measurement into a two-dimensional kinematic map. Instead of producing a single spectrum for a whole galaxy or a long-slit sequence along one axis, an integral-field spectrograph measures spectra across a field of view. After the LOSVD is extracted in each spatial bin, the result is a map of stellar velocity, velocity dispersion, and higher-order LOSVD shape. Such maps reveal rotation, velocity-dispersion gradients, kinematic twists, and misalignments between the photometric and kinematic axes. These features are especially useful for identifying departures from axisymmetry and for constraining dynamical models of the intrinsic three-dimensional structure.

While early stellar kinematic extraction relied on Fourier and cross-correlation techniques [178, 10], modern analyses usually fit the spectrum itself in pixel space. The most widely used tool for this purpose, and the one used throughout this dissertation, is the penalized pixel-fitting method pPXF [28, 32].

A compact version of the pPXF spectral model is

$$G_{\rm mod}(x) = \sum_{n=1}^{N} w_n \left[T_n(x) \otimes \mathcal{L}(cx)\right] \sum_{k=1}^{K} a_k P_k(x) + \sum_{l=1}^{L} b_l P_l(x) + \sum_{j=1}^{J} c_j S_j(x). \tag{1.4}$$

Here $G_{\rm mod}(x)$ is the model galaxy spectrum as a function of spectral pixel x, T_n are stellar template spectra, w_n are the template weights, and $\mathcal{L}$ is the LOSVD. The multiplicative

polynomials P_k with coefficients a_k adjust the continuum shape; the additive polynomial terms with coefficients b_l account for additional low-order continuum mismatches. The optional sky templates S_j with coefficients c_j can be used to model residual sky contamination. pPXF finds the mixture of template spectra and LOSVD broadening that best reproduces the observed galaxy spectrum.

Modern integral-field observations often have high enough signal-to-noise to measure departures from a purely Gaussian LOSVD in addition to a mean velocity and dispersion. These departures are usually expressed with a Gauss-Hermite series [117]. The leading terms are the mean velocity V and velocity dispersion σ:

$$\mathcal{L}(v) = \frac{e^{-y^2/2}}{\sigma\sqrt{2\pi}} \left[1 + \sum_{m=3}^{N_{\rm GH}} h_m H_m(y)\right], \qquad y \equiv \frac{v - V}{\sigma}. \tag{1.5}$$

The h_3 moment measures the leading skewness of the LOSVD, h_4 measures the leading kurtosis-like symmetric deviation, and still higher terms describe progressively finer departures from Gaussianity. These higher moments matter because real galaxy LOSVDs are rarely perfect Gaussians. In dynamical modeling, they constrain the distribution of stellar orbits beyond the information contained in the velocity dispersion alone.

1.3 Dynamical Modeling of Galaxies

Dynamical modeling provides the framework for turning the observables introduced above – photometry and spectroscopy – into measurements of the gravitational potential, including the mass of a central SMBH. The modeling task is to identify the combination of black hole mass, stellar mass, dark matter, intrinsic galaxy shape, and stellar orbital structure that simultaneously reproduces the observed light distribution and kinematics.

A useful starting point is the stellar distribution function, $f(\boldsymbol{x}, \boldsymbol{v}, t)$, which describes the density of stars in six-dimensional phase space. The stellar density follows by integrating over velocities,

$$\rho_*(\boldsymbol{x}, t) = \int f(\boldsymbol{x}, \boldsymbol{v}, t)\, d^3\boldsymbol{v}. \tag{1.6}$$

For the purposes of galaxy dynamics, stars in an elliptical galaxy are usually treated as a collisionless system moving in a smooth gravitational potential. Conservation of phase-space density then gives

$$\frac{\partial f}{\partial t} + \nabla_{\boldsymbol{x}} \cdot (f\dot{\boldsymbol{x}}) + \nabla_{\boldsymbol{v}} \cdot (f\dot{\boldsymbol{v}}) = 0. \tag{1.7}$$

Using $\dot{\boldsymbol{x}} = \boldsymbol{v}$ and Newton's equation $\dot{\boldsymbol{v}} = -\nabla_{\boldsymbol{x}}\Phi$, this becomes the collisionless Boltzmann equation (CBE),

$$\frac{\partial f}{\partial t} + \boldsymbol{v} \cdot \nabla_{\boldsymbol{x}} f - \nabla_{\boldsymbol{x}}\Phi \cdot \nabla_{\boldsymbol{v}} f = 0. \tag{1.8}$$

The potential is related to the mass distribution through Poisson's equation,

$$\nabla^2\Phi = 4\pi G\rho_{\rm tot}, \tag{1.9}$$

where $\rho_{\rm tot}$ includes stars, dark matter, and any central black hole contribution [16, 21].

Although the CBE is the natural starting point, solving directly for a full distribution function is often more information than is needed, or more difficult than the data justify. A common alternative is to take moments of the CBE over velocity. The zeroth moment gives a continuity equation for the stellar density. The first moment gives the Jeans equations. In Cartesian coordinates, one useful form is

$$\nu\frac{\partial\overline{v_j}}{\partial t} + \nu\overline{v_i}\frac{\partial\overline{v_j}}{\partial x_i} = -\nu\frac{\partial\Phi}{\partial x_j} - \frac{\partial\left(\nu\sigma_{ij}^2\right)}{\partial x_i}, \tag{1.10}$$

where ν is the stellar density, $\overline{v_j}$ is the mean velocity, and σ_{ij}^2 is the velocity-dispersion tensor. This equation relates the gravitational potential to the first and second moments of the velocity distribution, and it is the basis for Jeans modeling as well as simpler global mass estimators.

The Virial Theorem

The simplest dynamical mass estimates follow from the virial theorem, which can be derived from the Jeans equations by multiplying the first-moment equation by position, integrating over space, and considering a steady-state system. In tensor form, this procedure relates the kinetic-energy tensor to the potential-energy tensor. Taking the trace gives the scalar virial theorem,

$$2K + W = 0, \tag{1.11}$$

where K is the total kinetic energy and W is the total gravitational potential energy.

This relation provides a direct intuitive connection between observed stellar motions and enclosed mass. If the characteristic size of a galaxy is represented by the effective radius R_e and the characteristic stellar speed by an aperture velocity dispersion σ_e, then the virial theorem motivates an estimator of the form

$$M_{\rm dyn} \simeq k\frac{R_e\sigma_e^2}{G}, \tag{1.12}$$

where the coefficient k depends on the structure of the galaxy and on the precise definitions of R_e and σ_e [29]. This kind of estimator is powerful because it is simple and depends on directly measurable quantities. It also makes clear why galaxy size, luminosity, and velocity dispersion are so tightly connected in scaling relations such as the Fundamental Plane [57, 46].

The limitation is that a virial estimate is deliberately coarse. It gives a global mass scale that combines the contributions from the central black hole, stars, and dark matter. It also compresses the full velocity distribution into a single characteristic dispersion. For black hole mass measurements, where the central potential must be distinguished from the stellar mass distribution and orbital anisotropy, more detailed models are required.

Jeans Anisotropic Modeling

Jeans models use Equation 1.10 more directly. A trial mass model is specified, usually including a stellar density inferred from photometry, a stellar mass-to-light ratio, a central black hole, and sometimes a dark matter halo. The Jeans equations are then solved to predict projected velocity moments that can be compared with observed stellar kinematics.

The Jeans equations relate moments of the distribution function, but they do not determine the full velocity distribution by themselves. Additional closure assumptions are required. The Jeans Anisotropic Modeling (JAM) method provides a widely used and efficient closure by assuming axisymmetry and a specified alignment and anisotropy of the velocity ellipsoid [26]. In the commonly used cylindrically aligned formulation, the anisotropy can be written in terms of

$$\beta_z = 1 - \frac{\overline{v_z^2}}{\overline{v_R^2}}. \tag{1.13}$$

With this assumption, and with the luminosity density represented by an MGE, the projected second velocity moment can be calculated rapidly for many trial potentials.

A key reason JAM models are valuable is their speed. They provide an efficient way to estimate stellar mass-to-light ratios, black hole masses, inclinations, and dark matter contributions, and they are useful as cross-checks on more computationally expensive models that will be the focus of the rest of this thesis. However, this speed comes from reducing the freedom of the distribution function to a small number of closure choices. The cylindrically aligned version described above is one common choice; a spherically aligned version provides a related closure in spherical coordinates [26, 31]. In either case, the model must specify how the velocity ellipsoid is aligned and how the anisotropy varies with position, often through a single parameter such as β_z or through a small number of spatial zones. These choices make the calculation tractable, but they are imposed by the model rather than determined freely by the Jeans equations.

These restrictions matter because real galaxies do not need to have a single global velocity-ellipsoid alignment or a compact anisotropy profile. Moreover, the central region influenced by a black hole, the stellar body, and the outer dark-matter-dominated halo can have different orbital structure, and the most massive early-type galaxies are often not strictly axisymmetric. Controlled tests with simulated barred galaxies and cosmological galaxy remnants show that JAM can still recover useful global mass scales, while also showing where the assumptions make the models fall short, in particular in measurements of the viewing angle, non-axisymmetric structure, and spatially-varying anisotropy [100, 104].

Typical JAM applications also compare the model to the lowest-order velocity information, often through the projected second moment $V_{\rm rms} = \sqrt{V^2 + \sigma^2}$. This compresses the line-of-sight velocity distribution into its mean velocity and dispersion and leaves aside much of the information in the non-Gaussian LOSVD shape being measured by modern IFU observations. More fundamentally, a Jeans model constrains moments of the distribution function rather than constructing the distribution function itself. A model can therefore

reproduce the observed second moments while still having limited freedom in the orbit mix and intrinsic shape that generated those moments.

For these reasons, JAM is best viewed as a fast and informative dynamical model rather than a complete description of the stellar distribution function. The next step is to construct that distribution function explicitly through orbit superposition. In Schwarzschild modeling, the orbit library samples the phase space of a trial potential, and the fitted orbit weights determine which combinations of stellar trajectories reproduce the observed light distribution and kinematics. This added freedom is essential when the goal is to separate black hole mass, stellar mass-to-light ratio, dark matter, anisotropy, and intrinsic galaxy shape in systems where several different orbital structures can produce similar low-order velocity moments [40, 183, 186].

Schwarzschild Orbit Modeling

The central dynamical method used in this dissertation is Schwarzschild orbit modeling. Schwarzschild's method demonstrated that a self-consistent triaxial stellar system can be represented as a non-negative superposition of stellar orbits integrated in a fixed gravitational potential [158]. Instead of specifying the distribution function through a small set of analytic assumptions, the method represents the distribution function numerically through the weighted orbit library.

The procedure begins by choosing a trial potential. In the applications here, that potential may include a central black hole, a stellar mass component obtained from the deprojected light profile and a stellar mass-to-light ratio, and a dark matter halo. A large library of stellar trajectories is then integrated in this potential. Along each orbit, the model records how much time the star spends in different regions of space and what line-of-sight velocities it would contribute when projected onto the sky. The orbit library is then assigned non-negative weights so that the weighted superposition reproduces both the stellar light distribution and the observed stellar kinematics.

Schematically, if $\mathcal{L}_{jk}(v)$ is the LOSVD contribution of orbit k to spatial bin j, the model LOSVD is

$$\mathcal{L}_{j,\mathrm{model}}(v) = \sum_k w_k \mathcal{L}_{jk}(v), \qquad w_k \geq 0. \tag{1.14}$$

The quality of a trial potential can then be assessed by comparing the model LOSVD moments to the observed moments. By repeating the procedure over many trial potentials, one can infer the mass and shape parameters that best reproduce the data.

Schwarzschild modeling is more computationally expensive than virial or Jeans modeling, but it is also substantially more flexible. The method represents the distribution function through a numerical orbit library, allowing complicated anisotropy and orbital structure to emerge from the weighted superposition. It can use the full shape of the LOSVD, including higher-order Gauss-Hermite moments, and it can model systems whose orbital structure is too complex to be captured by simpler moment-based approaches.

The technique has developed steadily since its first applications. Early work adapted orbit superposition from constructing equilibrium galaxy models to fitting real galaxy kinematic data, including spherical and axisymmetric applications that constrained dark matter and central black holes [148, 185, 41, 64]. Subsequent studies explored the reliability and degeneracies of black hole mass and mass-to-light ratio recovery in orbit-based models [180, 40]. Triaxial orbit-based modeling later expanded the method to galaxies with three unequal intrinsic axes, opening the possibility of measuring intrinsic galaxy shapes together with mass parameters [183, 181].

Recent work by our group has focused on making triaxial Schwarzschild modeling more reliable and useful for SMBH mass measurements. The TriOS code and framework have been developed and tested in both axisymmetric and triaxial limits, with particular attention to orbit sampling, deprojection parameters, likelihood exploration, and recovery of known input parameters from mock observations [142, 143]. These developments make it possible to fit black hole mass, stellar mass-to-light ratio, dark matter content, and intrinsic shape simultaneously in massive early-type galaxies. This is the modeling framework used in the main dynamical chapters of this dissertation.

1.4 Galaxy Catalogs and PTA Source Searches

The individual-galaxy measurements described above also feed into a broader population problem. PTAs are sensitive to gravitational waves from binary SMBHs at nanohertz frequencies, for which the strain of an individual source depends strongly on binary mass and distance. Direct dynamical black hole masses are available for only a small number of nearby systems, so searches for candidate binary hosts must often rely on galaxy catalogs in which SMBH masses are inferred from more accessible observables.

The catalog work in this dissertation builds on this idea by combining large all-sky photometric samples, including WISExSuperCOSMOS and 2MPZ, to estimate homogeneous stellar masses from WISE mid-infrared photometry and then infer SMBH masses through black hole–host-galaxy scaling relations [12, 13, 90, 118, 93]. Such a catalog provides a ranked census of massive nearby galaxies that can be used to narrow searches within PTA localization regions, supply astrophysically motivated priors for targeted binary searches, and connect the local massive black hole population to the emerging nanohertz gravitational-wave sky [1, 2].

1.5 Overview of This Dissertation

The remainder of this dissertation applies the observational and dynamical ideas introduced above to both individual galaxies and to constructing a large galaxy catalog.

Chapter 2 presents Schwarzschild modeling of the nearby massive elliptical galaxy NGC 2693. Using spatially resolved stellar kinematics and a photometric model of the stellar light dis-

tribution, the chapter measures the central SMBH mass, stellar mass-to-light ratio, dark matter content, and intrinsic galaxy shape. NGC 2693 is close to axisymmetric in some respects, but the chapter uses the triaxial modeling framework to test how assumptions about intrinsic shape affect the inferred mass parameters.

Chapter 3 turns from modeling real galaxy observations to modeling controlled mock observations. This chapter focuses on generating simulated galaxy datasets with known input parameters and using them to test the accuracy and precision of the TriOS triaxial Schwarzschild modeling code. These recovery tests are a necessary calibration step because a flexible six-dimensional search is useful only if it can recover black hole mass, mass-to-light ratio, dark matter content, and intrinsic shape in experiments where the true answer is known.

Chapter 4 applies the same broad Schwarzschild modeling technique to the nearby radio galaxy NGC 315. This galaxy has an existing SMBH mass measurement from CO gas dynamics, making it a particularly valuable system for comparison. By measuring the black hole mass using stellar dynamics, this chapter provides a cross-check between two different dynamical tracers and helps assess systematic uncertainties in SMBH mass measurements.

Chapter 5 shifts from detailed modeling of individual galaxies to population-level inference. It constructs an all-sky galaxy catalog with homogeneous stellar masses and inferred SMBH masses. The catalog is designed to support searches for host galaxies of SMBH binaries detected or constrained by PTAs. In this way, the final chapter connects the detailed local calibration of black hole–galaxy relations to the broader problem of identifying the massive black hole population responsible for nanohertz gravitational-wave signals.

Chapter 2

A Triaxial Orbit-based Determination of the Black Hole Mass and Intrinsic Shape of Elliptical Galaxy NGC 2693

This chapter applies triaxial Schwarzschild orbit modeling to NGC 2693, a massive elliptical galaxy whose projected photometry and regular stellar rotation make it appear close to axisymmetric. Using high-resolution *HST* imaging and spatially resolved stellar kinematics from Gemini/GMOS and the Mitchell Spectrograph, we measure the mass components and intrinsic shape of the galaxy simultaneously. The main motivation is to test whether galaxies that appear nearly axisymmetric in projection still require triaxial dynamical models for robust SMBH mass measurements. This chapter was originally published as:

Jacob D. Pilawa, Emily R. Liepold, Silvana C. Delgado Andrade, Jonelle L. Walsh, Chung-Pei Ma, Matthew E. Quenneville, Jenny E. Greene, and John P. Blakeslee. "The MASSIVE Survey. XVII. A Triaxial Orbit-based Determination of the Black Hole Mass and Intrinsic Shape of Elliptical Galaxy NGC 2693". In: The Astrophysical Journal 928, 178 (Apr. 2022). doi: 10.3847/1538-4357/ac58fd. arXiv: 2111.13699 [astro-ph.GA].

2.1 Introduction

The most massive SMBHs in the local universe have been found at the centers of some of the most massive nearby elliptical galaxies. At stellar masses $M_* \gtrsim 10^{11.5} M_\odot$ targeted by the volume-limited MASSIVE galaxy survey [113], a majority of these massive elliptical galaxies exhibit slow or no detectable rotation [189, 188, 52]. When selected by environments, massive galaxies in the cores of galaxy clusters are also predominantly slow- or non-rotators (e.g., Brough et al. [24], Loubser et al. [112], Krajnović et al. [96], and Graham et al. [71]). In comparison, the ATLAS^{3D} project surveyed early-type galaxies at lower masses ($10^{10} M_\odot \lesssim M_\star \lesssim 10^{11.5} M_\odot$) and found most to be fast rotators [50].

When the kinematic axis of a massive elliptical galaxy can be identified, it is often misaligned from the photometric major axis (e.g., Ene et al. [52]). Detailed IFS kinematic maps also show intricate local twists, and the central and main-body kinematic axes within a galaxy are not always aligned [53, 99]. All these features are strong indications that local massive elliptical galaxies are triaxial in intrinsic shape, and not axisymmetric as is often assumed in prior dynamical modeling studies of early-type galaxies, which would only allow rotation about the minor axis [15].

The MASSIVE galaxy survey [113] is designed to study all the major dynamical components – SMBH, stars, and dark matter halo – in the most massive ~ 100 ($M_* \gtrsim 10^{11.5} M_\odot$) early type galaxies (ETGs) in the local volume (out to ~ 100 Mpc). For a subset of 20 MASSIVE galaxies, we have completed the stellar kinematic measurements from our IFS observations that cover both the galaxies' central regions with high spatial resolution, and wide fields out to at least one effective radius. In this paper, we focus on NGC 2693, a galaxy with one of the largest ratios of V/σ, where the stellar rotation is $V \sim 160\, km\ s^{-1}$ and the velocity dispersion is $\sigma \sim 300\, km\ s^{-1}$ [189, 53]. The only other MASSIVE galaxy that exhibits similarly fast and regular rotation is NGC 1453. NGC 1453 is recently studied both in the axisymmetric limit [105] and with fully triaxial orbit modeling [141]. The triaxial models are found to better recover the input kinematics while also fitting the non-axisymmetric features present in NGC 1453. Given the similarities between NGC 2693 and NGC 1453, we turn to NGC 2693 in this paper.

We use the orbit superposition method to obtain dynamical mass measurements of the components of NGC 2693 with observations taken as part of the MASSIVE Survey. We use our latest version of the TriOS code [140, 141] based on the code by van den Bosch et al. [183][1] to perform a full triaxial modeling of the stellar orbits in NGC 2693 and to simultaneously constrain the galaxy's intrinsic shape, $M_{\rm BH}$, and other mass parameters.

In Section 2, we describe the photometric observations used to model the deprojected stellar mass distribution of NGC 2693, as well as the spectroscopic observations from GMOS (Hook et al. [77]) covering the central kpc and wide-field observations from the McDonald Mitchell IFS (Hill et al. [76]). In Section 3, we describe the triaxial modeling and phase space sampling in our Schwarzschild orbit models. In Section 4, we discuss our search for the best-fit triaxial galaxy model, marginalization scheme for extracting best-fit parameters, and resulting best-fit dynamical model. In Section 5, we compare the triaxial model to axisymmetric Schwarzschild orbit models and Jeans modeling of NGC 2693.

We adopt a distance to NGC 2693 of 71.0 Mpc from the MASSIVE-WFC3 project [68] using the surface-brightness fluctuation technique [84, 17]. At this distance, $1''$ is 354 pc, assuming a flat ΛCDM cosmology with a matter density of $\Omega_m = 0.315$ and a Hubble parameter of $H_0 = 70\, km\ s^{-1}$ Mpc^{-1}.

[1] https://github.com/remcovandenbosch/TriaxSchwarzschild

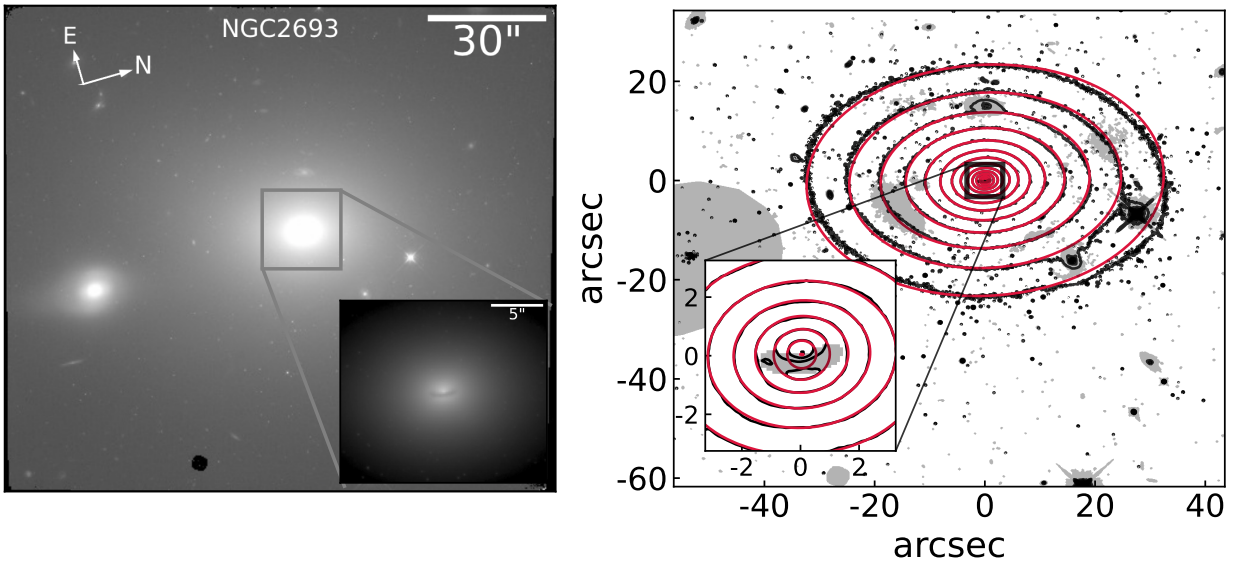

Figure 2.1: (Left) The F110W-band *HST* image of NGC 2693 used for our photometry. A companion galaxy which is masked from photometric analysis (see text) can be seen $\sim 50''$ south of NGC 2693. (Left inset) NGC 2693 has a dust disk extending approximately $1.5''$ (in radius) from the center. This feature is masked from our MGE fitting. (Right) Isophotes of the *HST* WFC3 IR image of NGC 2693 (black) and the best fit MGE model (red). The inset shows the central region containing the nuclear dust disk. The gray regions are masked when performing the fit as described in the text.

2.2 Photometric and Spectroscopic Observations

NGC 2693 is a relatively isolated galaxy, being the only identified member of its galaxy group in the 2MASS "high-density contrast" group catalog [42]. We obtain photometric observations of NGC 2693 in the F110W filter of *HST* and spectroscopic observations using GMOS in IFS mode on the 8.1 m Gemini North telescope and the Mitchell IFS on the 2.7m Harlan J. Smith Telescope at McDonald Observatory. In this section, we describe these observations, the data reduction process, modeling the surface brightness profile, and the extraction of the stellar kinematics of NGC 2693.

HST Observations and Stellar Mass Profile of NGC 2693

We model the spatial distribution of stars in NGC 2693 with observations from the IR channel of *HST* WFC3 in the F110W filter (Figure 2.1). Observations (GO-14219, P.I. J. Blakeslee) were taken over a single orbit and have a total exposure time of 2695 seconds. This orbit was divided into five dithered exposures with a sub-pixel dither pattern to improve measurements

Table 2.1: Best-fit MGE parameters to the NGC 2693 *HST* WFC3 IR photometry. Each Gaussian component (k) is parametrized by a central surface density $I_k = L_k/2\pi\sigma_k'^2 q_k'$, dispersion σ_k', and axis ratio q_k', where primed variables are projected quantities. The central surface densities have been corrected for a galactic extinction of 0.017 mag and assume an absolute (Vega) magnitude of 3.89 for the Sun. The components all have a PA of 167.9° east of north.

I_k $[L_{F110W,\odot}/\mathrm{pc}^2]$	σ_k' $['']$	q_k'
6521.78208	0.10611	0.99990
18597.03132	0.24071	0.99990
17231.46878	0.51203	0.98100
14094.87758	1.21090	0.78400
4883.63124	2.49551	0.76540
1854.85184	4.66292	0.74880
694.17907	8.71737	0.73490
177.10426	12.21259	0.68370
217.66116	21.51988	0.71920
59.57494	66.58575	0.78070

of the point-spread function (PSF). We reduce the images using STScI's standard reduction pipeline, a specialized Python program[2] to correct for variable background levels, and the `Astrodrizzle` package [66]. We additionally perform background subtraction, removing a neighboring galaxy located 55″ to the south of NGC 2693, and construct a mask to exclude foreground stars, other galaxies, and detector artifacts. The final F110W image has a pixel scale of 0.″1. For details on the photometric data reduction, see Goullaud et al. [68].

The *HST* observations of NGC 2693 show slightly boxy isophotes near the center of the galaxy, which become disky at radii larger than $\sim 5''$. There is a small compact dust disk extending 1.″5 in radius from the center. The galaxy's luminosity-weighted ellipticity is nearly constant with radius (beyond the region of the central dust disk) with a mean value $\langle\epsilon\rangle_L = 0.27 \pm 0.002$ [68]. Below we parametrize the surface brightness of NGC 2693 as a sum of 2D Gaussians with a common center and PA.

We run the Cappellari [30] Multi-Gaussian Expansion (MGE) code with regularization to avoid flattened components that artificially restrict the range of inclination angles that can be used during the dynamical modeling. We then tweak the MGE solution using `Galfit` [130]. We set a lower boundary on each component's projected axis ratio, q_k', of 0.65, which was determined from the previous regularized MGE run. The WFC3 PSF is accounted for by an empirical PSF constructed from extracting, summing, and re-normalizing 11 bright stars within the field of view. We apply the mask of other objects in the field plus a mask for the central dust disk. Since no high-resolution multi-band imaging for NGC 2693 was

[2] https://github.com/gbrammer/wfc3

available, we construct a dust mask by eye initially, conservatively flagging only the most obviously affected pixels, and then we adopt an iterative approach. After the `Galfit` run converged, we examine the residual image and extend the dust mask to neighboring pixels with residuals above a selected threshold. We continually repeat the process, each time modifying the threshold, until achieving residuals at the $\sim 5\%$ level at the nucleus.

Our best-fit MGE is composed of 10 Gaussians with the central surface brightness I_k, projected dispersion σ'_k, and q'_k given in Table 2.1. The model is a good description of the data, as seen in Figure 2.1, with residuals below $\sim 6\%$ out to a radius of $\sim 70''$.

All of the MGE components have the same PA of 167.9° east of north, but we run `Galfit` again allowing for the PA to vary between components. The initial guesses for the parameters are set to the best-fit MGE from Table 2.1, and we use the same empirical PSF and mask. When allowing for PA twists, our best-fit MGE consists of three circular Gaussians at small radii. The next five Gaussians have PA twists of $< 3°$ relative to a PA of 167.9° and the outer three components have smaller PAs of $\sim 155°$. While we subtracted the companion galaxy and masked the remaining residuals, the outermost region of NGC 2693 likely remains contaminated by the companion galaxy causing the smaller PAs for the largest three MGE components. Nevertheless, these two MGEs differed by less than 5% at all radii for which we have kinematic data. Beyond $50''$, the relative difference approaches $\sim 10\%$ primarily due to the companion. The negligible impact of allowing for a PA twist does not seem to improve our fit but rather fits the remaining contamination of the companion galaxy, and thus we adopt the MGE model with a spatially constant PA.

We further test the companion galaxy's impact on the measured photometric position angle by fitting subsections of the full *HST* WFC3 image. We perform two additional fits, one to the central $20'' \times 20''$ region and another to the central $40'' \times 40''$ region as opposed to the full $141'' \times 125''$ image. We use our fiducial MGE presented in Table 2.1 as initial guesses for the ten Gaussians, and we require the PA and center for all ten components to be the same. In both cases, the preferred photometric position angle changes negligibly compared to the fiducal case of 167.9° E of N. When fitting only to the central $20'' \times 20''$ region of the image, the preferred photometric PA is 168.6° E of N, and when fitting to the $40'' \times 40''$ region, the PA of the Gaussians is 168.2° E of N.

Central GMOS kinematics

We observed the central region of NGC 2693 in the 2016B semester with the two-slit mode of GMOS, providing a $5'' \times 7''$ ($\sim$1.7 kpc $\times$ 2.4 kpc) field-of-view composed of 1000 hexagonal lenslets, for a projected diameter of $0.2''$ per lenslet. In total, six science exposures were taken, each of 1200 seconds exposure time. The median seeing was $0.6''$ FWHM. We used the R400-G5305 grating with the CaT filter for clean coverage from $7800-9330$ Å. A $5'' \times 3.5''$ region of the sky, offset $1'$ from NGC 2693's central region was simultaneously observed. The spectral resolution was determined from arc lamp lines for each lenslet, with a median value of 2.3 Å FWHM.

The GMOS lenslets are binned to achieve a target S/N of 125 using the Voronoi-binning procedure [27]. This procedure results in a total of 60 bins. The spectra are co-added from individual lenslets within a single Voronoi bin as described in Ene et al. [51]. Example spectra for three bins at increasing radii are shown in Figure 2.2 (black curves).

We use the CaII triplet absorption features over a rest wavelength of 8420-8770Å to extract the stellar line-of-sight velocity distribution (LOSVD) for each bin with the penalized pixel-fitting (pPXF) method of Cappellari [32]. We choose to decompose each LOSVD into a Gauss-Hermite series up to order $n = 8$ as is done in Liepold et al. [105]. An additive polynomial of degree zero (a constant) and a multiplicative polynomial of degree three are used to model the stellar continuum for the spectra.

We compare two sets of stellar templates chosen from the MILES Calcium Triplet (CaT) Library of 706 stars [36]: the first set is limited to the 15 stars from Table 2 of Barth, Ho, and Sargent [5]; the second set includes all 706 stars in the library. The resulting kinematics are consistent within measurement errors, and we choose to use the former set of kinematics for dynamical modeling discussed later in this paper. These template spectra cover the wavelength range of 8347-9020Å with a 1.5Å spectral resolution FWHM.

We follow a nearly identical kinematic extraction procedure to that of Liepold et al. [105]. Three example stellar templates broadened by the best-fit LOSVDs are shown in Figure 2.2 (blue curves). The errors on the kinematic moments are determined with bootstrap methods as described in Section 4 of Ene et al. [51]. Figure 4.2 shows the kinematic maps of the eight Gauss-Hermite velocity moments for all 60 GMOS bins; Figure 2.4 shows the corresponding radial profiles of the moments (blue filled circles). The velocity map shows regular rotation with the maximum velocity reaching $|V| \sim 160\,km\ s^{-1}$; the σ map shows a central peak with an amplitude of $\sim 320\,km\ s^{-1}$. The mean errors on V and σ are $4.3\,km\ s^{-1}$ and $5.0\,km\ s^{-1}$, respectively. The errors on higher order moments (h_3 through h_8) are similar in amplitude, ranging from 0.010 to 0.013.

Wide-field Mitchell kinematics

NGC 2693 is one of ~ 100 MASSIVE galaxies observed using the Mitchell IFS. Three dither positions were used, and during each dither, we interleaved two 20 minute science frames with one 10 minute sky frame, for a total exposure time of 2 hours on-source. The Mitchell IFS consists of 246 fibers covering a $107'' \times 107''$ field of view. The observations covered a spectral range of 3650-5850Å that include the Ca HK region, the $G-$band region, Hβ, Mgb, and several Fe features.

Each fiber in the central region of NGC 2693 yields a spectrum of $S/N \gtrsim 50$, while the outer fibers are binned to achieve a $S/N \geq 20$. We obtain a total of 33 bins but drop the outermost 4 bins at $\sim 46''$ due to low S/N. We model the stellar LOSVD in a similar way to the GMOS data, fitting up to order $n = 6$ due to the lower S/N. We use the MILES library of 985 stellar spectra (Sánchez-Blázquez et al. [152] and Falcón-Barroso et al. [58]) as the templates. Details of the Mitchell data reduction and kinematic measurements are described in Veale et al. [189] and Veale et al. [188].

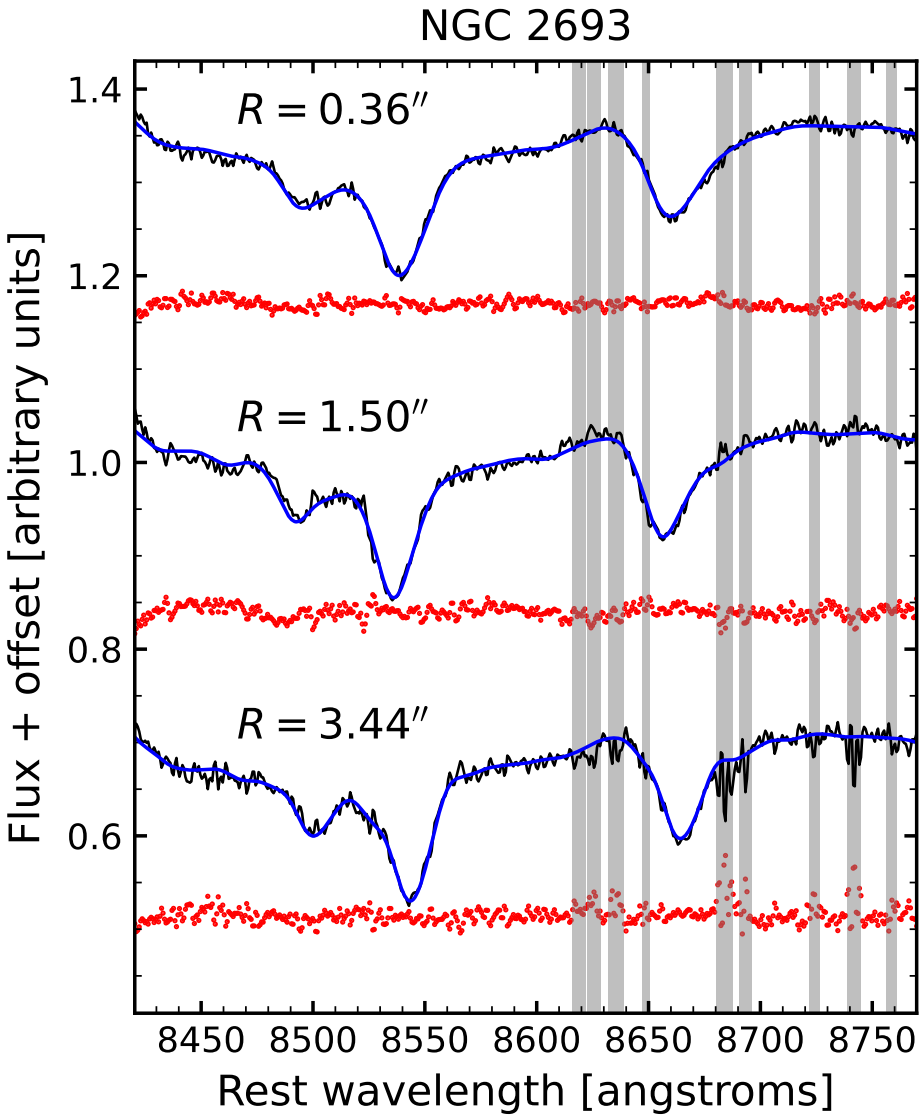

Figure 2.2: CaII triplet region of the GMOS IFS spectrum (black) of NGC 2693 for three example bins located at increasing distance from the nucleus: (top) central bin with $S/N = 204$, (middle) bin $1.50''$ from center with $S/N = 144$, and (bottom) bin $3.44''$ from center with $S/N = 100$. The spectrum is fit by broadening a series of stellar templates by the best-fit LOSVD (blue) over a wavelength range of $8420 - 8770\mathring{A}$. The grey shaded regions are excluded from the fit to account for improperly subtracted sky lines. The red points are the (best-fit minus observation) residuals offset by constants for clarity. The typical residual is $\sim 0.5\%$.

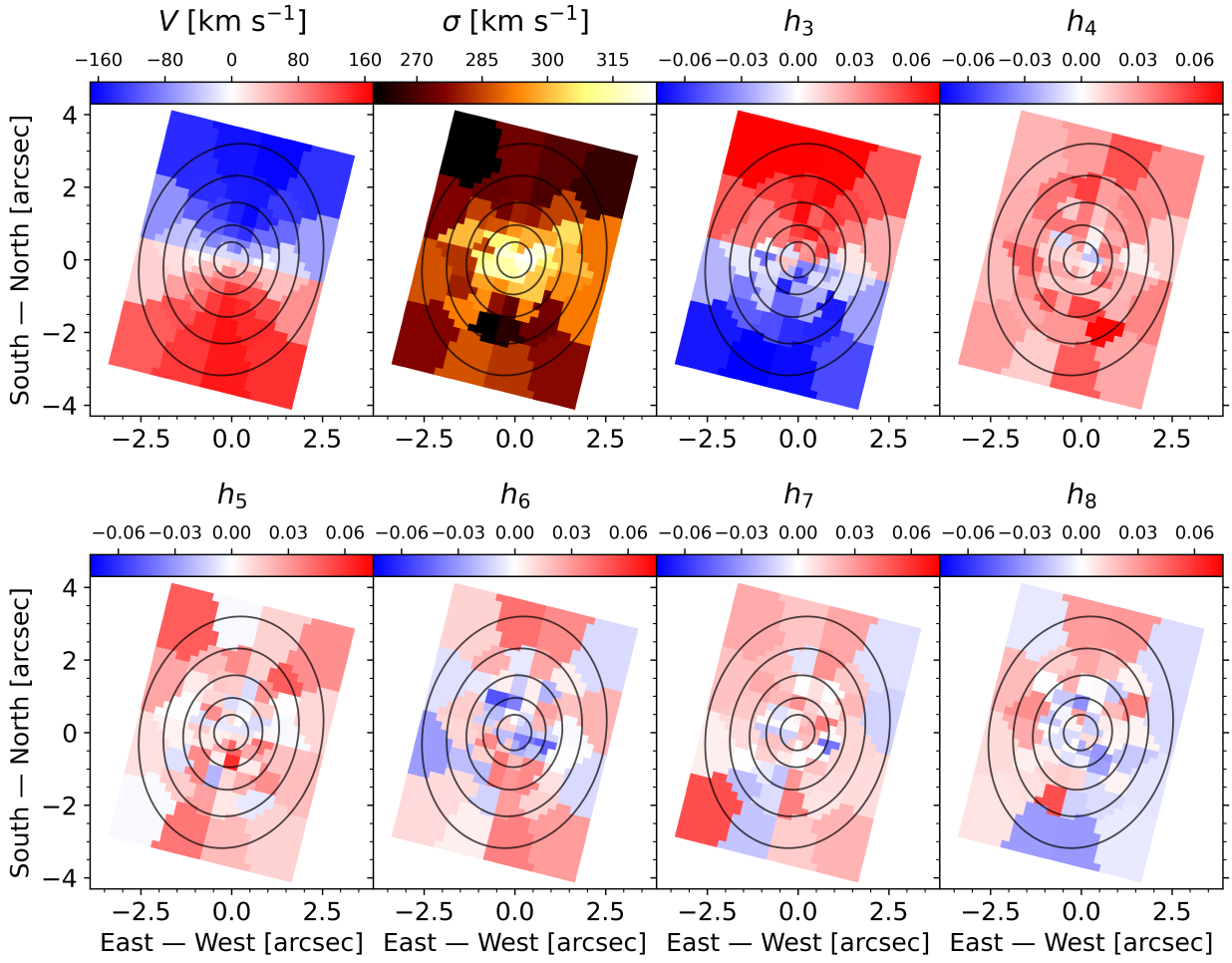

Figure 2.3: Spatial maps of the stellar kinematics extracted from the Gemini GMOS IFS spectra for 60 bins in the central $5'' \times 7''$ region of NGC 2693. Each panel shows a different moment of the Gauss-Hermite expansion of the line-of-site velocity distribution: the top-left two panels are the velocity V and velocity dispersion σ, with the higher-order h_i moments characterizing deviations from Gaussianity. The $+x$ axis of the galaxy is located 167 degrees East of North (North is up and East is to the left). The velocity map shows a prominent rotation pattern with maximal velocities of $|V| \sim 160\, km\ s^{-1}$; the σ maps shows a central peak. The black lines are surface brightness contours from the best-fitting MGE model in Table 2.1 and Figure 2.1.

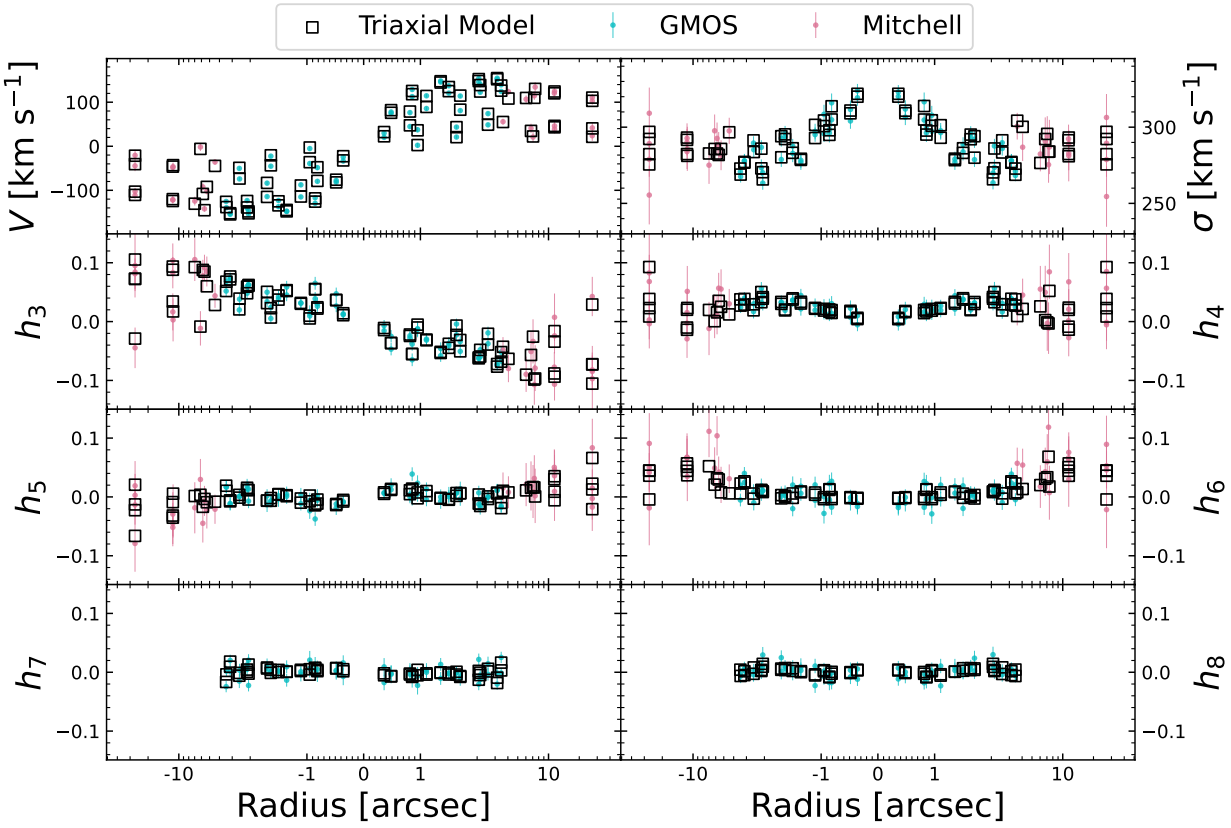

Figure 2.4: Radial profiles of the velocity moments determined from the GMOS (blue circles) and Mitchell (pink circles) IFS observations. The observed moments are well matched by those predicted from our best-fit triaxial galaxy model (black open squares) with mass parameters $(M_{\rm BH}, M^*/L, M_{15}) = (1.7 \times 10^9 M_\odot, 2.35, 7.1 \times 10^{11} M_\odot)$ and shape parameters $(T, T_{\rm maj}, T_{\rm min}) = (0.39, 0.09, 0.17)$. The spatial bins have been unfolded such that the bins whose centers lie between $-90°$ and $+90°$ of the photometric PA are plotted with positive radius and others with negative radius. Note that the axes are on a linear scale between $-1''$ and $1''$ and logarithmically scaled otherwise.

The radial profiles of the Mitchell kinematic moments are shown in Figure 2.4 (pink filled circles). The innermost few Mitchell fibers (each with a $4.1''$ diameter) overlap the FOV of GMOS. Reassuringly, the Mitchell kinematics in this region are in good agreement with the GMOS values averaged over the GMOS FOV. The mean errors on the Mitchell kinematics are about two times larger than the GMOS kinematics. The mean errors on V and σ are $8.95\,km\ s^{-1}$ and $12.2\,km\ s^{-1}$, respectively, with errors on higher order moments (h_3 through h_6) ranging from 0.030 to 0.039.

2.3 Triaxial Orbit Modeling of NGC 2693

The TriOS Code and Input Kinematics

We use the *TriOS* code [140, 141] to perform orbit modeling of NGC 2693. The galaxy is modeled as a stationary, triaxial gravitational potential composed of a SMBH, a stellar component specified by the deprojected MGE, and a dark matter halo. The six parameter galaxy model and the method used to search this parameter space is described in detail in Section 2.4.

For a collection of orbits spanning the phase space, we integrate each orbit for 2000 (loop orbits) or 200 (box orbits) dynamical times. At a large number of steps along the trajectory, we project the orbit onto the sky, keeping track of the projected position and line-of-sight kinematics. For each dataset (GMOS and Mitchell), the projected position is convolved with the respective instrumental PSF, and steps in the trajectory are binned according to the apertures described in Sections 2.2 and 2.3. This produces (i) a measure of the fraction of that orbit's time spent in each aperture and (ii) the LOSVD associated with the orbits within each kinematic bin. As described in Section 2.3, a superposition of these orbital contributions is found that best reproduces the observed kinematic LOSVD. We repeat this process for many gravitational potentials to find the galaxy parametrization that most closely reproduces the observed kinematics.

We fit for eight moments of the GMOS kinematics and six moments of the Mitchell kinematics presented in Section 2. We constrain additional moments up to and including h_{12} to be $0.0 \pm \delta$, where δ represents typical errors in the highest odd and even moments of each kinematic dataset. Our previous tests have showed that constraining only the lowest four moments and leaving the higher-order moments free in the orbit model could result in spurious behavior in the higher-order moments and the resulting LOSVDs (Figs. 10 and 11 of Liepold et al. [105]). We test the effects of constraining up to h_{16}, but moments h_{13} to h_{16} are sufficiently close to 0 when constraining the first twelve moments that the added constraint on the last four moments does not change our fits. Thus, we opt to leave moments higher than h_{13} unconstrained. We note that leaving moments h_9 to h_{12} unconstrained can shift the inferred best fit parameters by $\sim 10\%$.

Throughout the analysis, we model the GMOS and Mitchell PSFs as single, circularly symmetric Gaussians with FWHM of $0.56''$ and $1.2''$ respectively. To keep the potential non-singular at the origin, we use a Plummer-style potential for the central black hole with a force softening length of 3×10^{-4} arcsec, which is roughly three orders of magnitude smaller than the central-most GMOS bins.

Orbital Phase-space Sampling and Orbital Weight Optimization

Insufficient orbit sampling can bias the inferred mass and shape parameters, so particular care is needed in choosing initial conditions for the orbits. In the TriOS code, the orbits are initialized in two different spaces, referred to as "start spaces" [159, 183]. A Cartesian

coordinate system centered on the galaxy's nucleus is used. The x, y, and z axes are parallel to the intrinsic major axis a, intrinsic intermediate axis b, and intrinsic minor axis c, respectively.

The first start space, called the x-z start space, launches loop orbits from the (x, z) plane and a velocity in the $+y$ direction at $N_E = 40$ different energies (implicitly sampled over radii). The (x, z) positions are determined by dividing the start space into N_{I_2} rays spanning polar angles from 0 to $\pi/2$ in the x–z plane; along each ray, we space N_{I_3} orbits. The code allows for additional dithering of orbits, where we group together $N_{\rm dither} = 3$ adjacent initial conditions for denser and smoother phase-space sampling. Dithering orbits increases the sampling density by a factor of $N^3_{\rm dither}$ since dithering is performed in all three dimensions. Orbits launched from the same initial position but with velocity in the $-y$ direction are valid orbits. To include these orbits in our modelling, we invert the LOSVD from each orbit in the (x, z) start space and store the resulting orbits in a second 'retrograde' library.

Similar to NGC 1453 (Section 4.3 of Quenneville, Liepold, and Ma [141]), we find spurious oscillations in the goodness-of-fit χ^2 landscape while varying T for NGC 2693 when using $N_{I_2} = 9$ and $N_{I_3} = 9$ in the (x, z) start space. The spacing between these oscillations matches the spacing between dithered initial conditions, resulting in periodic local minima and thus biased results for the intrinsic galaxy shape. We eliminate these unwanted oscillations by increasing the angular sampling N_{I_2} of orbits in the (x, z) start space from $N_{I_2} = 9$ to $N_{I_2} = 15$. The total number of orbits used in our loop library is therefore $2 \times N^3_{\rm dither} \times N_E \times N_{I_2} \times N_{I_3} = 2 \times 3^3 \times 40 \times 15 \times 9 = 291,600$, where the factor of 2 accounts for the time reversed copy of each orbit.

A second start space, called the stationary start space, is used to generate a library of box orbits in a triaxial system. In this start space, orbits with a given energy E are launched at rest with $v_x = v_y = v_z = 0$ from starting positions, where the gravitational potential is $\Phi(R, \theta, \phi) = E$, and θ and ϕ are the polar and azimuthal angles in the usual spherical coordinate system. Both θ and ϕ are sampled uniformly between 0 and $\pi/2$ at $N_\theta = 9$ and $N_\phi = 9$ locations. We find no oscillatory behavior in the resulting χ^2 for this start space, so we choose $(N_\theta, N_\phi, N_{dither}) = (9, 9, 3)$. The total number of orbits in our box library is thus $3^3 \times 40 \times 9 \times 9 = 87,480$.

With three integrated orbit libraries consisting of $291,600 + 87,480 = 379,080$ orbits for a given galaxy model, we solve for the linear combination of orbital weights that best fits the observed kinematics and surface brightness. As noted, we use a dithering factor of 3, meaning that $3^3 = 27$ neighboring orbits are bundled while solving for the orbital weights. Accordingly, there are $379,080/3^3 = 14,040$ independent weights in each model. We compute these weights to minimize the χ^2 associated with the kinematics using non-negative least squares [102], under the constraint that both the projected mass within each aperture and the 3D mass distribution in coarse bins are consistent within 1% of the MGE. We do this for all kinematic bins simultaneously to build a model LOSVD in each bin for each galaxy model.

We note that the choice of 1% mass constraint above is based on the range of values commonly adopted in earlier orbit modeling work (e.g., 2% in van den Bosch and de Zeeuw

[182]; 1% in Walsh et al. [193]). Our results do not depend on the exact value used: relaxing the 3D mass constraint from 1% to 10% changes our best-fit $M_{\rm BH}$ reported below by only a few %, which is well within the 1σ uncertainty. Additionally, the typical χ^2 associated with the mass constraint is only a small fraction ($\sim 0.5\%$) of the size of the χ^2 from the stellar kinematics. We obtain identical $M_{\rm BH}$ regardless of whether we use χ^2 from kinematics alone or include χ^2 associated with the mass constraint.

2.4 Parameter Search of Triaxial Models

Galaxy Model

We use a six-parameter model to describe the triaxial potential of NGC 2693. Three parameters are for the mass components: black hole mass $M_{\rm BH}$, stellar mass-to-light ratio M^*/L_{F110W} (hereafter M^*/L), and enclosed dark matter mass at 15 kpc, M_{15}. A logarithmic dark matter halo is assumed, where the enclosed dark matter mass at radius r is

$$M(<r) = \frac{V_c^2}{G}\frac{r^3}{r^2+R_c^2}\,, \tag{2.1}$$

where R_c is the scale radius and V_c is the circular velocity of the halo. We fit for the enclosed dark matter mass at 15 kpc, which is approximately the outer edge of our outermost mass bin.

The other three parameters of our galaxy model encode the intrinsic shape of NGC 2693. Previous dynamical studies used angles (θ,ϕ,ψ), or axis ratios $(u,p,q) = (a'/a, b/a, c/a)$, to relate the projected and intrinsic shapes of a triaxial galaxy. Here, u is a compression factor relating the intrinsic (unprimed) and projected (primed) length scales; p is a ratio between the intrinsic intermediate axis b and the intrinsic major axis a (with projected major axis a'); and q is the ratio between the intrinsic minor axis c and the intrinsic major axis. Additionally, $q' = b'/a'$ describes the projected flattening of the MGE component. In general these axis ratios are different for each MGE component as those components have different projected flattenings.

We instead adopt the new parameters $(T, T_{\rm maj}, T_{\rm min})$ introduced in Quenneville, Liepold, and Ma [141]:

$$T = \frac{1-p^2}{1-q^2}\,, \quad T_{\rm maj} = \frac{1-u^2}{1-p^2}\,, \quad T_{\rm min} = \frac{(uq')^2-q^2}{p^2-q^2}\,, \tag{2.2}$$

where T is the commonly used triaxiality parameter, $T_{\rm maj}$ parametrizes the length of the projected major axis relative to the minimum value b and maximum value a, and $T_{\rm min}$ parametrizes the length of the projected minor axis relative to the minimum c and maximum b. The three parameters $T, T_{\rm maj}$ and $T_{\rm min}$ form a convenient unit cube, each with an allowed range of 0 to 1. They have a number of additional desirable properties when compared to the axis ratios (u,p,q) or angles (θ,ϕ,ψ); see Section 3.4 of Quenneville, Liepold, and Ma [141]. Note that while these shape parameters are expressed in terms of the axis ratios in

Equation (2.2), they are constant for different MGE components when the PAs of the MGE components are identical. As shown in Equations (8) and (A2) in Quenneville, Liepold, and Ma [141], the angles (θ, ϕ, ψ) can be directly computed from a $(T, T_{\rm maj}, T_{\rm min})$ triplet and vice versa.

Latin Hypercube Sampling and Bayesian Search

As in Quenneville, Liepold, and Ma [141], we use the grid-free Latin hypercube sampling method [120] to search the 6D model parameter space: $M_{\rm BH}$, M^*/L, M_{15}, T, $T_{\rm maj}$, and $T_{\rm min}$. Latin hypercube sampling is becoming increasingly common in computer-designed experiments due to the simplicity of the sampling algorithm and the desirable space-filling properties in high dimensional parameter spaces. We adopt the Latin hypercube scheme described in Jin, Chen, and Sudjianto [85] and implemented in the `Python` package `SMT` [20].

In this method, we first divide each dimension of our search-space into N cells, where N is the number of galaxy models in a Latin hypercube batch. We then uniformly sample points in each dimension until each cell contains a point, uniformly filling the space. We note that we use the "center" dispersal criterion in `SMT`, which places new points in the center of each hypercube cell. The result is a set of model points spanning six dimensions more uniformly than a regular grid and allowing for a more representative sampling of the likelihood function as a function of the six model parameters.

When drawing points from intrinsic-shape space, we opt to sample uniformly in $\sqrt{T_{\rm maj}}$ and $\sqrt{T_{\rm min}}$ rather than in $T_{\rm maj}$ and $T_{\rm min}$. For nearly axisymmetric galaxies, this sampling space results in fewer unrealistically flat models, increasing the efficiency of our parameter search.

After running preliminary searches over broad ranges of parameters, we choose the uniform prior ranges of $M_{\rm BH} \in [0, 4] \times 10^9 M_\odot$, $M^*/L \in [2.0, 2.85]\ M_\odot/L_\odot$, $M_{15} \in [1, 13] \times 10^{11} M_\odot$, $T \in [0.15, 0.65]$, $T_{\rm maj} \in [0.0, 0.6]$, and $T_{\rm min} \in [0.0, 0.4]$ for our parameters. After each hypercube realization of roughly 1000 galaxy models, we model the χ^2 likelihood landscape as a function of the six parameters using Gaussian process regression. We construct posterior distributions of the space and estimate of the best-fit values for each parameter using dynamic nested sampling [170]. To test for convergence in our model sampling, we perform jackknife resampling where the regression and parameter inference is repeatedly performed using subsets of the full suite of models. In total, we generate 8530 galaxy model points which, when jackknife-resampled, converge on the same best-fit galaxy parameters.

To map the high-likelihood region in fine detail and to serve as an additional test for convergence from our hypercube iterations, we perform one more independent check of our best-fit parameters. We again perform a 6-D gaussian process regression function to the χ^2 landscape produced by the 8530 models described above. We then sample 1000 additional model points with another hypercube, rejecting those which fall outside of the 3σ confidence volume, as estimated by that regression fitted to the previous 8530 model points. The rejection sampling procedure very efficiently populates the χ^2 minimum. Of the 1000 points

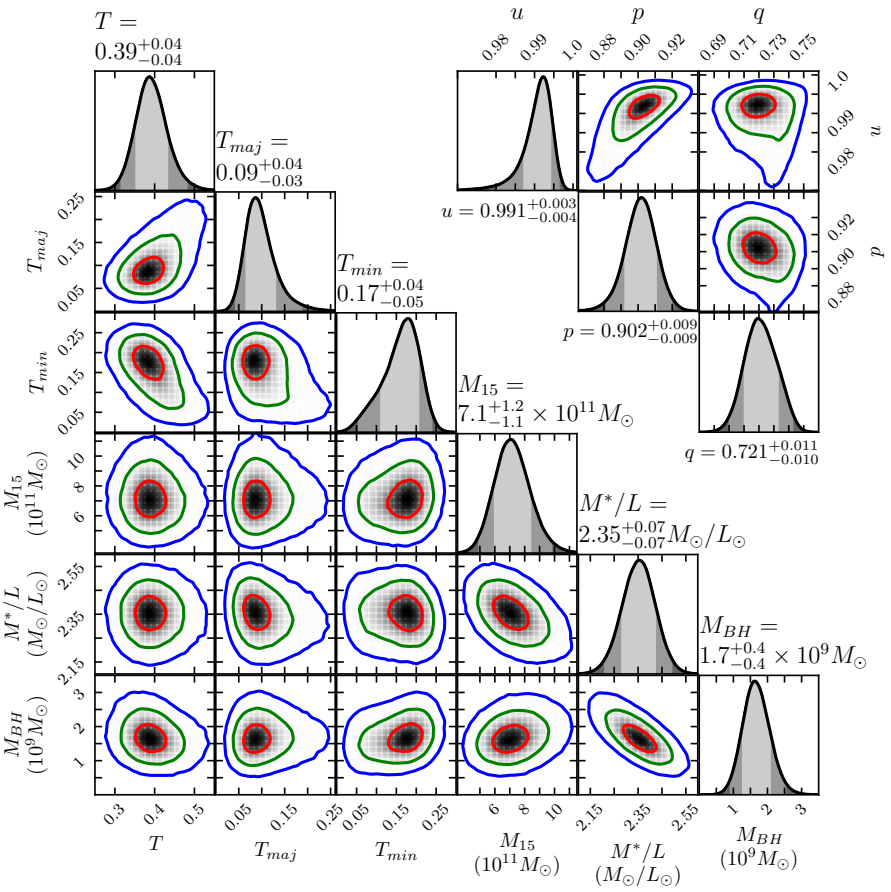

Figure 2.5: (Lower left) 1D and 2D marginalized posteriors for the triaxial orbit models of NGC 2693 described in the text. We marginalize over a smoothed 6D landscape generated with Gaussian process regression. The 1σ, 2σ, and 3σ contours are represented by the curves in red, green, and blue respectively, and as different shade of grey in the 1D panels. Above each 1D posterior distribution are the extracted best-fit values and 1σ confidence intervals. (Upper right) 1D and 2D marginalized posteriors in the axis-ratio space of (u, p, q). Below each 1D posterior are the best-fit values and 1σ confidence intervals.

in that sample, $\sim 9\%$ lie within the 3σ confidence volume for 6 parameters ($\Delta\chi^2 \approx 20.06$), compared to just $\sim 4\%$ from the uninformed 8530-point sample.

Both the uniform hypercube of 8530 models and the 1000 rejection-sampled hypercube models converge on the same best fit parameters. We include both sets here. The resulting 6D posterior distribution of our 9530 production run models is shown in Figure 4.4. We determine the best-fit value and uncertainties by fitting the χ^2 landscape with Gaussian process

regression with a squared-exponential covariance kernel and sampling that landscape with the dynamic nested sampler described in [170]. A uniform prior is assumed for all parameters. The $1\sigma, 2\sigma$, and 3σ confidence regions in 1D and 2D are computed from the posterior distribution marginalized over all other dimensions. These confidence levels correspond to $\Delta\chi^2 = 1, 4$, and 9 in 1-D and $\Delta\chi^2 \approx 2.3, 6.2, 11.8$ in 2D.

Best-Fit Triaxial Model

The best-fit galaxy model is an excellent fit to the observed stellar kinematics, shown in Figure 2.4. The best-fit parameters from the 6D posterior distribution in Figure 4.4 are listed in Table 4.1. The total χ^2 of the best-fit triaxial model is 265.9, with 19.7 from the higher-order moments which are constrained to be $0.0 \pm \delta$. As a test, we have repeated the regression using only four Gauss-Hermite moments measured from the spectra while setting h_5 and beyond to $0.0 \pm \delta$ described above. The best-fit $M_{\rm BH}$ is within 0.5σ confidence interval of the fiducial model in Table 4.1, but the uncertainties on $M_{\rm BH}$ in this case increase by $\sim 10\%$. The same trend is reported in Table 2 of Liepold et al. [105].

Galaxy Parameter	Triaxial Orbit Model	Axisymmetric Orbit Model	JAM Model
$M_{\rm BH}$ $[10^9 M_\odot]$	1.7 ± 0.4	2.4 ± 0.6	2.9 ± 0.3
M^*/L $[M_\odot/L_\odot]$	2.35 ± 0.07	2.27 ± 0.1	2.17 ± 0.03
M_{15} $[10^{11} M_\odot]$	$7.1^{+1.2}_{-1.1}$	7.9 ± 1.3	4.7 ± 0.2
β_z	See caption.†	See caption.†	0.07 ± 0.01
T	0.39 ± 0.04		
$T_{\rm maj}$	$0.09^{+0.04}_{-0.03}$		
$T_{\rm min}$	$0.17^{+0.04}_{-0.05}$		
u	$0.991^{+0.003}_{-0.004}$		
p	0.902 ± 0.009		
q	$0.721^{+0.011}_{-0.010}$		
$\theta\,(^\circ)$	66^{+4}_{-3}		
$\phi\,(^\circ)$	72 ± 3		
$\psi\,(^\circ)$	$93.0^{+0.7}_{-0.6}$		

Table 2.2: Summary of best-fit galaxy models for NGC 2693. For each parameter, we marginalize over the other dimensions and report the 1σ uncertainties. The axisymmetric orbit models and JAM models have fixed inclination of 70°. In orbit models, θ is the inclination angle in the oblate axisymmetric limit ($\psi = 90^\circ$, or equivalenly $p = 1$), with $\theta = 90^\circ$ being edge-on and $\theta = 0^\circ$ being face-on. †We measure β_z in the orbit model as a function of radius, shown in the bottom panel of Figure 4.5. The best-fit JAM value of $\beta_z = 0.07 \pm 0.01$ is consistent with the range of β_z values measured from this best-fit model, with values ranging from $\beta_z = -0.27$ at small radii to $\beta_z = 0.28$ at large radii in both the triaxial and axisymmetric Schwarzschild models.

As we will discuss further in Section 6.1, our inferred $M_{\rm BH} = (1.7 \pm 0.4) \times 10^9 M_\odot$ for the SMBH in NGC 2693 is within the intrinsic scatter of the SMBH-galaxy scaling relations. For the intrinsic shape of NGC 2693, we can compare our inferred axis ratios $(p, q) = (0.902 \pm 0.009, 0.721^{+0.011}_{-0.010})$ with the mean galaxy shapes for 49 slow-rotating galaxies in the MASSIVE survey from Ene et al. [52]. In that work, based on the observed ellipticity and misalignment between the kinematic and photometric axes, the mean flattening of the galaxy sample was estimated statistically to be $(p, q) = (0.88, 0.65)$, with 56% of galaxies having $p > 0.9$. The triaxial shape of NGC 2693 is therefore quite close to the mean values. NGC 1453, the other MASSIVE galaxy for which we have performed triaxial orbit modeling [141], has best-fit shape parameters of $(p, q) = (0.93, 0.78)$, indicating a slightly less flattened shape than NGC 2693 and the mean MASSIVE galaxy. Additionally, the intrinsic shapes of NGC 2693 and NGC 1453 are consistent with the distribution of shapes of fast rotators found in the IllustrisTNG50 and IllustrisTNG100 simulations [137], where the mean axis ratios are $(p, q) \sim (0.9, 0.52)$ and the dispersion is $\sigma \sim 0.15$ for the most massive fast rotating elliptical galaxies.

We note that by construction, the axis ratios (p, q, u) of each MGE component obey the relation $0 \leq q \leq uq' \leq p \leq u \leq 1$ (see, e.g., Sec. 2.1 of Quenneville, Liepold, and Ma [141]). For the MGE of NGC 2693, the most flattened component has $q' = 0.684$. For physically useful deprojections, we may expect $q \gtrsim 0.2$ [14]. The allowed ranges of (p, q, u) are therefore quite narrow, in particular for u, which is constrained to be between ~ 0.9 and 1. The errors on these parameters in Table 2, while appearing small on absolute terms, are on the order of $\sim 5 - 10\%$ of the allowed ranges.

We also highlight that the recovered viewing angle $\theta = 66^{\circ +4^\circ}_{-3^\circ}$, which corresponds to the galaxy's inclination in the oblate axisymmetric limit, is consistent with the inclination of the galaxy estimated from the nuclear dust disk at NGC 2693's center, which we measure to be $i \approx 70^\circ$.

We have also run two additional galaxy models using the best-fit parameters shown in Table 4.1, but with $M_{\rm BH} = 0$ and $M_{\rm BH}$ twice the best-fit value to assess what features in the kinematics provide the black hole mass constraint. Both models are a worse fit to the kinematic data, giving a $\Delta\chi^2 = 38.1$ when there is no black hole present, and a $\Delta\chi^2$ of 17.9 when the black hole is twice as massive. As expected, the inner kinematic data provide significant constraints on $M_{\rm BH}$, with $\sim 30\%$ and 50% of the additional $\Delta\chi^2$ coming from the inner $\sim 1''$ data for the two test cases, respectively.

We use the computed orbit libraries to calculate the orbital composition, as well as the radial velocity dispersion σ_r and tangential velocity dispersion $\sigma_t \equiv \left(\sigma_\theta^2 + \sigma_\phi^2\right)/2$ of NGC 2693. We present the orbital fractions and two anisotropy parameters β and β_z as a function of radius in Figure 4.5. Long-axis tubes and box orbits, both of which are only present in triaxial potentials, make up $\sim 40\%$ of the orbits at small radii and 35% of the orbits at outer parts of the galaxy. Near the center of the galaxy, the orbits are mostly tangential with $\beta < 0$ but become radially anisotropic beyond ~ 1 kpc.

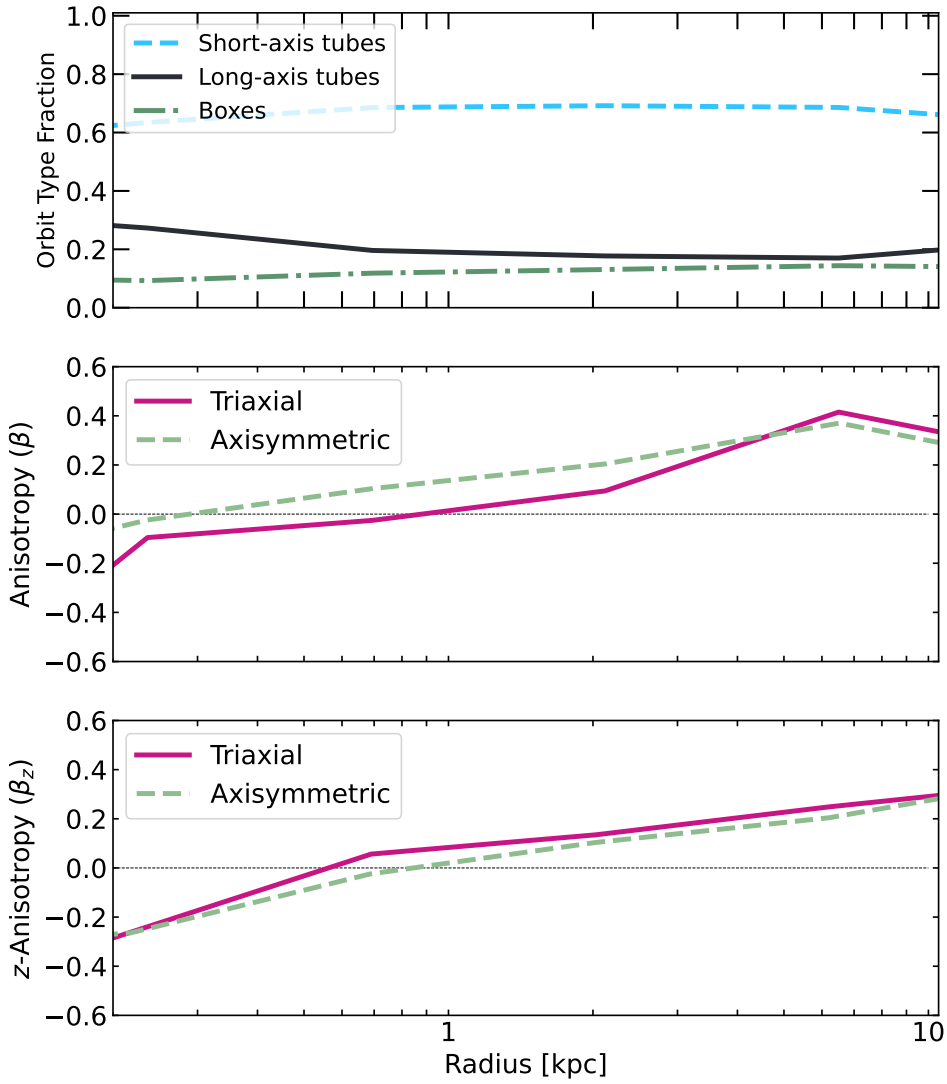

Figure 2.6: (Top) Fraction of orbital weights in each orbital family for the best-fit triaxial galaxy model. The orbital structure is dominated by short-axis tubes at all radii, with a non-zero fraction of the weights occupied by long-axis tubes and box orbits, both of which are present only in triaxial potentials. For axisymmetric models, short-axis tubes are the only allowed orbital family. (Middle) Velocity anisotropy $\beta \equiv 1 - \sigma_t^2/\sigma_r^2$ profile of the best-fit triaxial model (pink, solid line) and best-fit axisymmetric model (green, dashed line) of NGC 2693. Inner orbits are tangential out to $\sim$ 1 kpc and are increasingly radially anisotropic at larger radii in both the axisymmetric and triaxial cases. (Bottom) Anisotropy parameter $\beta_z = 1 - (\sigma_z/\sigma_R)^2$, where σ_z and σ_R are the velocity dispersions parallel to the rotation axis and in the radial direction, for the best-fit axisymmetric and triaxial models described in the text.

2.5 Axisymmetric Dynamical Modeling of NGC 2693

For a comparison study, we have performed axisymmetric modeling of NGC 2693 using both the orbit superposition method and Jeans modeling. We describe the results from each method below.

Schwarzschild Orbit Modeling in the Axisymmetric Limit

We use the axi-symmeterized version of the TriOS code first described in Quenneville, Liepold, and Ma [140], with further improvements in mass binning and acceleration table discussed in Quenneville, Liepold, and Ma [141]. Liepold et al. [105] first applied this code to NGC 1453; here we use similar settings to achieve axisymmetry within the triaxial TriOS code. We ensure the low L_z space is well sampled by tube orbits and do not include the box orbit library (which has $L_z = 0$) explicitly. We set the viewing angle ψ sufficiently close to 90° in the input parameter file, i.e., $|\psi - 90°| = 10^{-9}$, to ensure no long-axis tube orbits are present. For the remaining short-axis tube orbits, we enforce axisymmetry by making 40 copies of each orbit, each copy rotated successively by $2\pi/40$ about the intrinsic minor axis of the galaxy (Section 3 of Quenneville, Liepold, and Ma [140]). These three precautions are necessary to run the triaxial code in the axisymmetric limit and obtain robust parameter constraints. We choose $(N_{I_2}, N_{I_3}, N_{dither}) = (9, 9, 3)$ for the phase space sampling, and include two copies of the integrated orbit library in our minimization. This gives a total number of $174,960$ orbits for our axisymmetric galaxy models.

We search for the best-fit galaxy model using the Latin hypercube scheme outlined in Section 3 over three dimensions: $M_{\rm BH}$, M^*/L, and M_{15}, with a fixed inclination angle $i = 70°$, estimated from the nuclear dust disk. Our hypercube consists of 2000 galaxy models drawn from a range $M_{\rm BH} = [0, 4] \times 10^9\ M_\odot$, $M^*/L = [1.8, 2.8]\ M_\odot/L_\odot$, and $M_{15} = [1, 13] \times 10^{11}\ M_\odot$. The best-fit axisymmetric model parameters are listed in Table 4.1.

Our best fit axisymmetric model of NGC 2693 prefers a $\sim 40\%$ larger $M_{\rm BH}$ compared to the triaxial case, though the recovered best-fit M^*/L and dark matter halo are consistent with triaxial modeling at the 1σ level. By construction, axisymmetric models produce bisymmetric kinematic maps, meaning that the LOSVDs are symmetric about the photometric major axis and anti-symmetric for points mirrored about the photometric minor axis. By contrast, LOSVDs in triaxial models are only point-symmetric about the origin. The apparent minor-axis rotation in "Non-bisymmetric Data Component" panel of Figure 2.7 therefore can be fit by triaxial models but not axisymmetric models. Our best-fit axisymmetric model fails to account for this component (lower middle panel), while our best-fit triaxial model captures well the full velocity features and produces featureless and nearly zero residuals (lower right panel). Our best-fit axisymmetric model fails to account for this component (middle, left panel), while our best-fit triaxial model captures well the full velocity features and produces featureless and nearly zero residuals (middle, right panel).

We have run an additional test to verify that the non-bisymmetric component of the kinematics show in Figure 2.7 is due to a physical non-alignment between the photometric

and kinematic axes and can not be simply "rotated away". In this test, instead of using the best-fit photomertic PA 167.9° given by the MGE (see Sec. 2.1), we inflate the photometric PA to be 175°, a value that would minimize the magnitude of the non-bisymmetric component. Using this inflated PA, we then refit the MGE and re-compute the non-bisymmetric component of our input kinematics. Figure 2.8 compares the result for this test (bottom panel) with that of our fiducial PA (top panel). While the non-bisymmetric feature is indeed much reduced for PA = 175°, the MGE isophotes for this PA provide a noticeably worse fit to the observed surface brightness profile at both at large and small radii.

Lipka and Thomas [109] recently argued that edge-on axisymmetric models have a larger model flexibility than face-on projections and thus can fit observational data better, biasing the recovered inclination towards $i \sim 90°$. The rationale is that in edge-on models, the prograde and retrograde orbits have opposite velocities along the line of sight and contribute uniquely to the model's LOSVDs, whereas in face-on models, the two sets of orbits have negligible line-of-sight velocities, making them virtually interchangeable and effectively reducing the number of unique orbits used in superposition and minimization routines. They reported a $\Delta\chi^2 \sim 30$ bias, favoring edge-on inclinations. We have performed a parameter search including inclination as a fourth model parameter, sampling 1000 values from $i = [68°, 89°]$ in the hypercube. Our regression find a best fit value $i = 87.6°^{+0.9°}_{-1.8°}$, with a $\Delta\chi^2$ between the lowest and highest inclinations of ~ 25, slightly smaller than that reported in Lipka and Thomas [109]. Despite this preference for edge-on inclinations in the axisymmetric models, our best-fit $M_{\rm BH}$ and M^*/L barely change when we include inclination as a free parameter: $M_{\rm BH} = (2.4 \pm 0.5) \times 10^9\ M_\odot$ and $M^*/L = (2.23 \pm 0.1) M_\odot/L_\odot$. These are both consistent within the confidence intervals of the $i = 70°$ results, so our results are robust to choice of inclination angle.

Jeans Anisotropic Models

We further model the stellar kinematics of NGC 2693 as an axisymmetric system using Jeans anisotropic modeling (JAM; Cappellari [33, 31]). JAM solves the Jeans equations assuming a velocity ellipsoid that is aligned with a cylindrical coordinate system (R, z, ϕ) or a spherical coordinate system (R, θ, ϕ). We adopt a cylindrically aligned velocity ellipsoid, which is flattened along the z-axis and is characterized by the anisotropy parameter $\beta_z = 1-(\sigma_z/\sigma_R)^2$, where σ_z and σ_R are the velocity dispersions parallel to the rotation axis and in the radial direction. JAM has the advantage of being computationally inexpensive and previous studies generally have found similar results between (axisymmetric) Schwarzschild models and JAM (e.g., Seth et al. [161], Krajnović et al. [95], and Thater et al. [174]).

In our model, the gravitational potential comes from the BH, stars, and dark matter. The galaxy's surface brightness from Table 2.1 is deprojected into a 3D stellar mass density given an inclination angle, $i = 70°$, and M^*/L, while the dark matter halo is parametrized by the logarithmic profile in Equation (2.1). Thus, the free parameters in our model are: $M_{\rm BH}$, M^*/L, M_{15} (the dark matter mass enclosed within 15 kpc), and β_z. Given these parameters and the GMOS PSF, JAM predicts the second moment, which we compare to the observed

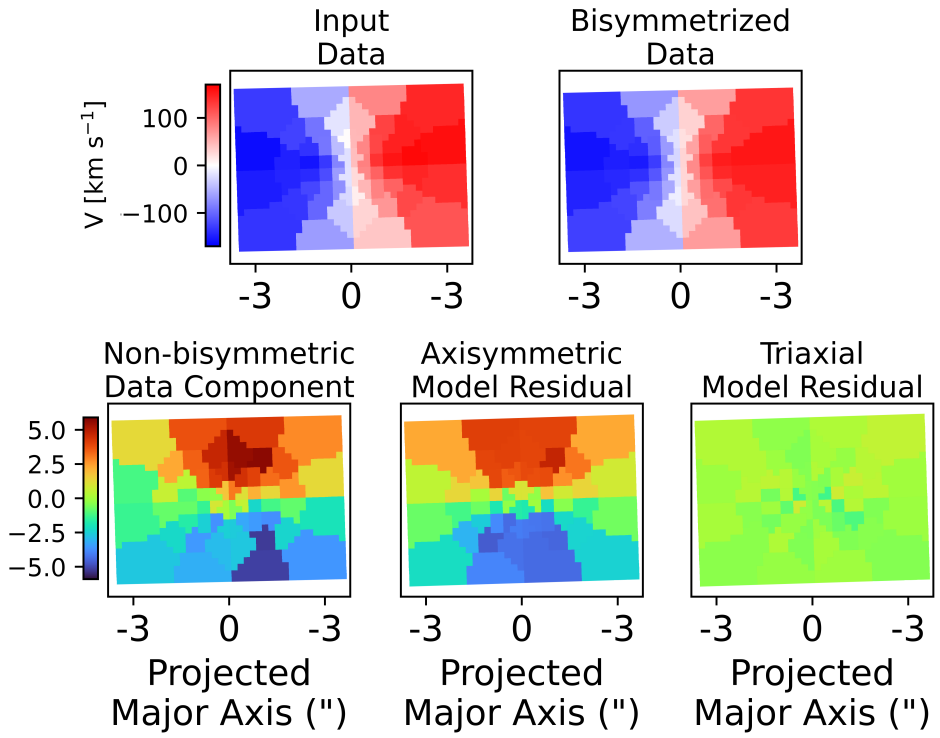

Figure 2.7: Observed velocity map of the central $5'' \times 7''$ of NGC 2693 (upper left), oriented such that the observed photometric major and minor axes are horizontal and vertical, respectively, where the best-fit MGE PA is 167.9°. We decompose the map into a bisymmetrized component (upper right) and a non-bisymmetric component (lower row), where bisymmetry means symmetry for points mirrored about the photometric major axis and anti-symmetry for points mirrored across the photometric minor axis. The non-bisymmetric component (normalized by measurement uncertainty) shows a prominent apparent minor-axis rotation, a telltale sign of triaxiality. Since axisymmetric models can only produce bisymmetric velocity maps by construction, the residuals from our best-fit axisymmetric model (lower middle) shows a similar pattern as the non-bisymmetrized map. By contrast, our best-fit triaxial model (lower right) is able to reproduce the full observed velocity structure, and the residuals scatter randomly about 0.

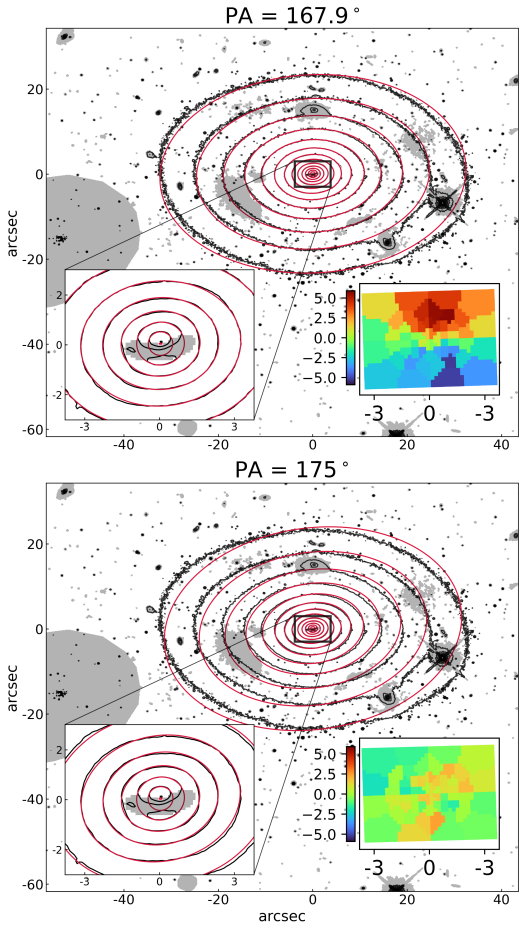

Figure 2.8: Illustration of the non-alignment between the photometric PA and kinematic features. The upper panel repeats the *HST* (black) and MGE model isophotes (red) in Figure 2.1 and the non-bisymmetric component of the GMOS data in Figure 2.7. The best-fit MGE PA of the photometric major axis is 167.9° in this fiducial case. In the lower panel, we inflate the MGE PA to 175° and plot the resulting model fits and non-bisymmetric map assuiming this PA. While the non-bisymmetric velocity pattern is minimized, this inflated PA provides a poor fit to the observed surface brightness profile.

$V_{\rm rms}$, with $V_{\rm rms} = \sqrt{(V^2 + \sigma^2)}$. We use the point-symmetrized V and σ from the GMOS and Mitchell observations, excluding the innermost Mitchell kinematics that spatially overlap with the GMOS kinematics. We additionally exclude the outermost four Mitchell bins as was done in the Schwarzschild models in earlier sections.

The model parameters are optimized using Bayesian inference and the nested sampling code `Dynesty` [170], which estimates posteriors and evidences. We adopted a likelihood

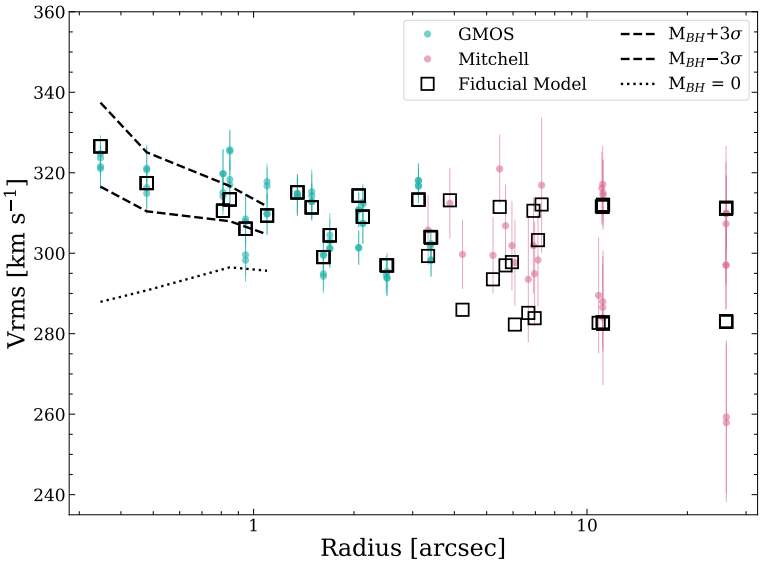

Figure 2.9: Line-of-sight rms velocity (V_{rms}) determined from the GMOS (blue dots) and Mitchell (pink dots) IFS kinematics. The best-fit JAM model is shown with black open squares. Also shown are three JAM models with $M_{\rm BH}$ fixed to $0 M_{\odot}$ (dotted line), $2.1{\times}10^{9}$ $M_{\odot}$ (the 3σ lower bound; dashed line), and 3.7×10^{9} $M_{\odot}$ (the 3σ upper bound; dashed line). The three models extend over all radii, although only the model predictions within the central region are plotted. Beyond $\sim 1''$, it is difficult to distinguish between the models. The best-fit model is a good match to the observations and the model without a SMBH underestimates V_{rms} at the nucleus.

$L \propto \exp(-\chi^2/2)$ where $\chi^2 = \Sigma_i (D_i - M_i)^2/\sigma_i^2$ and D_i and M_i are the observed and model $V_{\rm rms}$, respectively, and σ_i is the $V_{\rm rms}$ uncertainty for each spatial bin. When running with `Dynesty`, we use 500 live points and stop the initial sampling stage once reaching a threshold of 0.05, which is the log-ratio between the current estimated Bayesian evidence and the remaining evidence. The batch sampling stage is stopped when the fractional error on the posterior reaches 0.02. We assume uniform priors, with all free parameters sampled linearly. The best-fit values and 1σ uncertainties are taken to be the median and 68% confidence intervals of the posterior distributions, respectively.

The results are shown in Table 4.1 and the comparison between the best-fit model and the observed $V_{\rm rms}$ is given in Figure 2.9. The model reproduces the data well, with a reduced χ^2 of 1.07. Figure 2.9 also displays three models with $M_{\rm BH}$ set to 0 $M_{\odot}$, 2.1×10^{9} $M_{\odot}$ (the 3σ lower bound), and 3.7×10^{9} $M_{\odot}$ (the 3σ upper bound), with M^*/L, M_{15}, and β_z fixed to the values from the best-fit JAM model in Table 4.1. The $M_{\rm BH} = 0$ $M_{\odot}$ case fails to match the kinematics in the inner region and further demonstrates the need for a black hole in the galaxy potential. The $M_{\rm BH}$ and M^*/L from the best-fit JAM model are consistent within 1σ

of the axisymmetric Schwarzschild model results in Section 2.5, and β_z falls within the range of values extracted from the best-fit axisymmetric Schwarzschild model. The M_{15} value from JAM is lower than the Schwarzschild model result, but it remains consistent at the 2σ level. Liepold et al. [105] found a similar result in the analysis of NGC 1453, with JAM favoring a value of M_{15} half that inferred from the axisymmetric Schwarzschild models.

We complete additional JAM runs to test assumptions made during the modeling. In our fiducial model, we fix $i = 70°$, which is the inclination angle inferred from the dust disk, but we also test allowing i to be a free parameter. We find a preference for $i = 81°$, however all the angles for which the MGE could be deprojected fall within the 3σ uncertainties. In addition, we test using a spatially varying anisotropy, with a parameter ($\beta_{z,\mathrm{in}}$) assigned to the MGE components with $\sigma'_k < 3''$ and another parameter ($\beta_{z,\mathrm{out}}$) attributed to the remaining MGE components. We then examine a case where $\beta_{z,\mathrm{in}}$ corresponded to the MGE components with $\sigma'_k < 6''$. These choices were motivated by the previously run Schwarzschild models, which suggested a change in the anisotropy between a radius of $\sim 3 - 6''$. Next, we fit to only the GMOS data, which extend to a radius of $3''.4$, and we assume a spatially constant anisotropy. Finally, we test including the Mitchell kinematics from the outer spatial bins during the fit, adopting an modified MGE constructed using a dust mask with fewer central pixels flagged, and increasing the number of live points and applying different sampling thresholds in `Dynesty`. Even when changing the model in these various ways, we nearly always find consistent results at the 1σ level with the fiducial model. The exception is when we fit to only the GMOS data with a spatially constant β_z; we find that M^*/L is consistent within the 2σ uncertainties while the remaining parameters are in agreement at the 1σ level with the fiducial model.

The above work assumed a cylindrically aligned velocity ellipsoid, but we also examine using spherically aligned JAM. In this case, we find a large anisotropy, with $\beta = 1-(\sigma_\theta/\sigma_r)^2 = 0.39$ and an order-of-magnitude smaller M_{BH} with 3σ uncertainties that extend to 0 $M_\odot$. We also fit spherically aligned JAM to only the GMOS kinematics and recover the same results. When repeating the run and fixing $\beta = 0.0$, we find that M_{BH} is constrained with a best-fit value of 3.4×10^9 $M_\odot$. In this case, the M_{BH} and remaining parameters are consistent with the fiducial (cylindrically aligned) JAM model given the 1σ uncertainties.

Despite the assumptions of cylindrically aligned JAM, the inferred M_{BH} and M^*/L match (at the 1σ level) the results from the more complex axisymmetric orbit model in Section 2.5 (Table 4.1). The enclosed dark matter mass from JAM is $\sim 40\%$ lower than that from the axisymmetric orbit model, but it is within 2σ uncertainties of the orbit model. As Table 4.1 shows, the uncertainties in the best-fit parameters from JAM tend to be much smaller than those from the axisymmetric orbit model. We continue to see a shift in the M_{BH} compared to the best-fit value from the triaxial Schwarzschild model, with the JAM value being 75% more massive than the value predicted from the triaxial modeling; see Section 6.2 for further discussion.

2.6 Discussion

Black Hole Scaling Relations

To place the NGC 2693 SMBH on the $M_{\rm BH} - \sigma$ relation, we use the luminosity-weighted velocity dispersion within R_e, $\sigma = 296\,km\ s^{-1}$, from Veale et al. [188] for NGC 2693. This measurement was obtained from the same Mitchell IFS data used in this paper. The mass of the NGC 2693 SMBH is within 15% of the value predicted by the mean $M_{\rm BH} - \sigma$ relation in McConnell and Ma [118] and $\sim 5\%$ above the relation in Saglia et al. [151]; it is within the intrinsic scatter of both relations, with values of 0.38 dex and 0.417 dex, respectively.

For the $M_{\rm BH} - M_{\rm bulge}$ relation, we use the total stellar mass of NGC 2693 from our best-fit triaxial model, $M^* = 7.2 \times 10^{11}\ M_\odot$, as the bulge mass.[3] The NGC 2693 $M_{\rm BH}$ is $\sim 25\%$ smaller than the value predicted by the mean $M_{\rm BH} - M_{\rm bulge}$ relation of McConnell and Ma [118] and $\sim 18\%$ smaller than the value predicted by the Saglia et al. [151] relation. Again, this SMBH is within the intrinsic scatter of both relations, with values of 0.34 and 0.535 dex, respectively.

Comparison of Triaxial and Axisymmetric Models

There are few studies that compare $M_{\rm BH}$ determination from fully triaxial stellar dynamical models to axisymmetric models of the same galaxy. The best-fit $M_{\rm BH}$ for both M32 [182] and NGC 1453 [105, 141] were unchanged when relaxing the assumption of axisymmetry, whereas $M_{\rm BH}$ in NGC 3379 increased by a factor of ~ 2 in the triaxial case [182]. We note that the mass modeling performed for M32 and NGC 3379 did not simultaneously model the dark matter halo of the two galaxies. In comparison, we make no assumptions on the dark matter halo of NGC 2693, and instead constrain the dark matter mass at 15 kpc directly as was done for NGC 1453 [141]. Furthermore, the triaxial code of van den Bosch et al. [183] had an incorrect scheme for mirroring orbits, which we fixed in the TriOS code used for NGC 1453 and NGC 2693 here.

In the case of NGC 3998, Walsh et al. [194] applied the triaxial code of van den Bosch et al. [183] and considered different dark matter halos. The grid-based parameter search did not allow for simultaneously varying all parameters in their model. While NGC 3998 was not modelled in the axisymmetric regime, the gas-dynamical measurement of $M_{\rm BH}$ disagreed with the stellar-dynamical value by a factor of ~ 4 [45].

Recently, Brok et al. [23] applied the van den Bosch et al. [183] code to the brightest cluster galaxy PGC 046832 to determine its intrinsic shape, central black hole mass, and orbital composition. The galaxy has a unique velocity map, exhibiting both a kinematically decoupled core and dramatic twists in the velocity field, suggesting a non-axisymmetric intrinsic shape. Their triaxial models prefer prolate galaxy shapes in the inner 10 arcseconds of the galaxy, and oblate shapes beyond 10 arcseconds, though these models only provide an

[3] This is 15% larger than the stellar mass estimated from the ATLAS^{3D} M_K-stellar mass relation [29], using a K-band absolute magnitude of $M_K = -25.76$ [113].

upper bound on the black hole mass of $M_{\rm BH} \lesssim 2 \times 10^9 M_\odot$. While this disagrees considerably with the results from their best-fit axisymmetric models, which prefer $M_{\rm BH} \sim 6 \times 10^9 M_\odot$, it remains to be seen if their triaxial result would change after the incorrect orbit mirroring in the van den Bosch et al. [183] code and other issues discussed in Quenneville, Liepold, and Ma [141] are fixed.

In the case of NGC 2693, the best-fit orbit model in the axisymmetric limit and the best-fit JAM model favor $M_{\rm BH}$ that is 40%-70% higher than the triaxial orbit model, but the difference is within $\sim 2\sigma$ confidence level (see Table 2). Similar comparison studies are needed from more galaxies to assess whether any systematic difference exists in $M_{\rm BH}$ values determined from different methods.

2.7 Summary

We have reported detection of a SMBH with $M_{\rm BH} = (1.7 \pm 0.4) \times 10^9\ M_\odot$ at the center of the massive, fast-rotating galaxy NGC 2693 targeted by the MASSIVE survey. Using HST stellar light profiles and extensive IFS kinematic data covering a FOV from ~ 150 pc to 15 kpc as constraints (Section 5.2), we have performed triaxial orbit modeling with the *TriOS* code to determine the galaxy's internal stellar orbit structure, $M_{\rm BH}$, M^*/L, dark matter content, and intrinsic 3D shape (Section 4.3). We modeled the gravitational potential of NGC 2693 with 6 parameters and performed a 6D Bayesian search using Latin hypercube sampling of $\sim 10,000$ galaxy models to find the model that best matches our input data (Section 5.5).

Despite NGC 2693 exhibiting properties typically indicating an intrinsic axisymmetric shape, we find the best-fit model to be triaxial with $T = 0.39 \pm 0.04$ and intrinsic axis ratios $p = b/a = 0.902 \pm 0.009$ and $q = c/a = 0.721^{+0.011}_{-0.010}$. We find that triaxial models are needed to account for non-axisymmetric features seen in the residuals of our accompanying axisymmetric models (Figure 2.7). When limiting ourselves to axisymmetry, we find 40% larger best-fit black hole mass of $M_{\rm BH} = (2.4 \pm 0.6) \times 10^9\ M_\odot$ from axisymmetric orbit modeling, and 75% larger best-fit black hole mass of $M_{\rm BH} = (2.9 \pm 0.3) \times 10^9 M_\odot$ from JAM modeling (Section 5); both values are within $\sim 2\sigma$ confidence level of $M_{\rm BH}$ determined from triaxial modeling (Table 2).

We have examined orbit flexibility in our galaxy models to assess possible effect of "generalized degrees of freedom" [198, 172] on parameter determinations. Using a similar measure as Lipka and Thomas [109] to estimate the effective number of parameters, we find that our models in the axisymmetric limit have a similar behavior as Lipka and Thomas [109], in which edge-on orientations tend to have higher model flexibility (Section 5.1). Such varying model flexibility can be attributed to varying degeneracy between prograde and retrograde short-axis loop orbits as the line-of-sight approaches the symmetry axis. For triaxial models, however, we find the model flexibility to vary much less in the region around the best-fit models, and our best-fit triaxial shape parameters change by less than 1σ in a number of preliminary tests. It is possible that the additional presence of box and long-axis tube orbits

in triaxial potentials has led to a weaker dependence of model flexibility on viewing angles. We will report the full results in a subsequent paper.

This paper adds to only a handful of other stellar dynamical modeling studies not limited to axisymmetric galaxy shapes (Section 2.6). Most of the remaining galaxies in the MASSIVE survey exhibit more prominent kinematic and photometric twists and less rotation compared to NGC 2693, further providing evidence that massive early-type galaxies have triaxial intrinsic shapes. More stellar dynamical measurements beyond the axisymmetric limit will inform whether the systematic differences in $M_{\rm BH}$ seen for NGC 2693 in this paper is a common occurrence.

Acknowledgements

J.D.P, C.M.L., C.-P.M., and M.E.Q. acknowledge support from NSF AST-1817100, HST GO-15265, HST AR-14573, the Heising-Simons Foundation, and the Miller Institute for Basic Research in Science. J.L.W. and S.C.D.A were supported in part by NSF grant AST-1814799. M.E.Q. acknowledges the support of the Natural Sciences and Engineering Research Council of Canada (NSERC), PGSD3-517040-2018. This work used the Extreme Science and Engineering Discovery Environment (XSEDE) at the San Diego Supercomputing Center through allocation AST180041, which is supported by NSF grant ACI-1548562. Portions of this research were conducted with the advanced computing resources provided by Texas A&M High Performance Research Computing. This work is based in part on data obtained at the international Gemini Observatory, a program of NSF's NOIRLab, which is managed by the Association of Universities for Research in Astronomy (AURA) under a cooperative agreement with the National Science Foundation on behalf of the Gemini partnership: the National Science Foundation (United States), the National Research Council (Canada), Agencia Nacional de Investigación y Desarrollo (Chile), Ministerio de Ciencia, Tecnología e Innovación (Argentina), Ministério da Ciência, Tecnologia, Inovações e Comunicações (Brazil), and Korea Astronomy and Space Science Institute (Republic of Korea). This work is based in part on observations made with the NASA/ESA Hubble Space Telescope, obtained at the Space Telescope Science Institute, which is operated by the Association of Universities for Research in Astronomy, Inc., under NASA contract NAS5-26555. These observations are associated with program GO-14219.

Chapter 3

`TriOS` Schwarzschild Orbit Modeling: Robustness of Parameter Inference for Masses and Shapes of Triaxial Galaxies with Supermassive Black Holes

This chapter tests the reliability of triaxial Schwarzschild orbit modeling using simulated galaxy observations with known input parameters. The goal is to determine whether the `TriOS` modeling framework and parameter-search procedure can recover SMBH mass, stellar mass-to-light ratio, dark matter content, intrinsic shape, and orbital structure when the true galaxy model is known. These mock tests provide an essential validation step before interpreting triaxial orbit-model results for real galaxies. This chapter was originally published as:

Jacob Pilawa, Emily R. Liepold, and Chung-Pei Ma. "TriOS Schwarzschild Orbit Modeling: Robustness of Parameter Inference for Masses and Shapes of Triaxial Galaxies with Supermassive Black Holes". In: The Astrophysical Journal 966, 205 (May 2024). doi: 10.3847/1538-4357/ad3935. arXiv: 2402.16935 [astro-ph.GA].

3.1 Introduction

Since its introduction, the orbit superposition technique of Schwarzschild [158] has become a useful tool for performing detailed dynamical modeling of the internal structures of galaxies. By integrating a set of representative stellar orbits in an assumed gravitational potential, a superposition of orbits is constructed to replicate the stellar kinematics and surface brightness profiles of a galaxy seen in projection. Schwarzschild's method was initially proposed to demonstrate the existence of self-consistent galaxies with triaxial mass distributions. It has

since been extended to allow for fitting of kinematic and photometric observations (e.g., Pfenniger [133], Richstone and Tremaine [146, 147], and Rix et al. [148]) and is used to constrain properties of the host galaxy such as its supermassive black hole mass $M_{\rm BH}$, stellar mass-to-light ratio M^*/L, dark matter content, intrinsic shape, and stellar orbital structure.

Despite the wide application of the Schwarzschild method to real data, its ability to recover known input parameters has only been tested in a handful of cases, each case with different underlying assumptions. Early tests of the Schwarzschild method on simulated data in the three-integral axisymmetric limit highlighted the advantages and challenges posed by the method when it was applied to long-slit kinematic data (e.g., Valluri, Merritt, and Emsellem [180], Cretton and Emsellem [40], and Magorrian [114]). The availability of integral-field spectroscopy (IFS) over the past two decades has led to significantly improved data quality and number of kinematic constraints. An early application of axisymmetric orbit modeling to Sauron IFS data of M32 yielded well constrained $M_{\rm BH}$, M^*/L, as well as the inclination angle, $i = 70^\circ \pm 5^\circ$ [192]. A subsequent study of NGC 2974 (also using Sauron IFS data) obtained well constrained M^*/L and i from axisymmetric modeling of real data, but tests on simulated data found the inclination to be marginally constrained; the authors cautioned the validity of the formal orbit model solution $i = 65^\circ \pm 2.5^\circ$ [98]. Since then, other tests on simulated data using different axisymmetric orbit codes have found a range of results. For instance, Appendix A.3 of Siopis et al. [166] and Appendix C of Quenneville, Liepold, and Ma [142] reported excellent recoveries of $M_{\rm BH}$ and halo circular velocity; Thomas et al. [176] was able to use the orbit method to reconstruct the stellar masses and velocity anisotropies in N-body merger remnants with high accuracy; Vasiliev and Valluri [186] recovered the true values of M^*/L but were unable to put strong constraints on $M_{\rm BH}$ and dark matter halos; Lipka and Thomas [109] discussed the tendency for the inclination angle to be biased towards edge-on due to increased model flexibility.

When the axisymmetric assumption is removed, the Schwarzschild method becomes significantly more complicated and computationally expensive. Triaxial orbit modeling requires specification of three unequal axes (or equivalently, three angles) and integration of new libraries of stellar orbits, so a full exploration of the galaxy parameter space is much more computationally intensive than for axisymmetric models. Accordingly, there have been fewer attempts at performing recovery tests on simulated data. Early tests on mock triaxial Abel galaxies recovered M^*/L and intrinsic axis lengths at 10%-20% accuracy [183, 184]. When the same triaxial code was applied to galaxies in hydrodynamical cosmological simulations, Jin et al. [86] found that depending on the assumed halo profile, the mean stellar mass is under-estimated by 13%-24% and the halo mass is over-estimated by 18%-38%. All these tests, however, used the original 2008 code that had been shown to have 12 wrong signs in some components of the orbital velocities and various other issues [143]. Neureiter et al. [127] reported robust recovery of $M_{\rm BH}$ and M^*/L for several tested orientations of an N-body merger remnant.

In this paper, we conduct a comprehensive study of the ability of the triaxial orbit method to *simultaneously* recover the intrinsic shape and mass parameters of simulated triaxial galaxies containing SMBHs, stars, and dark matter. We have been working to

reduce the computational cost of individual triaxial Schwarzschild models in the triaxial code `TriOS` [142, 143], as well as improve the efficiency in exploring the mass and intrinsic shape parameter space via non-grid-based, likelihood approach to parameter inference. We apply this efficient parameter inference methodology to a suite of simulated triaxial galaxies, testing the ability of `TriOS` to recover known input parameters to our models while all parameters are varied simultaneously.

An additional aim of this paper is to investigate the extent to which our triaxial Schwarzschild orbit models are impacted by varying degrees of statistical complexity in the `TriOS` models. It has been a common practice while performing Schwarzschild modeling to compute a χ^2 value associated with a model's goodness-of-fit to a set of observed constraints, and select the "best-fit" model that minimizes the χ^2. While often effective, this strategy potentially introduces biases due to the variable complexity of the underlying models. Intuitively, if models in some region of the parameter space have more flexibility to fit the observations, those models may have lower χ^2 values as a simple consequence of that flexibility. A more prudent model selection procedure therefore should balance a combination of the fit quality and a measure of the complexity of a model.

It is, however, non-trivial to quantify the complexity of a model. The number of degrees of freedom (DOF) is often used for linear models without constraints because the number of non-redundant free parameters in a model provides a natural measure of the model complexity, or flexibility in overfitting. While subtleties exist in the use of DOF for unconstrained linear models, the problem of how to capture complexity is even thornier for linear models with constraints or priors (and hence with reduced model flexibility), or for nonlinear models [4]. Different forms of complexity measure, or information criterion (IC), for the effective number of parameters in a model have been proposed, e.g., AIC [3], TIC [163], BIC [157], NIC [125], and a Bayesian measure [173]. Ye [198] suggests a generalized DOF that measures how sensitive the model predictions are to perturbations in the model constraints. A model with higher complexity or flexibility is one whose predictions are more responsive to those perturbations. Following Ye [198], Lipka and Thomas [109] constructed an estimate of the complexity of axisymmetric Schwarzschild orbit models. Here we examine the role of penalty terms for triaxial orbit models in simulated galaxies.

The paper is laid out as follows. Section 2 summarizes the Schwarzschild orbit method and our procedure for constructing simulated galaxy kinematics. Section 3 outlines the main results of the paper, including a description of the parameter inference scheme used to compute our parameter estimates and corresponding confidence intervals. In Section 4, we briefly discuss estimating the statistical complexity of triaxial Schwarzschild models, and the extent to which taking into account the model flexibility changes our parameter estimation. Section 5 summarizes the results and the outlook for future triaxial stellar dynamical modeling efforts.

3.2 Dynamical Modeling and Simulated Data

Triaxial Schwarzschild Orbit Modeling

Throughout this work, we perform triaxial Schwarzschild orbit modeling with the `TriOS` code [142, 143], which is based on an earlier unnamed triaxial modeling code [183]. In this method, a stationary gravitational potential is proposed, and a library of orbits spanning the phase space is integrated. A set of weights are assigned to these orbits such that the linear superposition of the orbits can both reproduce the mass distribution associated with the gravitational potential and fit a set of kinematic observations. This procedure enforces self-consistency between the mass distribution and gravitational potential without requiring specific assumptions about the form of the distribution function or velocity anisotropy.

The mass components of a galaxy in `TriOS` can consist of a central SMBH with mass $M_{\rm BH}$, a stellar component with mass-to-light ratio M^*/L, and a dark matter halo. Most prior work using the Schwarzschild orbit method has assumed a spherical or axisymmetric potential; `TriOS` relaxes these assumptions and allows triaxially-shaped 3D stellar mass densities. The stellar mass density is determined by first modeling the 2D (observed) surface brightness distribution of a galaxy as a Multi-Gaussian Expansion (MGE) [30]. For a given set of angles θ, ϕ, and ψ that relate the intrinsic (3D) and projected (2D) coordinate systems, we deproject each component of the MGE and sum them to create the 3D stellar density. Each MGE component (labelled by subscript j) is allowed to have its own 2D axis ratio, q'_j, which is the ratio of the lengths of its semi-minor and semi-major axes. Through the relations in the appendix of Quenneville, Liepold, and Ma [143], the intrinsic axis ratios are determined: $p_j = b_j/a_j$ is the intrinsic middle-to-long axis ratio; $q_j = c_j/a_j$ is the intrinsic short-to-long axis ratio; and u_j is the apparent-to-intrinsic long axis ratio. When performing parameter searches and inferences below, we follow Quenneville, Liepold, and Ma [143] and use an alternative set of shape parameters, T, $T_{\rm maj}$, and $T_{\rm min}$. The definitions and advantages of these parameters are articulated in Sec. 3 of Quenneville, Liepold, and Ma [143].

For each galaxy model, the `TriOS` code samples the phase space with a set of representative stellar orbits and integrates their trajectories. The orbits are initiated in two separate spaces: the x–z and the stationary start spaces, where the $x-$, $y-$, and $z-$axes are directed along the intrinsic major, intermediate, and minor axes of the galaxy, respectively. In each space, N_E values of the orbital energy are sampled. In the x–z start space, orbits of a given energy are initialized on a polar grid in the x–z plane along N_{I_2} rays uniformly spaced in angle from the z-axis to the x-axis, and at N_{I_3} positions along each ray (see Fig. 4 of Quenneville, Liepold, and Ma [143]). Each orbit has initial velocities $v_x = v_z = 0$ and $v_y > 0$. In addition, a set of 'retrograde' orbits are constructed by simply inverting the velocities of orbits in the prograde x–z orbit library, and seven additional copies of each orbit are generated through the mirroring scheme described in Quenneville, Liepold, and Ma [143]. In the stationary start space, orbits of a given energy are initiated with zero velocities at positions on the equipotential surface sampled on a uniform grid over the two spherical angles θ and ϕ. To enhance phase-space sampling, the code allows for "dithering" the initial conditions,

by which the number of sample points along each of the three dimensions of the start space is increased by a factor of $N_{\rm dither}$, resulting in an overall factor of $N_{\rm dither}^3$ increase in the phase space sampling. The properties of bundles of $N_{\rm dither}^3$ adjacent orbits are averaged and each bundle of orbits is given a single orbital weight when constructing the superposition.

Each orbit is projected onto the sky and its line of sight velocity distribution (LOSVD) within $N_{\rm bin}$ spatial apertures is stored. Its mass distribution in a 3D grid is also stored. We perform a non-negative least squares (NNLS) optimization to determine a set of orbit weights such that the superposition of orbits reproduces both the 3D stellar mass distribution (obtained from de-projection of observed surface brightness distribution) and the observed LOSVD in each spatial bin. The LOSVD is characterized by a set of Gauss-Hermite moments [117], and the NNLS objective function consists primarily of the χ^2 associated with the reproduction of those observed moments (see Equation 4.1). The models contain $N_{\rm kin}$ kinematic constraints, which is equal to the product of the number of spatial apertures and the number of Gauss-Hermite moments used to characterize the LOSVDs. The mass self consistency is enforced by adding additional χ^2-like terms to the NNLS objective function that are associated with the mismatch between the input's and model's mass in each of the 3D grid cells and within each of the 2D spatial apertures with a 1% error imposed on each mass. The phase-space distribution function for the galaxy model can be understood as being composed of this set of orbit weights.

Generation of Simulated Galaxy Data

We use the Schwarzschild method to create simulated stellar kinematics for a suite of model galaxies, each of known mass components and a known intrinsic shape. For the simulated data to provide useful insight into actual observations, we opt to create stellar kinematics that mimic those observed in real galaxies. We achieve this by building the simulated galaxy kinematics using the measured kinematics of a real galaxy as a template. Here we use the kinematics of NGC 2693 presented in Pilawa et al. [135], which are typical of those known for massive elliptical galaxies in the MASSIVE survey [113]. Since these kinematics are only used as a starting template, we do not expect the main conclusions of this paper to depend strongly on the particular galaxy choice. We note that while the velocity anisotropy profiles investigated here tend to be tangential at small radii and radial at large radii (Fig. 6 of Pilawa et al. [135]; Fig. 3.3 here), this profile is not unique to NGC 2693. Similar profiles are found for many massive galaxies that have been studied with the orbit modeling method (e.g., Extended Data Figure 6 of Thomas et al. [177]). A different procedure would be needed to produce a qualitatively different velocity anisotropy profile.

Six parameters were determined for NGC 2693: SMBH mass $M_{\rm BH}$, the stellar mass-to-light ratio M^*/L, the dark matter mass enclosed within a radius of 15 kpc M_{15}, and three shape parameters (T, $T_{\rm maj}$, $T_{\rm min}$), or equivalently, the luminosity-averaged axis ratios (p, q, u). The dark matter halo is logarithmic with a fixed scale radius $R_c = 15$ kpc. To generate simulated stellar kinematics for a given galaxy model G_i listed in Table 1, we first run `TriOS` to compute the orbit libraries representing this galaxy and determine the set

of orbit weights with a regularization scheme (see below) such that the model's projected kinematics best reproduce those of real observations of NGC 2693. We then perturb this model's noise-free projected kinematics with Gaussian noise with seed r and an amplitude set by the observed uncertainties on each measurements.

While determining the orbital weights of the simulated galaxies described above, we incorporate the distribution function regularization scheme outlined in Section 5.2 of van den Bosch et al. [183]. This scheme penalizes the goodness-of-fit statistic when fitting the orbital weight distribution by a term proportional to the second derivative of the orbital weights with respect to the orbits' indices in their start space. This procedure yields distribution functions that are substantially smoother in phase space than can be obtained in models without the regularization. The stellar masses in regularized models are represented by many more orbits than in non-regularized models. For example, for the galaxy model that best reproduced the data in Pilawa et al. [135], non-regularized models had 99%, 99.9%, and 99.99% of the mass in 298, 365, and 397 of the 14040 orbits in the library, respectively; while regularized models have the same percentages of the mass represented by ∼5100, ∼6400, and ∼7200 orbits, respectively. Here we use regularization as a way to generate simulated galaxy kinematics that are represented by a wide variety of orbital weights. In the tests below, we will assess the ability of the `TriOS` code in recovering the input galaxy parameters without using regularization, as is commonly done when the Schwarzschild method is applied to real data to measure $M_{\rm BH}$ and other parameters.

Model	G_1	G_2	G_3	G_4	G_5
$M_{\rm BH}$ $[10^9 M_\odot]$	2.1	1.7	1.0	2.4	1.3
M^*/L $[M_\odot/L_\odot]$	2.23	2.31	2.43	2.25	2.28
M_{15} $[10^{11} M_\odot]$	5.5	8.9	10.2	5.5	6.0
T	0.39	0.47	0.46	0.49	0.41
$T_{\rm maj}$	0.04	0.17	0.26	0.25	0.10
$T_{\rm min}$	0.07	0.09	0.06	0.05	0.09
u	0.997	0.982	0.971	0.970	0.991
p	0.909	0.886	0.885	0.878	0.902
q	0.746	0.733	0.729	0.731	0.739

Table 3.1: Mass and shape parameters for the five triaxial galaxy models tested in this work: $M_{\rm BH}$ is the SMBH mass, M^*/L is the stellar mass-to-light ratio, M_{15} is the dark matter mass enclosed within a radius of 15 kpc, and T, $T_{\rm maj}$, and $T_{\rm min}$ are the three shape parameters specifying the triaxial potential. The axial ratios u, p, and q are related to the shape parameters and are computed here by taking luminosity-weighted averages over the MGE components (see text).

In this work, we generate simulated kinematics for five different locations in the 6D parameter space, which are labeled G_1 through G_5 and listed in Table 3.1. These parameter

values are chosen to span a broad range in each dimension, but narrow enough that the models can be explored with a reasonably sized collection of orbit models. This allows us to test the ability of the orbit code to recover model parameters over a wide range of physically reasonable values. We recall that the axis ratios (p, q, u) must obey the inequality $0 \leq q \leq uq' \leq p \leq u \leq 1$, where $q' = b'/a'$ is the observed axis ratio of the 2D projected galaxy shape (e.g., Quenneville, Liepold, and Ma [143]), and only a subspace of (p, q, u) has 3D shapes that could produce the required flattening q' upon projection. The range of allowed (p, q, u) is therefore typically quite narrow.

For each galaxy model G_i, we perform five draws of random Gaussian noise and add it to the galaxy model's noise-free projected kinematics. The amplitudes of the injected noise are chosen to resemble those inherent in real data, so the five realizations mimic repeated observations of the same galaxy and allow us to assess the uncertainties in the recovery test for each of the simulated galaxies. The different noise realizations are labeled r_1 through r_5.

In total, we have 25 sets of simulated stellar kinematics for five models of realistic galaxies. Next, we treat each of the 25 sets of kinematics as a mock observation of a galaxy, and perform recovery tests over the full 6D parameter space to search for the best-fit parameters.

3.3 Parameter Inference and Recovery Test

In this section, we present the results of the 25 recovery tests and compare the inferred model parameters against the known input parameters of each simulated galaxy to assess how well the procedure recovers the model parameters. The computational cost is substantial and is akin to performing triaxial Schwarzshild orbit modeling and parameter inference for 25 galaxies.

For each of the five realizations for a given galaxy model in Table 1, we treat the mock galaxy's projected kinematics as simulated data and perform a 6D parameter space search following the grid-free procedure we have developed for recent analyses of real data (e.g., Quenneville, Liepold, and Ma [143], Pilawa et al. [135], and Liepold, Ma, and Walsh [108]). In this procedure, a grid-free Latin hypercube scheme is used to choose sampling points in the galaxy model parameter space (about 3000 models in this work). For each sampled model, we run `TriOS` and compute a goodness-of-fit metric associated with the model predictions compared to the input kinematics. To mimic the procedure used in orbit modeling of real data, we do not use regularization in this step (see discussion in Sec 2.2). The metric, hereafter referred to as the log-likelihood, is given by

$$-2 \ln \mathcal{L}(\boldsymbol{\mu}) = \chi^2_{\mathrm{kin}}(\boldsymbol{\mu}) = \sum_{j}^{N_{\mathrm{bin}}} \sum_{i}^{N_{\mathrm{GH}}} \frac{(h_{ij}(\boldsymbol{\mu}) - h_{ij,\mathrm{input}})^2}{\Delta h^2_{ij,\mathrm{input}}}\,, \tag{3.1}$$

where h_{ij} is the i-th Gauss-Hermite moments of the stellar LOSVDs in the j-th spatial bin, Δh_{ij} is the associated measurement uncertainty, and $\boldsymbol{\mu}$ is the set of six parameters describing the galaxy's potential. For the template galaxy NGC 2693 used in this work,

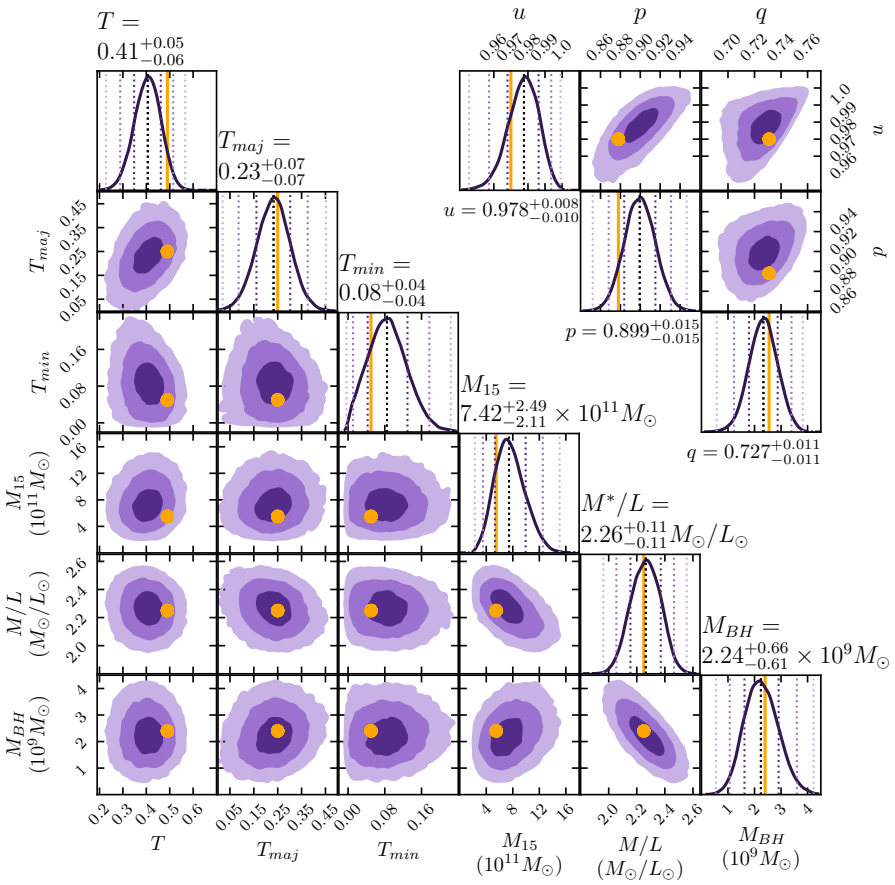

Figure 3.1: (Lower left) 1D and 2D marginalized posteriors of the six model parameters in an example recovery test (realization r_5 of model G_4). The 68%, 95%, and 99% confidence interval contours are represented by the different shades of purple in the 2D panels, and the 1D marginalized posteriors are shown in the 1D panels. The true input value for each parameter is represented by the orange filled circle and orange vertical line in each panel. (Upper right) 1D and 2D marginalized posteriors in the axis-ratio space of (p, q, u), computed from the (luminosity-weighted) posteriors of $(T, T_{\rm maj}, T_{\rm min})$.

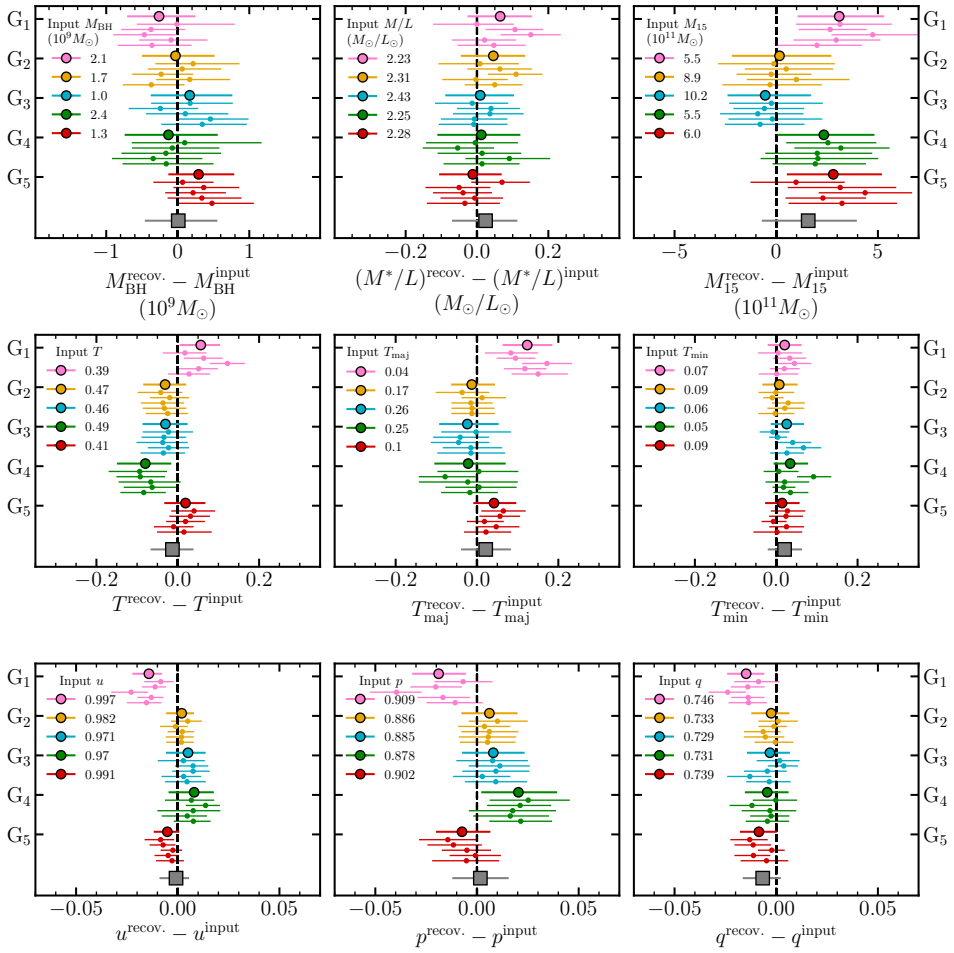

Figure 3.2: Results of the 25 rounds of recovery tests for the galaxy model parameters. The upper three panels denote the supermassive black hole mass $M_{\rm BH}$, stellar mass-to-light ratio M^*/L, and enclosed dark matter mass at 15 kpc. The middle panels show the recovered intrinsic shape parameters T, $T_{\rm maj}$, and $T_{\rm min}$, and the bottom panels show the same shape recovery but for the more intuitive luminosity-averaged axis-ratios u, p, and q. In each panel, the difference between the input parameter value (listed in the legend) and the recovered value is shown; the black dashed vertical line indicates exact recovery of that parameter. The five galaxy models G_1 through G_5 are grouped by colors. Within each color group, the small dot denotes the recovery result for one noise realization of model G_i, where the error bars represent the 68% credible region of the posterior samples (see Fig. 3.1 for an example). The larger filled circle for each G_i model is the mean recovered value for the five realizations, where the error bars denote the median uncertainty of the realizations. The large gray square at the bottom of each panel shows the mean over all 25 recovery tests, where the error bars denote the median value of the uncertainties of the 25 tests.

Gemini GMOS integral-field spectroscopy (IFS) yielded 60 spatial bins, each with 8 Gauss-Hermite moments, for the central $5'' \times 7''$ region of the galaxy, and McDonald Mitchell IFS yielded 29 bins, each with 6 moments, for the outer part of the galaxy [135]; together, the total number of kinematic constraints is $N_{\rm kin} = 654$.

Adopting the parameter inference procedure used in our prior work [143, 135, 108], we first construct an interpolated log-likelihood surface from the discrete set of evaluated models using Gaussian process regression [144] with a Matérn covariance kernel with $\nu = 3/2$. The resulting Gaussian process mean function is used as a smooth surrogate function for the true log-likelihood surface. The dynamic nested sampler `dynesty` [171] is then used to sample this smooth log-likelihood function and to produce a posterior assuming uniform priors on each parameter.

A typical outcome of our recovery tests is shown in Figure 3.1, where the 1D and 2D marginalized posteriors for the six model parameters in realization r_5 of model G_4 are plotted. The true input values of the model parameters (orange circles) are well recovered, lying within the 95% confidence interval of the best-fit model for all six parameters.

The results for all 25 recovery tests are summarized in Figure 3.2. The input parameter values are shown in the legend of each panel and in Table 3.1. Overall, these results show an excellent recovery of the input parameters for (i) individual mock realizations (small dots), (ii) when averaging over five realizations for each galaxy model G_i (big circles), and (iii) when averaging over all 25 tests (big square). In particular, the two key mass parameters – black hole mass and stellar mass-to-light ratios – are consistently recovered within the 68% confidence interval. For other parameters, while there are some variations across different realizations and galaxy models, the gray squares indicate that the *average* bias is consistent with 0 for all parameters.

In addition to recoveries of galaxy model parameters, we can also assess the ability of the `TriOS` code to recover intrinsic properties of the simulated galaxies. One such key property is the velocity anisotropy, typically parameterized by $\beta \equiv 1 - \sigma_t^2/\sigma_r^2$, where σ_r is the radial velocity dispersion, and σ_t is the tangential velocity dispersion with $\sigma_t^2 \equiv (\sigma_\theta^2 + \sigma_\phi^2)/2$. The value $\beta = 0$ indicates velocity isotropy, while a negative (positive) β indicates tangential (radial) anisotropy.

Figure 3.3 shows the velocity anisotropy of the five simulated galaxies (black dashed curve in each panel) is preferentially tangential ($\beta < 0$) near the centers of the galaxies and preferentially radial ($\beta > 0$) beyond ~ 1 kpc. The β profiles from the five lowest χ^2 models (one for each r_i) in our recovery tests are shown as a solid color band in each panel, with the band corresponding to the mean and standard deviation in β at a given radius. We include $\beta = 0$ as the dotted gray line to guide the eye. Our tests recover the simulated β profiles quite well, with the largest discrepancies near the innermost and outermost portions of the galaxy. This trend in the innermost region has been noticed in anisotropy recovery studies before, but has been attributed to a number of different factors, including the relative paucity of orbits/mass in this innermost region [22, 94].

One feature in Figure 3.2 is the tendency towards over-estimation of the dark matter mass parameter M_{15} in three of five galaxy models (G1, G4, G5) at the $\sim 1\sigma$ level. While

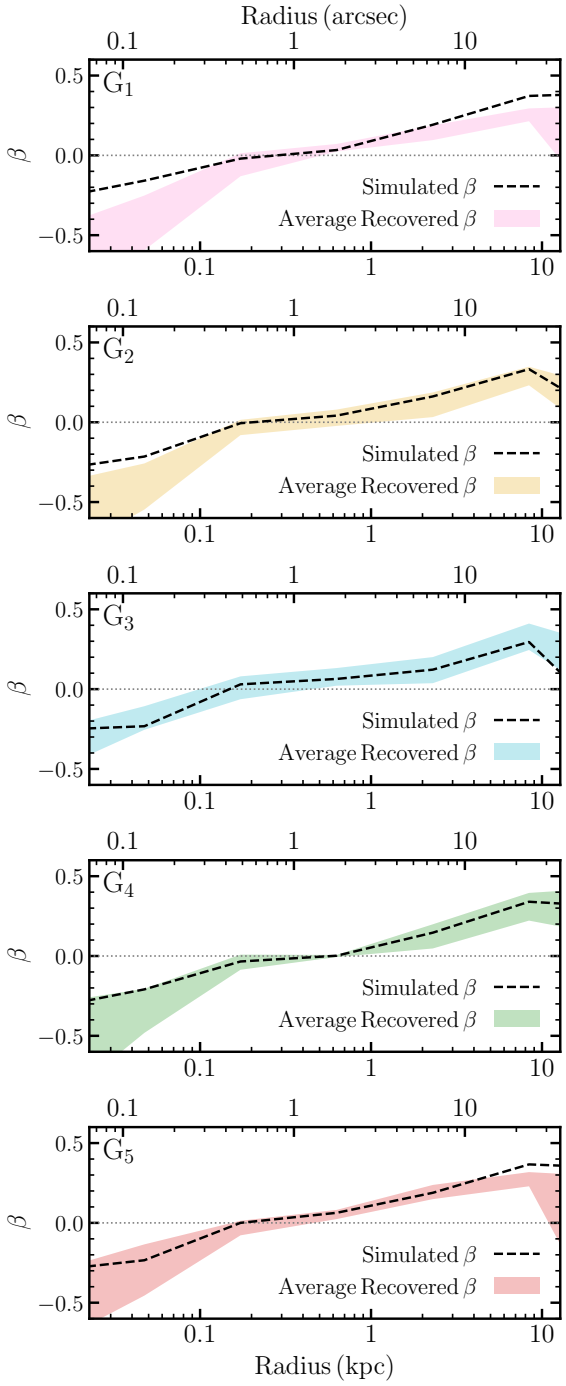

Figure 3.3: Profile of the velocity anisotropy parameter, $\beta \equiv 1 - \sigma_t^2/\sigma_r^2$, for the five simulated galaxies G_1 to G_5 (top to bottom; black dashed curves). At each radius, the colored band indicates the standard deviation of β from the recovery tests of the five realizations for the given galaxy model.

this trend could be simply due to small number statistics, there are factors that could make the halo parameter less well constrained than other parameters. In general, the constraint on the halo is driven by the outermost portion of the kinematic data since this is the region in which the enclosed dark matter mass starts to become comparable to that of the stars. Due to the rapidly decreasing surface brightness in the outer regions of galaxies, we must co-add stellar spectra over a much larger area of the sky to achieve a reasonable signal-to-noise ratio. Furthermore, our outer data were obtained from the wide-field Mitchell IFS on a 2.7-meter telescope, while the inner data were from the high-resolution GMOS on a 8.1-meter telescope. The larger uncertainties in the outermost kinematic data points thus allow for larger perturbations when we generate the simulated galaxy kinematics. In addition, our recipe for computing the simulated Gauss-Hermite moments thus far does not take into account the correlations in the *uncertainties* in the moments [78]. These factors together can potentially bias the halo parameter more than the other parameters in our model.

3.4 Model Complexity and Impact of Penalty Terms

As discussed in Sec. 1, in the framework of classical statistic modeling, increasing the complexity of a model generally results in a better goodness-of-fit statistic. If the complexity is variable across models, the apparent goodness-of-fit may be biased by the variable complexity. In this section, we examine this issue by adding a term to our log-likelihood function of Equation (4.1) in the form of

$$-2\ln\mathcal{L}(\boldsymbol{\mu}) \rightarrow -2\ln\mathcal{L}(\boldsymbol{\mu}) + \kappa(\boldsymbol{\mu})\,, \tag{3.2}$$

where κ is a "penalty" term used to capture a model's complexity. Various forms of κ have been proposed in the literature (see Sec. 1) to penalize the models in the parameter space with more complexity and alleviate any resultant biases in the inferred model parameters.

Intuitively, κ can be interpreted as serving a similar role as the Bayesian prior probability distribution. Just as the prior changes the shape of the posterior probability distribution given some previous knowledge of the parameter space, the shape of the penalty term $\kappa(\boldsymbol{\mu})$ adjusts the goodness-of-fit landscape in our study, $\chi^2_{\rm kin}(\boldsymbol{\mu})$, to correct for variability in model complexity as a function of the parameter space location $\boldsymbol{\mu}$. In regions in which the model complexity κ is high, the goodness-of-fit $\chi^2_{\rm kin}$ should tend to be lower, and the relative trade-off of these two quantities yields the final inferred locations by subtly displacing the minimum of the modified log-likelihood landscape.

Here we consider the complexity measure proposed in Ye [198] and adopted in Lipka and Thomas [109]. Those works compute a generalized DOF that is related to the ability of the model to respond to small perturbations in the model constraints. Intuitively, a model with a higher complexity (or flexibility) will be more responsive to those small perturbations, while a simple (or inflexible) model will be less responsive. In our application, the constraints are given by the observed stellar kinematic moments and the goodness of fit is described by the log-likelihood. To measure the flexibility of a given model, we perturb the stellar

kinematic predictions from that model a refit the model given those perturbed kinematics. The complexity (or flexibility) of the model is related to the amount of improvement in the log-likelihood after this re-fitting. For flexible models the improvement is large while for inflexible models the improvement is smaller. This scheme empirically connects variations in the data directly to variations in the goodness of fit on a model-by-model basis without making significant assumptions about the form of the modeling.

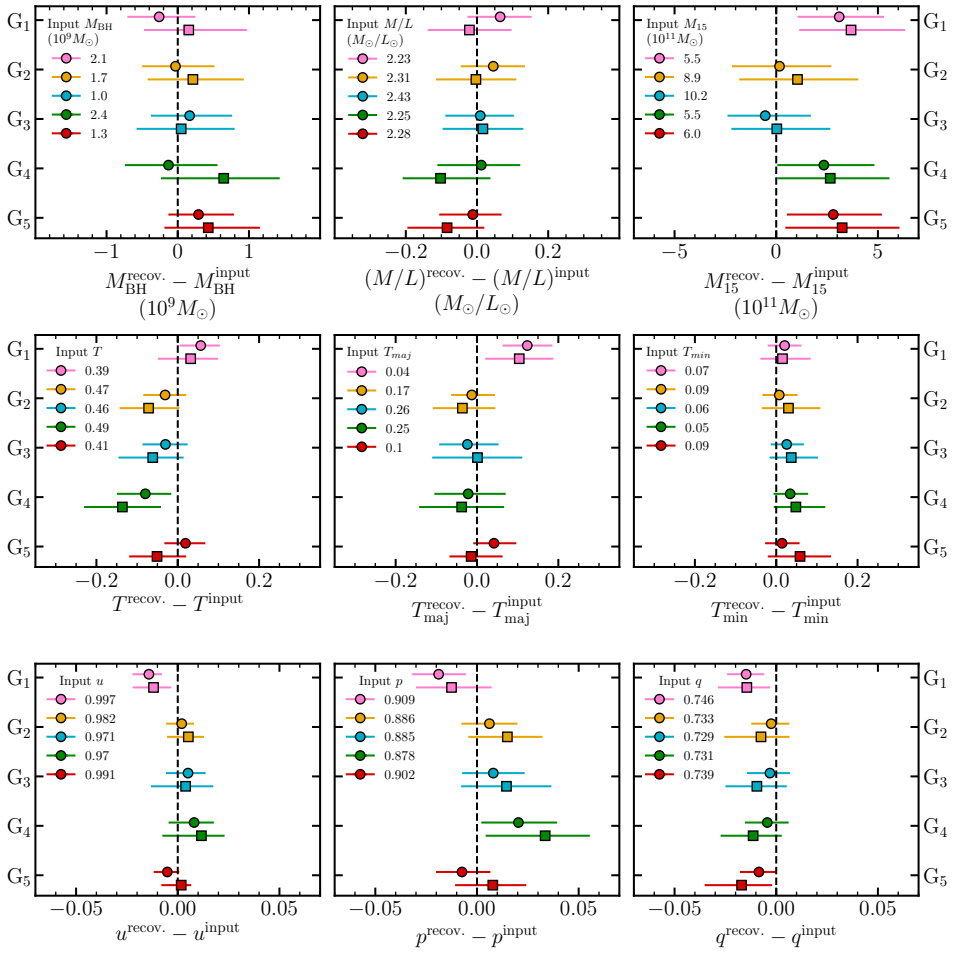

Figure 3.4: Effect of adding a penalty term to the log-likelihood function (see Equation 2) in the recovery tests. The filled circles are identical to those in Figure 2 and denote the mean difference between the recovered and true parameter values of the five noise realizations for each galaxy model G_i. The corresponding result after including a penalty term is shown as squares. A penalty term leads to no improvement in parameter recovery.

The specific steps used to compute the penalty term are as follows. We first fit a set of galaxy kinematics using a Schwarzschild model with parameters $\boldsymbol{\mu}$. We then perturb

this model's kinematic moment predictions using Gaussian-distributed random values whose amplitudes are equal to the original measurement errors. We generate 20 realizations of these perturbations. For each realization, a χ^2-like term $\chi^2_{\mathrm{prior},i}$ is computed, which describes the difference between the perturbed and unperturbed moments. This quantity only depends on the number of kinematic moments that have been perturbed, with $\langle \chi^2_{\mathrm{prior},\,i} \rangle = N_{\mathrm{kin}}$. We then re-optimize the orbital weights in the Schwarzschild model to fit these perturbed kinematics, resulting in a goodness-of-fit $\chi^2_{\mathrm{posterior},\,i}(\boldsymbol{\mu})$. The difference in these two quantities is taken to be a measure of the complexity with $\chi^2_{\mathrm{prior}} - \chi^2_{\mathrm{posterior}}(\boldsymbol{\mu}) \equiv m_{\mathrm{eff}}(\boldsymbol{\mu})$, appropriately averaged across the 20 realizations. For a given set of galaxy model parameters, this procedure is identical to generating a simulated galaxy with those parameters, then fitting the simulated data with the same set of parameters. This is repeated for each of the $\sim$3000 models in our sample of orbit models used for the analyses in previous section.

The recovered parameters for the five simulated galaxies using the original likelihood $\mathcal{L}$ (circles; same as in Fig. 3.2) versus the penalized likelihood (squares) are shown in Figure 3.4. Each symbol represents the mean value (relative to the true value) over the five noise realizations, and the uncertainty is taken to be the median uncertainty of the realizations. Overall, there are only small differences in the resulting best-fit parameters and confidence intervals, and the average recovered values and median uncertainties are all consistent with one another at the 68% confidence level. The surface of our penalty term as a function of galaxy parameters is generally quite flat and shows no consistent structure. In some cases in Figure 3.4, adding the penalty term in fact moves the recovered median value away from the true value. This first exploration of model complexity for triaxial models therefore indicates that both the mass and shape parameters of a simulated triaxial galaxy are well recovered using our likelihood function without a penalty term.

When axisymmetry is imposed in orbit models, Lipka and Thomas [109] find their penalty term to be essentially monotonically increasing with increasing galaxy inclination angle i. The source of this dependence was attributed to the orbital structures of an axisymmetric potential as follows. A fair phase-space sampling of an axisymmetric galaxy includes both a prograde and a retrograde copy of every orbit. In the edge-on axisymmetric limit, these two orbits have opposite signs in the line-of-sight velocities and can contribute maximally to the model LOSVDs. In the face-on limit, on the other hand, the velocities of these two orbits are perpendicular to the line of sight, and the prograde and retrograde orbits contribute essentially identically to the resultant LOSVD. The inclination-dependent degeneracy between the prograde and retrograde orbits yields an effectively smaller number of distinct orbits for oblique and maximally face-on inclinations than edge-on inclinations, resulting in models with edge-on inclinations having more flexibility to produce good fits to the input data.

Triaxial potentials admit a larger suite of orbital types with more complicated structures and less symmetry than axisymmetric potentials. The inclination angle for an axisymmetric galaxy is replaced by three angles, or equivalently, three shape parameters (e.g., van den Bosch et al. [183] and Quenneville, Liepold, and Ma [143]). While adding a penalty term improved the recovery of the inclination angle in axisymmetric mock models, we do not find such a term to be necessary for triaxial models.

3.5 Conclusion

We have presented a study on the accuracy and reliability of recovering known sets of input galaxy mass and shape parameters using the triaxial Schwarzschild orbit modeling code `TriOS`. We generated 25 sets of simulated galaxy kinematics and performed a full search in the 6D parameter space using our likelihood-based inference scheme to derive best-fitting parameters and confidence intervals. Treating the goodness-of-fit as proportional to a Bayesian log-likelihood, we produced posterior probability distributions for each parameter using dynamic nested sampling. The computational cost of this study is similar to that of performing full-scale triaixal Schwarzshild orbit modeling and parameter inference for 25 galaxies.

The outcome of this study indicates robust recovery of both the parameters defining the galaxy potential (Figures 3.1 and 3.2) and internal orbital structures such as the stellar velocity anisotropy profiles (Figure 3.3). In particular, the two key mass parameters in the galaxy models – black hole mass and the stellar mass-to-light ratio – are always recovered within the 68% confidence interval of the true values.

We additionally estimated the statistical model complexity of the triaxial models and tested the impact of this penalty term on the resulting parameter estimation. In contrast to recent tests of axisymmetric orbit models, we find that penalty terms quantifying the varying model-to-model complexity do not appreciably alter the shape of the likelihood landscape, nor do they significantly impact the location of the best-fitting models (Figure 3.4). At best, the posteriors obtained with the inclusion of a penalty term reproduce the posteriors obtained without a penalty term; at worst, the addition of a penalty term artificially increases the sizes of the confidence intervals, weakening the overall statistical power of the models and parameter inference scheme.

Taken together, our results suggest that triaxial Schwarzschild orbit modeling with the `TriOS` code, when combined with dense sampling of the 6D parameter space and our parameter inference scheme, can *simultaneously* recover known mass parameters (for black holes, stars, and dark matter) as well as triaxial galaxy shape parameters without the need of a penalty term to compensate for model complexities.

Acknowledgements

The authors acknowledge support from NSF AST-2206307, the Heising-Simons Foundation, and the Miller Institute for Basic Research in Science. This work used the Extreme Science and Engineering Discovery Environment (XSEDE) at the San Diego Supercomputing Center through allocation AST180041, which is supported by NSF grant ACI-1548562.

Chapter 4

A Triaxial Stellar Dynamical Measurement of the Supermassive Black Hole Mass and Intrinsic Galaxy Shape of Giant Radio Galaxy NGC 315

This chapter presents a triaxial stellar-dynamical measurement of the SMBH mass and intrinsic shape of NGC 315, a massive radio galaxy with an existing black hole mass measurement from ALMA CO gas dynamics. The analysis uses MASSIVE survey stellar kinematics and wide-field photometric information to model the galaxy with the same orbit-based framework used elsewhere in this dissertation. The motivation is twofold: to add another triaxial stellar-dynamical measurement for a massive early-type galaxy, and to provide a direct cross-check between SMBH masses inferred from stellar dynamics and molecular gas dynamics. This chapter was originally published as:

Jacob Pilawa, Emily R. Liepold, Chung-Pei Ma, Jonelle L. Walsh, and Jenny E. Greene. "The MASSIVE Survey. XX. A Triaxial Stellar Dynamical Measurement of the Supermassive Black Hole Mass and Intrinsic Galaxy Shape of Giant Radio Galaxy NGC 315". In: The Astrophysical Journal 989, 98 (Aug. 2025). doi: 10.3847/1538-4357/adee1e. arXiv: 2504.01071 [astro-ph.GA].

4.1 Introduction

The MASSIVE survey is a volume-limited, photometric and spectroscopic survey of the ∼100 most massive early-type galaxies (with stellar mass $M_* \gtrsim 10^{11.5} M_\odot$) in the local Universe [113]. A key scientific goal of the survey is to dynamically measure the masses of a sample of supermassive black holes (SMBHs) within the targeted volume (to a distance of ∼100

Mpc above declination $\delta = -6°$) with spatially resolved stellar and gas (when present) kinematics. To date, 14 MASSIVE galaxies have published dynamical SMBH mass ($M_{\rm BH}$) measurements as compiled in Table 1 of Liepold and Ma [106]. Among them, only M87 has $M_{\rm BH}$ determined from the motion of more than one type of dynamical tracers. For the rest, nine galaxies[1] have $M_{\rm BH}$ determined from stellar kinematics using the Schwarzschild orbit modeling method, three galaxies[2] have $M_{\rm BH}$ inferred from CO kinematics, and one galaxy[3] is studied with ionized gas.

In this work, we report a new mass measurement of the SMBH in NGC 315 using stellar kinematics from MASSIVE survey observations and the triaxial orbit modeling method. NGC 315 has a prior $M_{\rm BH}$ determination based on CO kinematics from Atacama Large Millimeter/submillimeter Array (ALMA) observations [19]. NGC 315 is therefore only the second galaxy in the MASSIVE survey for which a direct comparison of $M_{\rm BH}$ from different dynamical tracers can be made. Beyond MASSIVE, six other galaxies have $M_{\rm BH}$ inferred from both ALMA CO kinematics and stellar kinematics, enabling us to assess the consistency between the two methods (see Sec. 4). NGC 315 is also only the 5th MASSIVE galaxy for which the triaxial stellar orbit modeling is used to determine its $M_{\rm BH}$ (others assumed axisymmetry), and the first MASSIVE galaxy with $M_{\rm BH}$ determined from both CO and *triaxial* stellar based methods.

NGC 315 is the brightest member of a galaxy group identified in the Two Micron All Sky Survey (2MASS) group catalog [42]. The high-density contrast and low-density contrast versions of the catalog list 6 and 97 member galaxies, respectively. The halo virial mass is estimated to be $3.5{\times}10^{13} M_{\odot}$ based on member galaxy velocities. NGC 315 has strong nuclear radio emission [59] and a prominent jet extending $\gtrsim 100''$ at a position angle (PA) of $\sim -50°$ [101, 145]. NGC 315 is one of seven MASSIVE survey targets with evidence for an X-ray point source in the nuclear region in the $4-7$ keV band. The mean temperature and luminosity of the X-ray hot gas are estimated to be $T_X = 0.57$ keV and $L_X = 3.8{\times}10^{41}$ erg s^{-1} [67].

Typical of MASSIVE galaxies, NGC 315 is a slow rotator with a velocity amplitude of $\sim 30\, km\ s^{-1}$ and a spin parameter of $\lambda = 0.063$ [191, 51]. The PA of the kinematic axis (measured E of N to the receding portion) is determined to be $\mathrm{PA_{kin}} = 222°{\pm}7°$ over the $107''{\times}107''$ field of view (FOV) of the Mitchell integral-field spectrograph (IFS, Ene et al. [52]), and $\mathrm{PA_{kin}} = 218°{\pm}13°$ in the central $5''{\times}7''$ region from Gemini IFS data [53]. The $\sim 90°$ offset between the kinematic axis and the jet indicates the projection of the angular momentum vector of the stars onto the sky is at the same PA as the jet. *HST* photometry shows boxy isophotes and nearly constant ellipticity and photometric PA between a radius of $1''$ and $100''$ with luminosity-weighted values of $\epsilon = 0.27$ and $\mathrm{PA_{phot}} = 44.3°{\pm}0.2°$ (Fig. 1.2 of Goullaud et al. [68]). The kinematic misalignment angle is consistent with 0: $\Psi = 6.3°{\pm}13.3°$ [53].

[1] NGC 708, NGC 1453, NGC 1600, NGC 2693, NGC 3842, NGC 4472, NGC 4649, NGC 4889, NGC 7619
[2] NGC 315, NGC 997, NGC 1684
[3] NGC 7052

In Section 2, we discuss the IFS data from Gemini and McDonald Observatories and the stellar velocity moment measurements reported in Veale et al. [191, 188, 190], Ene et al. [52], Ene et al. [51], and Ene et al. [53]. The *HST* observations of NGC 315 [68] and surface brightness profile determination [19] are also summarized. In Section 3, we summarize the triaxial orbit modeling code TriOS [142, 143] and the parameter search strategy used to select galaxy models, followed by a discussion of the mass and shape parameters and stellar orbital structure that best match the observations. Section 4 discusses systematic uncertainties and compares $M_{\rm BH}$ determined from stellar vs. CO kinematics.

Throughout this work, we assume a luminosity distance for NGC 315 of $D_L = 68.1 \pm 2.5$ Mpc from the MASSIVE-*HST* project using the surface brightness fluctuation technique [68, 84, 17]. At NGC 315's redshift of $z = 0.0165$, the corresponding angular diameter distance is $D_A = 65.9 \pm 2.4$ Mpc, and $1''$ is 320 pc. When comparing with Boizelle et al. [19], we adjust their reported values from their assumed $D_A = 70$ Mpc to our distance.

4.2 Observations

Photometry

We adopt the characterization of the surface brightness of NGC 315 by [19] based on archival *HST* and Spitzer photometry. The *HST* Wide Field Camera 3 (WFC3) observation in the F110W filter cover a $2.1' \times 2.2'$ region centered at NGC 315 and produce a final image with $0''.08$ pixel^{-1} scale (GO-14219; Goullaud et al. [68]). Archival Spitzer InfraRed Array Camera data from channel 1 ($3.6\mu m$) provide deeper coverage of the stellar halo. The final mosaiced image covers a radial range out to $R{\sim}11'$ (about 225 kpc).

NGC 315 has a prominent circumnuclear dust disk in the central $\sim 1''$ region. [19] produce three multi-Gaussian expansion (MGE) models (A, B2, and B3) of the mosaiced image, applying a differing amount of extinction correction to the nuclear region. The central Gaussian component in B2 and B3 has a width of $\sigma' = 0''.178$ and $\sigma' = 0''.119$, respectively, comparable to the PSF ($\sim 0''.15$). As discussed in [107], the width of the central component is poorly constrained when it is comparable or below the scale of the PSF. The MGE routine sometimes assigns a central component with $\sigma' \lesssim \sigma'_{\rm PSF}$ that does not improve the fit in a meaningful way but results in an exceptionally large central 3D density after deprojection (recall $\nu \propto \Sigma/\sigma'$ where Σ is the central surface brightnes). Accordingly, the B2 and B3 MGEs have a "bump" in their luminosity densities in the central region, as shown in Figure 4.7 in the Appendix. Additional examples of this artifact can be found in [43]. [107] circumvented this problem by imposing a lower limit on σ' during the MGE fitting. Here, we adopt MGE model A, which has $\sigma' = 0''.580$ for the central component and a smooth 3D deprojected density profile without this stellar excess. In Sec. 4.1 below, we describe results from tests using model B3, the case with the most extreme central luminosity density.

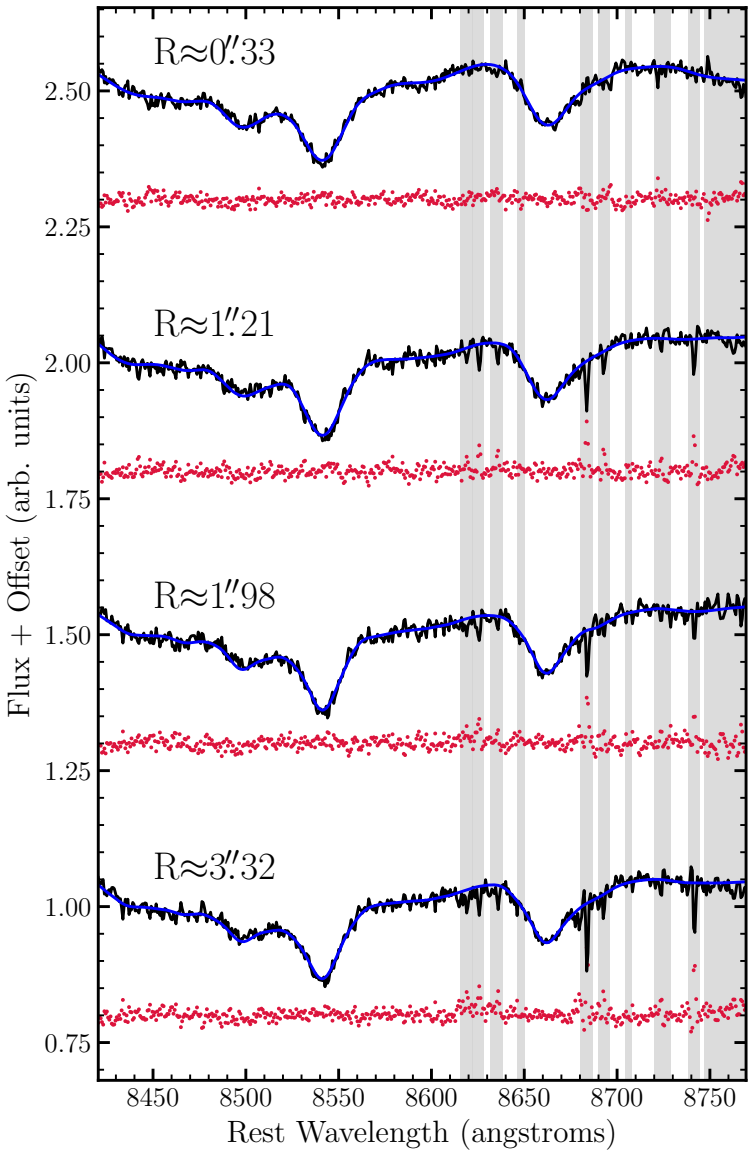

Figure 4.1: Four representative Gemini GMOS spectra (black) of NGC 315 for spatial bins located at increasing distance from the nucleus. The stellar template broadened by the best-fit LOSVD is overlaid (blue) on each spectrum. The fitting residuals (red points) are offset by constants for clarity. The typical residual is ∼0.5%. The grey shaded regions are excluded from the fit to account for improperly subtracted sky lines and detector gap.

Integral-Field Spectroscopy

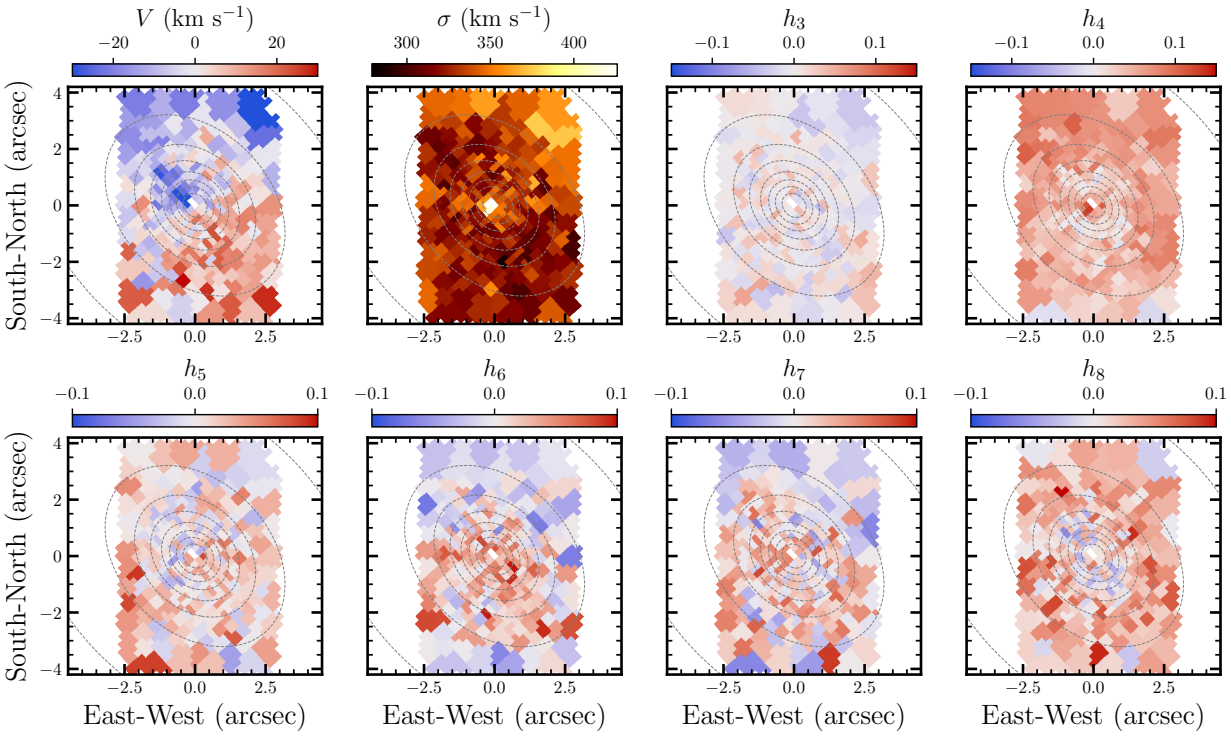

Figure 4.2: Stellar kinematic maps of the central $5'' \times 7''$ region of NGC 315 from Gemini GMOS observations. Spectra from individual lenslets are co-added to achieve a single spectrum with $S/N \gtrsim 125$ for each of the 245 spatial bins. The two upper-left panels show the line-of-sight velocities V and velocity dispersions σ, with the higher-order Gauss-Hermite moments h_3 to h_8 shown in the other panels. Surface brightness contours are plotted as dotted gray lines.

Central stellar kinematics

We observed the central $5''\times7''$ of NGC 315 using the two-slit IFS mode of Gemini Multi-Object Spectrograph (GMOS) on the Gemini North Telescope with 1000 hexagonal lenslets (each with a projected diameter of $0\farcs2$). Ten science exposures of 1200 seconds each were obtained, totaling 3.3 hours of on-source and simultaneous observations of a $5''\times3\farcs5$ region of sky offset by $\sim1'$ from the galaxy. The R400-G5305 grating with the CaT filter was used to cover the wavelength range 7800−9330 Å. The median spectral resolution (determined from arc lamp lines for each lenslet) was 2.5 Å FWHM. Details of the data processing procedure are described in MASSIVE Paper XIII [51].

We co-add the spectra from a group of adjacent GMOS lenslets to achieve a threshold signal-to-noise ratio (S/N) of 125. This binning procedure results in 248 high-quality spectra covering the central region of NGC 315. One difference in this step from Ene et al. [51] is that a symmetric binning scheme over the four quadrants of the galaxy was used in that work, while here we perform the binning over the entire GMOS FOV without this assumption. This difference only introduces minor adjustments in how the GMOS lenslets are grouped spatially; the stellar kinematics are measured for each bin without any symmetry assumption in both analyses.

From each spectrum, we measure the line-of-sight velocity distribution (LOSVD) from the CaII triplet (CaT) absorption features over a rest wavelength range of 8420−8770 Å using the penalized pixel-fitting (pPXF) method [32]. The LOSVD is represented as a Gauss-Hermite series of order $n = 8$. We use 15 stellar templates from the MILES CaT Library that covers a wavelength range of 8437−9020 Å with a spectral resolution of 1.5 Å FWHM [36]. This set of stars is taken from Table 2 of [5], but we find consistent stellar kinematics when the full library of 706 stars is used. A multiplicative polynomial of degree three is used to model the stellar continuum in each spectrum.

Four representative spectra at increasing radii are plotted in Figure 4.1. The template spectrum broadened by the best-fit LOSVD (blue curve) provides an excellent fit to each observed spectrum (black curve) with a typical residual (red points) of ∼0.5%. In addition to the bright sky lines, the wavelength range $\gtrsim$8750 Å is also masked due to the presence of a gap in the CCD chip. The resulting maps of the eight Gauss-Hermite moments of the LOSVDs for the 248 GMOS spatial bins are shown in Figure 4.2. The corresponding radial profiles of the eight moments are displayed as blue bars in Figure 4.3. The errors on the moments are determined via the Monte Carlo method described in Section 4 of [51]. These figures show a velocity profile with a low amplitude rotational velocity $|V|\sim$20 $km\ s^{-1}$, and a velocity dispersion profile that rises from $\sigma\sim$320 $km\ s^{-1}$ at $R\sim2''$ inward to $\sigma\sim$350 $km\ s^{-1}$ at $R\sim0''.3$.

Wide-field stellar kinematics

We observed NGC 315 with the Mitchell IFS at the McDonald Observatory as part of the MASSIVE Survey. Details of the observation, data reduction and kinematic measurements are described in [191, 188, 190]. The observations consisted of three dither positions, during which we interleaved two 20 minute science frames with one 10 minute sky frame, resulting in 2 hours on-source. Each frame spans a $107''\times107''$ FOV with 246 fibers, covering a wavelength range of 3650−5850 Å that includes the Ca HK region, the G-band region, $H\beta$, Mgb, and several Fe lines. The individual fibers in the central region of NGC 315 provide spectra with $S/N \gtrsim 50$. For the fainter part of the galaxy covered by the outer fibers, the spectra are co-added to achieve $S/N \gtrsim 20$.

The LOSVD from each Mitchell spectrum is extracted in a similar way as GMOS described above. We opt to fit to $n = 6$ Gauss-Hermite moments due to the lower S/N data here. The MILES library of 985 stellar spectra is used as templates [152, 58]. The kinematic

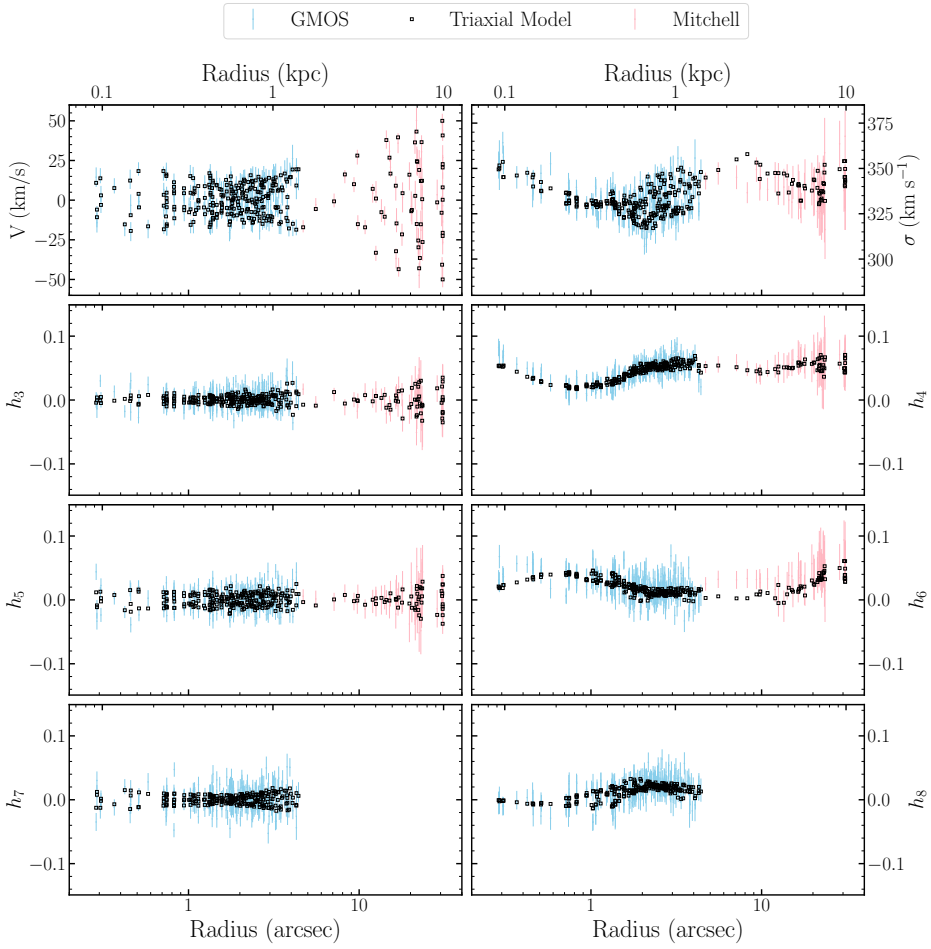

Figure 4.3: Radial profiles of the stellar kinematic moments for NGC 315 from Gemini GMOS (blue bars) and Mitchell (pink bars) data. Moments predicted by the best-fitting triaxial galaxy model (black squares) listed in Table 1 match the input data well.

moments for the 55 Mitchell bins are shown in Figure 4.3 in pink. The Mitchell data points connect smoothly to the GMOS points, showing excellent agreement between measurements obtained from different spectrographs, telescopes, and spectral regions. Six additional kinematic points at $R{\sim}50''$ are shown in Figure D1 of Veale et al. [191] but are excluded in the following analysis due to the low S/N of these outer spectra.

4.3 Results from Triaxial Orbit Modeling

The TriOS Code and Galaxy Models

We use the *TriOS* code [183, 142, 143] to compute triaxial orbit models of NGC 315. This code integrates a large number of stellar orbits that span the allowed phase space and computes the LOSVDs for a wide range of galaxy model parameters. The galaxy is assumed to have three mass components: a central black hole of mass $M_{\rm BH}$, a stellar component with a mass-to-light ratio M^*/L, and a dark matter halo with a density profile $\rho(r) = \rho_0/[(r/r_s)^\gamma\,(1+r/r_s)^{3-\gamma}]$, where r_s is a scale radius [126]. We set $\gamma = 0$ so that the profile has a finite central density ρ_0 and a flattened central density distribution similar to that of the stars. With our data, r_s and ρ_0 are often quite degenerate so we choose to parameterize the halo with a single parameter, M_{15}, defined to be the dark matter mass enclosed within 15 kpc with a fixed scale radius $r_s = 15$ kpc. A similar strategy was used in orbit modeling of other MASSIVE galaxies (e.g., Liepold et al. [105], Quenneville, Liepold, and Ma [143], and Pilawa et al. [135]).

We use three parameters to specify the triaxial shape of the stellar component: $p = b/a$ is the intrinsic middle-to-long axis ratio, $q = c/a$ is the intrinsic short-to-long axis ratio, and u is the apparent-to-intrinsic long axis ratio. These three shape parameters are related to the three angles θ, ϕ, and ψ that relate the intrinsic and projected coordinate systems of NGC 315; see Equations (4) and (8) of Quenneville, Liepold, and Ma [143]. Here θ and ϕ are polar angles in NGC 315's intrinsic coordinate system, and ψ specifies the remaining degree of freedom – a rotation of the galaxy around the line of sight.

In total, each galaxy model has 6 free parameters – $M_{\rm BH}$, M^*/L, M_{15}, and three shape parameters – to be constrained by the kinematic and photometric data. For each model, we use the same procedures for phase space sampling and orbit integrations as in our earlier work (e.g., Section 4.1 of Liepold, Ma, and Walsh [108]). We integrate the trajectories of stars to build a library of 437,400 stellar orbits. A dithering factor of $N_{\rm dither} = 3$ is used, where the properties of $N_{\rm dither}^3 = 27$ orbits with similar initial conditions are averaged, effectively giving them a single shared orbital weight. We determine the resulting 16,200 independent orbital weights using the kinematic measurements with non-negative least squares [102], under the additional constraint that both the projected mass within each aperture and the 3D mass distribution in coarse bins are consistent within 1% of the MGE. The GMOS and Mitchell PSFs are taken to be single, circularly symmetric Gaussians with FWHM of $0\farcs38$ and $1\farcs2$, respectively.

Best-Fit Triaxial Model

We use the model selection scheme described in our recent work (e.g., Pilawa et al. [135] and Liepold, Ma, and Walsh [108, 107]) to determine the mass and shape parameters that best match the kinematic and photometric data of NGC 315. This scheme, in brief, involves generating candidate galaxy models with Latin hypercube sampling [121], approximating the

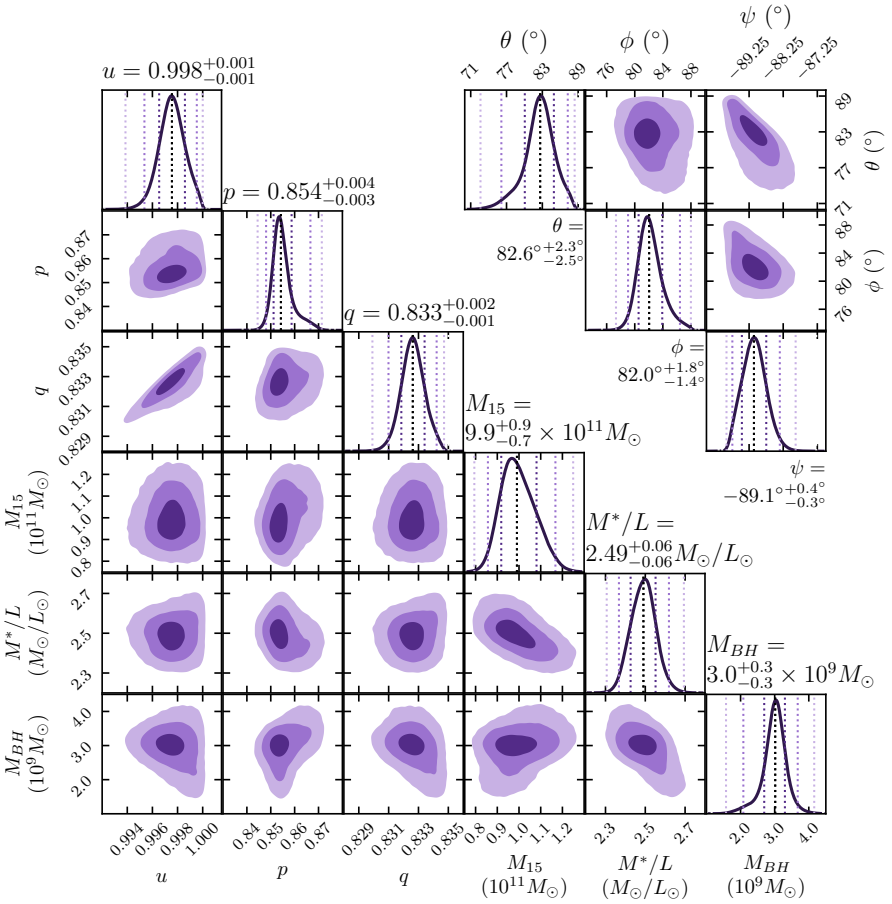

Figure 4.4: (Left) Posterior distributions of six parameters in triaxial orbit modeling of NGC 315: SMBH mass $M_{\rm BH}$, stellar mass-to-light ratio M^*/L, dark matter enclosed within 15 kpc M_{15}, and luminosity averaged axis ratios u, p, and q. The 68%, 95%, and 99.7% credible regions are represented by different shades of purple. The vertical lines in each 1D marginalized distribution indicate the median and the three corresponding confidence levels. (Upper right) Posterior distributions in viewing angle space, where θ and ϕ are polar angles in the galaxy's frame, and ψ specifies a rotation of the galaxy around the line of sight (Section 2.2 of Quenneville, Liepold, and Ma [143]).

resulting likelihood landscapes with Gaussian process regression, and sampling posteriors on our parameters via dynamic nested sampling [171]. The relative likelihood for each model is computed from

$$-2 \ln \mathcal{L}(\boldsymbol{\mu}) = \chi^2_{\rm kin}(\boldsymbol{\mu}) = \sum_j^{N_{\rm bin}} \sum_i^{N_{\rm GH}} \frac{(h_{ij}(\boldsymbol{\mu}) - h_{ij,\rm data})^2}{\Delta h^2_{ij,\rm data}}, \tag{4.1}$$

Table 4.1

Galaxy Parameters of NGC 315 from Triaxial Orbit Modeling

Galaxy Property (units)	Inferred Value
Black hole mass $M_{\rm BH}$ ($10^9 M_\odot$)	3.0±0.3
M^*/L ($M_\odot/L_\odot$)	2.49±0.06
Total stellar mass ($10^{12} M_\odot$)	1.5
DM mass within 15 kpc M_{15} ($10^{11} M_\odot$)	$9.9^{+0.9}_{-0.7}$
Triaxiality parameter T	0.89±0.02
Shape parameter $T_{\rm maj}$	$0.019^{+0.008}_{-0.007}$
Shape parameter $T_{\rm min}$	$0.017^{+0.009}_{-0.013}$
Average middle-to-long axis ratio p	$0.854^{+0.004}_{-0.003}$
Average short-to-long axis ratio q	$0.833^{+0.002}_{-0.001}$
Average apparent-to-intrinsic long axis ratio u	0.998±0.001
Line-of-sight direction $\theta(^\circ)$, $\phi(^\circ)$	$82.6^{+2.3}_{-2.5}$, $82.0^{+1.8}_{-1.4}$
Rotation about line of sight $\psi\,(^\circ)$	$-89.1^{+0.4}_{-0.3}$

Table 4.1: For each parameter, we marginalize over the other parameters and report the 68% credible regions. In orbit models, θ is the inclination angle in the oblate axisymmetric limit ($\psi = 90^\circ$, or equivalently $p = 1$), with $\theta = 90^\circ$ being edge-on and $\theta = 0^\circ$ being face-on.

where h_{ij} is the i-th Gauss-Hermite moment of the stellar LOSVDs in the j-th spatial bin, Δh_{ij} is the measurement uncertainty, and $\boldsymbol{\mu}$ is the set of six parameters describing the galaxy's potential. To obtain 1D confidence intervals for each galaxy parameter, we take the marginalized distribution for each parameter to be the distribution of (weighted) sample points over the desired parameters, assuming uncertainties in the distribution function (e.g., orbital weights) are neglected.

About ∼1750 galaxy models are used to obtain the final posteriors on the six parameters shown in Figure 4.4. An additional ∼3000 models covering wider ranges of parameters are used in the initial exploration of the 6D likelihood surface, and ∼10000 more models are used in various tests to ensure that the surface in the low χ^2 region is mapped out accurately.

A summary of the best-fit parameters for NGC 315 is listed in Table 4.1. The kinematic moments predicted by the model are compared with observed values in Figure 4.3. The total χ^2 is 1611.4 spread over 2314 kinematic constraints (8 moments for 248 GMOS bins and 6 moments for 55 Mitchell bins). A naive estimate of the reduced χ^2 would be $1611.4/(2314-6) = 0.698$ assuming 6 degrees of freedom (DOF). But we caution that DOF is nontrivial to estimate for nonlinear problems such as here. In a study using simulated stellar kinematics that mimic data in the MASSIVE survey [134], we have investigated a "generalized" measure of DOF in the form of a penalty term added to the likelihood measure [198, 110] and found it to be ~ 200 instead of the canonical value of 6, thereby raising the reduced χ^2 by ∼40%

in that study. While a similar calculation would have to be performed to estimate this alternative DOF measure for NGC 315, we expect the reduced χ^2 to be raised as well. Using this generalized measure to estimate the effective DOF in the models also helps address a related concern that the conventional (unpenalized) likelihood method does not marginalize over the high dimensional space of possible orbital weights, leading to reliable $M_{\rm BH}$ but with "overly pessimistic error estimates" [114]. In Pilawa, Liepold, and Ma [134], we find that the parameter search and inference routines used in this paper and other work by our group (e.g., Quenneville, Liepold, and Ma [143], Pilawa et al. [135], Liepold, Ma, and Walsh [108], Pilawa, Liepold, and Ma [134], and Liepold, Ma, and Walsh [107]) are able to reliably recover the mass and shape parameters associated with synthetic galaxy kinematic data without any additional penalty terms.

A handful model predictions in Figure 4.3 lie outside the 68% uncertainties of the data points, e.g., the h_4 and h_6 GMOS moments within $0\farcs6$ are under-predicted (on average) by $\sim$1.05σ and $\sim$1.11σ, respectively, and Mitchell's velocity dispersion and h_6 between $5''$ and $10''$ are over- and under-predicted by $\sim$1.1σ and $\sim$1.6σ, respectively. These systematic local deviations occur in $\lesssim 2\%$ of the 2314 kinematic constraints. When excluding these deviant constraints from the χ^2 used for our parameter inference, we find an insignificant change in the inferred $M_{\rm BH}$.

Black Hole Mass, Stellar Mass, and Dark Matter Mass

To assess how NGC 315 and its SMBH fit in the population of local galaxies with dynamically inferred $M_{\rm BH}$, we examine its location on the well-studied $M_{\rm BH}-\sigma$ and $M_{\rm BH}-M_{\rm bulge}$ relations. NGC 315's luminosity-weighted velocity dispersion within R_e is found to be $\sigma_e = 341$ km s^{-1} based on the same Mitchell IFS data in this paper [191]. At this σ_e, the mean full-sample $M_{\rm BH}-\sigma$ relations of McConnell and Ma [118] and [151] predict $M_{\rm BH} = 4.2 \times 10^9 M_\odot$ and $3.3 \times 10^9 M_\odot$, respectively, 40% (0.15 dex) and 10% (0.04 dex) larger than our dynamically measured $M_{\rm BH}$. However, our $M_{\rm BH}$ is within the intrinsic scatter of both relations, 0.38 dex.

To place NGC 315 on the $M_{\rm BH}-M_{\rm bulge}$ relation, we use the total stellar mass from our best-fitting triaxial model, $M_* = 1.5 \times 10^{12} M_\odot$. At this bulge mass, the mean full-sample relations of [118] and [151] predict $M_{\rm BH} = 5.3 \times 10^9 M_\odot$ and $4.4 \times 10^9 M_\odot$, respectively, 77% (0.25 dex) and 47% (0.17 dex) larger than our measured $M_{\rm BH}$. But again, our dynamical $M_{\rm BH}$ is within the intrinsic scatter of both $M_{\rm BH}-M_{\rm bulge}$ relations, 0.34 dex.

In our preferred model, the black hole has a gravitational sphere of influence (SOI) of $r_{\rm SOI} = 0\farcs81 = 0.26$ kpc with the definition of $M^*(< r_{\rm SOI}) = M_{\rm BH}$, and $r_{\rm SOI} = 1\farcs1 = 0.35$ kpc with the definition of $M^*(< r_{\rm SOI}) = 2M_{\rm BH}$.

Within the effective radius $R_e = 25\farcs7$ ($\sim$8.3 kpc) of NGC 315 [139], the dark matter halo constitutes $\sim$47% of the total mass of the galaxy. This value is broadly consistent with the rising dark matter fraction with increasing galaxy stellar mass reported for lower-mass early-type galaxies (e.g., Fig. 10 of Cappellari et al. [29]; Fig. 16 of Santucci et al. [153]), where the dark matter fraction (at $1\,R_e$) reaches $\sim$40% at the highest masses ($M^\star \sim 5 \times 10^{11} M_\odot$) in their samples.

Intrinsic 3D Galaxy Shape

The preferred axis ratios of $p = 0.854$ and $q = 0.833$ yield a triaxiality parameter of $T = (1 - p^2) / (1 - q^2) = 0.89 \pm 0.02$, where the limits of $T = 0$ and 1 correspond to oblate axisymmetry and prolate axisymmetry, respectively. In comparison, five other massive elliptical galaxies for which we have performed triaxial orbit modeling thus far all have smaller T. Four of them are oblate ($T \lesssim 0.5$): $T = 0.33 \pm 0.06$ for NGC 1453 [142], $T = 0.39 \pm 0.04$ for NGC 2693 [135], $T = 0.35 \pm 0.03$ for Holmberg 15A [107], and $T = 0.31 \pm 0.05$ for NGC 57 (Pilawa et al. 2025, in prep). M87, on the other hand, is slightly prolate with $T = 0.65 \pm 0.02$ [108].

While the determinations of the intrinsic axis ratios p and q for individual galaxies require triaxial orbit modeling and detailed kinematic data, one can infer the distributions of p and q *statistically* from the observed isophotal shapes and kinematic vs. photometric misalignment angles of an ensemble of galaxies. For slow-rotating galaxies in the MASSIVE survey, the mean values are found to be $\langle p \rangle = 0.88$, $\langle q \rangle = 0.65$, and $\langle T \rangle = 0.39$ [52], similar to the majority of our directly measured T thus far. Comparable distributions are also found for early-type galaxies in the ATLAS^{3D} and SAMI surveys [196, 62] and for simulated massive slow rotators in the IllustrisTNG simulations [138]. We therefore expect stellar halos with the prolateness of NGC 315 to be a rare occurrence.

Stellar Orbital Structure

The composition of the major types of orbits in the best-fit model for NGC 315 is plotted as a function of radius in the upper panel of Figure 4.5. The two types of tube orbits have a fixed sense of rotation, with short- and long-axis tubes having angular momentum components along the intrinsic short- and long-axis, respectively, which do not change sign. For the box orbits, all three components of the angular momentum change sign, leaving no sense of rotation for this orbit type. The relative contribution of these three orbit types determines the velocity structure of the galaxy.

Figure 4.5 shows that $45\% - 60\%$ of the mass in the orbits are from long-axis tubes, while short-axis tubes and box orbits contribute comparable amounts to the remaining orbital weight. The predominance of long-axis tubes over short-axis tubes reflects the prolateness of NGC 315. This is opposite to the orbital compositions in oblate triaxial galaxies with $T < 0.5$, e.g., about $60-70\%$ of orbits are short-axis tubes while $\sim$20% are long-axis tubes in NGC 1453 and NGC 2693 [142, 135].

Further insight into the relative short- and long-axis tube orbits can be gained from the relationship between the parameter T and the locations in the start space from which the tube orbits are generated (using the scheme of Schwarzschild [159]). Quenneville, Liepold, and Ma [142] shows that the location of the focal curve demarcating the regions in start space populated by long- and short- axis tubes (their Fig. 1) is specified by an angle η, where $\tan \eta \approx \sqrt{T/(1-T)}$. For $T = 0.89$, we have $\eta \approx 71^\circ$, indicating the long- and short-axis tube fraction in the start space is 79% and 21%, respectively, corresponding to

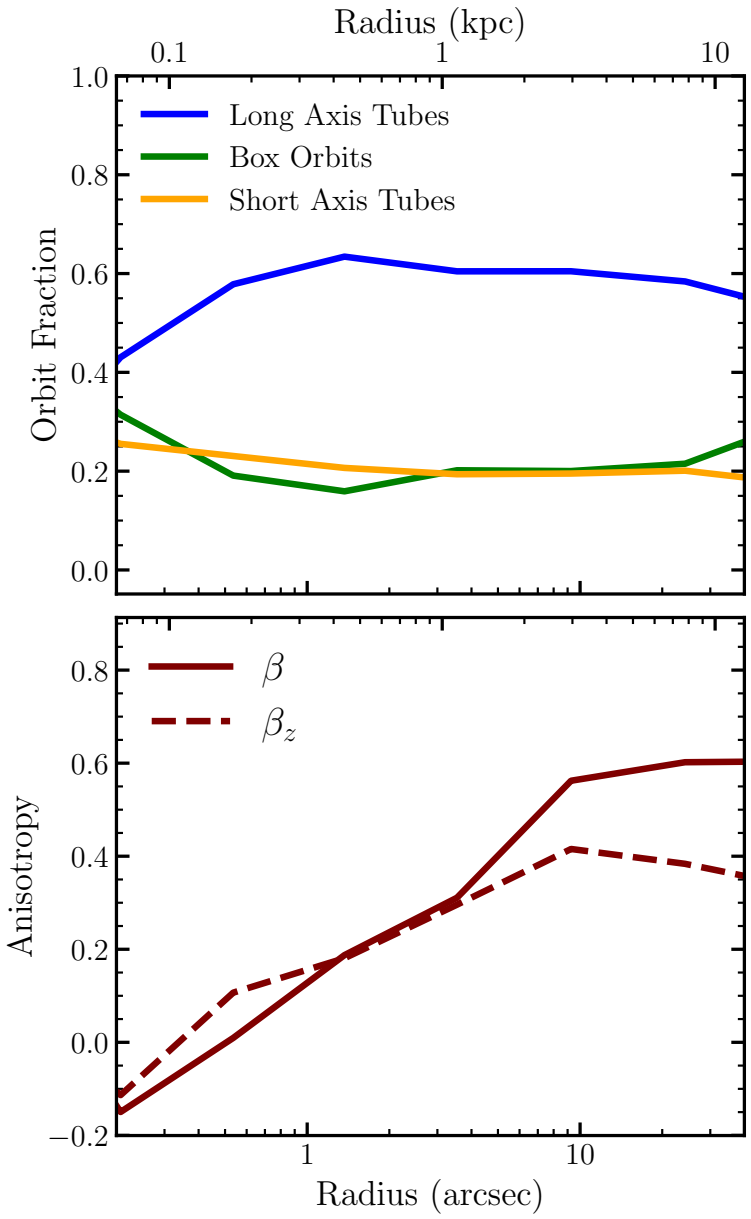

Figure 4.5: Composition of the three major orbit types (upper panel) and velocity anisotropy (lower panel) as a function of radius in the best-fit triaxial galaxy model of NGC 315. The majority of the orbital weights are in long-axis tube orbits, consistent with the prolateness of the galaxy. Short-axis tube orbits and box orbits both contribute about $20\% - 25\%$ to the remaining orbital weights.

The velocity anisotropy parameters $\beta \equiv 1 - \sigma_t^2/\sigma_r^2$ (in spherical coordinates) and $\beta_z = 1 - \sigma_z^2/\sigma_R^2$ (in cylindrical coordinates) indicate the stellar orbits are mildly tangentially anisotropic at small radii and are increasingly radially anisotropic at larger radii.

a ratio of about 4 to 1. The actual orbital fractions for the best-fit galaxy model shown in Figure 4.5 are computed from these base orbits with the corresponding orbital weights, yielding a comparable long-to-short tube ratio of roughly 3 to 1.[4]

The lower panel of Figure 4.5 displays the radial profile of the velocity anisotropy parameters, $\beta = 1 - \sigma_t^2/\sigma_r^2$ and $\beta_z = 1 - \sigma_z^2/\sigma_R^2$, where σ_t and σ_r are the tangential and radial velocity dispersions in spherical coordinates, and σ_z and σ_R are the vertical and radial velocity dispersions in cylindrical coordinates, respectively. The orbits in the central portion of NGC 315 are slightly tangential with $\beta < 0$ and become radially anisotropic away from the center. This trend is typical in massive elliptical galaxies (e.g., Thomas et al. [177]) and can be seen in other MASSIVE galaxies (e.g., Liepold et al. [105] and Pilawa et al. [135]).

4.4 Discussion

Uncertainties in Central Surface Brightness

A primary systematic uncertainty in the mass measurements of NGC 315 SMBH is the effect of dust on the observed central stellar light. In the main analysis above, we have used MGE model A of Boizelle et al. [19] to approximate the surface brightness profile of NGC 315. To test the impact of the adopted profile on the inferred $M_{\rm BH}$, we replace it with their MGE B3, the model that assumes the largest extinction correction. We re-run orbit models and parameter search in the reduced 3D space of $M_{\rm BH}$, M^*/L, and halo mass with the shape parameters fixed to the best-fitting values. While model B3 has a significantly higher central luminosity density than model A (Figure 4.7), the difference is confined to the inner $\sim 0\farcs5$, a scale comparable to the PSF of our Gemini observations. It is thus not surprising that our tests find $\lesssim 3\%$ changes in the best-fitting parameters, with $M_{\rm BH} = (2.9 \pm 0.2) \times 10^9 M_\odot$ and $M^*/L = 2.45 \pm 0.04\, M_\odot/L_\odot$. In comparison, Boizelle et al. [19] find that switching from model A to B3 in their CO-based study reduces $M_{\rm BH}$ and M^*/L by $\sim 18\%$. One possible reason for this larger change in their tests is the CO kinematic data only extend to $\sim 1''$, and thus their constraints are more sensitive to changes in the central luminosity density and the enclosed mass.

$M_{\rm BH}$ from Stellar vs. CO Kinematics

With the mass measurement of NGC 315's SMBH presented in this paper, there are now seven galaxies whose SMBH masses have been determined from the kinematics of both CO and stars (with orbit-based modeling). A summary of these measurements is given in Table 4.2 and Figure 4.6. To assess the level of agreement between $M_{\rm BH}$ from the two

[4]The preferred viewing angles (in Table 4.1) are close to the intermediate axis ($\theta = \phi = 90°$). In this limit, the freedom for the deprojection extends roughly along the intermediate axis, corresponding to different values of T (see Equations (7) and (8) of Quenneville, Liepold, and Ma [143]). Within the viewing-angle parameterization of the deprojection, the third viewing angle ψ then sets T.

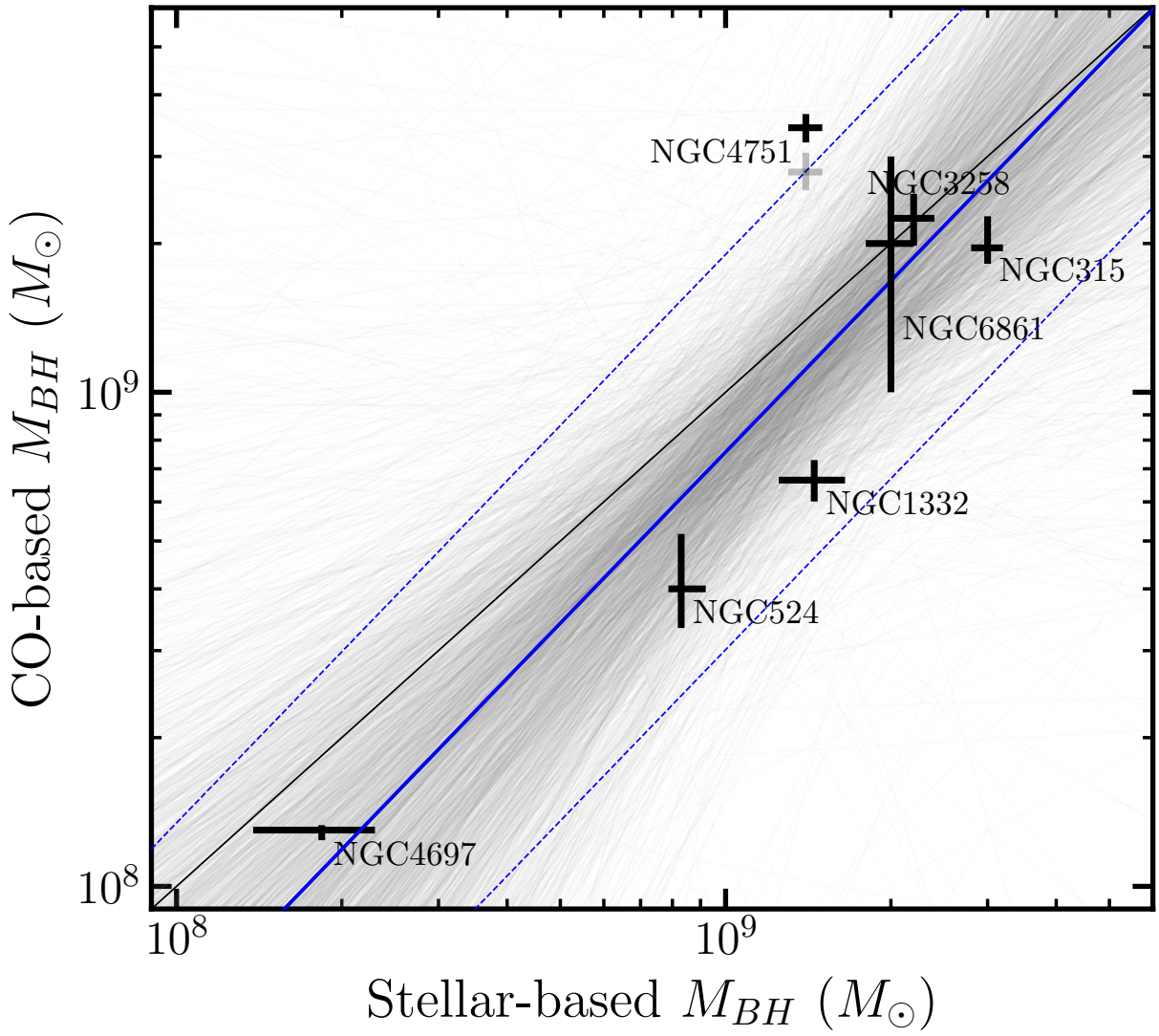

Figure 4.6: Comparison of seven local galaxies with $M_{\rm BH}$ determined independently from stellar and CO kinematics listed in Table 2. The median linear fit (solid blue line) is given by $\log_{10}(M_{\rm BH}^{\rm CO}/10^9 M_\odot) = (1.15^{+0.44}_{-0.41}) \log_{10}(M_{\rm BH}^{\rm stellar}/10^9 M_\odot) - (0.12 \pm 0.15)$, with an intrinsic scatter of $\epsilon = 0.35^{+0.26}_{-0.12}$ dex (dotted blue lines). Faint gray lines are constructed from sampling over the posteriors for our parameters. The solid black line denotes the one-to-one line to guide the eye. The two points for NGC 4751 represent $M_{\rm BH}$ inferred when assuming a spatially varying (lower point) vs. constant (upper point) M^*/L in the CO-based model (see text).

methods, we perform a linear fit using the `LinMix` package [89]. This method derives the best-fitting line through hierarchical Bayesian modeling, accounting for uncertainties in both x and y directions. It models the distribution of the independent variable as a mixture of Gaussians and assumes the dependent variable is drawn from a Gaussian distribution centered on a linear relation with the independent variable. The code returns posterior distributions for the parameters, including an intrinsic scatter term representing the variance beyond measurement uncertainties.

The resulting linear fit for $M_{\rm BH}$ from the two methods is

$$\log_{10}\left(\frac{M_{\rm BH}^{\rm CO}}{10^9\,M_\odot}\right) = \left(1.15^{+0.44}_{-0.41}\right)\log_{10}\left(\frac{M_{\rm BH}^{\rm stellar}}{10^9\,M_\odot}\right) - (0.12\pm0.15), \tag{4.2}$$

with an intrinsic scatter of $\epsilon = 0.35^{+0.26}_{-0.12}$ dex (blue lines in Figure 4.6). To assess whether the data prefer a one-to-one model with a fixed slope of 1 and intercept of 0 or a linear relation with free coefficients, we compare the marginal evidence ratio ("Bayes factor") of the two models. The one-to-one model here is a subset of the free linear model, so the Bayes factor in this case quantifies the factor by which a free slope and intercept improves the fit. Using `dynesty`, we find a log-marginal evidence difference of $\Delta \ln Z = 2.78\pm0.02$ (one-to-one model minus free model), which is much less than what is typically considered evidence in favor of one model (e.g., $|\Delta \ln Z| > 5$, Trotta [179] and Lockhart and Gralla [111]). We therefore conclude that while there are differences in individual $M_{\rm BH}$ values determined from CO and stellar kinematics, there is no evidence for statistically significant biases between the two methods in the current data.

4.5 Summary

We have performed triaxial stellar orbit modeling of the massive elliptical galaxy NGC 315 using photometric data and ∼2300 spatially resolved stellar kinematic measurements in 304 bins covering a radial range of ∼0.3″ to 30″ from the MASSIVE survey as constraints. After searching over ∼15,000 galaxy models with an efficient Bayesian scheme, we are able to simultaneously constrain NGC 315's $M_{\rm BH}$, M^*/L, dark matter halo mass, and intrinsic shape parameters.

We find NGC 315 to be a triaxial and highly prolate galaxy with a triaxiality parameter $T = 0.89\pm0.02$, hosting a SMBH with $M_{\rm BH} = (3.0\pm0.3)\times10^9 M_\odot$. At this dynamically inferred mass, the NGC 315 SMBH is located below the mean $M_{\rm BH}-\sigma$ and $M_{\rm BH}-M_{\rm bulge}$ scaling relations formed by other local SMBHs and their host galaxies, but it lies within the intrinsic scatter of these relations. In comparison, the SMBH mass inferred from CO kinematics is $M_{\rm BH} = (1.96^{+0.30}_{-0.13})\times10^9 M_\odot$ (scaled to our distance).

The orbit-based $M_{\rm BH}$ determination reported in this paper adds a measurement to a small but growing sample of galaxies for which the mass of the central SMBH has been measured using more than one dynamical tracers. Comparing $M_{\rm BH}$ values for a sample of seven galaxies with both CO-based and stellar-orbit based measurements, we find that the

Table 4.2
Galaxies with dynamical $M_{\rm BH}$ measurements from both stellar and CO kinematics

		Stellar-Based Measurements			CO-Based Measurements			
Name	D (Mpc)	$M_{\rm BH}$ ($10^9\,M_\odot$)	M^*/L [band]	i	$M_{\rm BH}$ ($10^9\,M_\odot$)	M^*/L [band]	i	Ref.
(1)	(2)	(3)	(4)	(5)	(6)	(7)	(8)	(9)
NGC 315	65.9	3.0±0.2	2.49±0.06 [J]	N/A	$1.96^{+0.30}_{-0.13}$	1.86±0.01 [J]	74.1°±0.1°	(a,b)
NGC 524†	23.3	$0.83^{+0.09}_{-0.04}$	5.8±0.4 [I]	20°	$0.40^{+0.12}_{-0.07}$	5.7±0.3 [I]	20° (fixed)	(c,d)
NGC 1332	22.3	1.45±0.2	7.08±0.39 [R]	90°	$0.664^{+0.065}_{-0.063}$	7.83 [R]	85.2°	(e,f)
NGC 3258	31.9	2.2±0.2	2.5±0.1 [H]	48°	2.249±0.27	··· [H]	27.5°−49.3°	(g,h)
NGC 4697	11.4	0.18±0.05	4.3±0.3 [V]	90°	$0.13^{+0.003}_{-0.006}$	$2.14^{+0.04}_{-0.05}$ [i]	$76.1^{\circ+0.5^\circ}_{-0.4^\circ}$	(i,j)
NGC 4751	26.9	1.4±0.1	$12.2^{+0.6}_{-0.7}$ [R]	90°	$3.43^{+0.16}_{-0.16}$	2.68±0.11 [H]	$78.7^{\circ+0.1^\circ}_{-0.1^\circ}$	(k,l)
NGC 6861	27.3	2.0±0.2	$6.1^{+0.2}_{-0.1}$ [I]	90°	1−3	2.14−2.52 [H]	72.7°−73.6°	(k,m)

Table 4.2: Column 1: galaxy name. Column 2: distance. Different values are assumed in the CO vs. stellar studies for NGC 315 (this paper) and NGC 4697; the surface brightness fluctuation distance is adopted here and all measurements are scaled to this value. Column 3: black hole mass from stellar-based measurements. Column 4: stellar mass-to-light ratio for the stellar-based measurements (band indicated in square brackets). Column 5: inclination angle assumed in axisymmetric orbit modeling; only NGC 315 is modeled with a triaxial orbit code, whereas the other galaxies have a fixed inclincation. Column 6: black hole mass from CO-based measurements. Column 7: stellar mass-to-light ratio for the CO-based measurements (band indicated in square brackets). Column 8: inclination from CO-based measurements. Column 9: references. (a) This work, (b) Boizelle et al. [19], (c) Krajnović et al. [97], (d) Smith et al. [168], (e) Rusli et al. [149], (f) Barth et al. [6], (g) Waters et al. [195], (h) Boizelle et al. [18], (i) Schulze and Gebhardt [156], (j) Davis et al. [44], (k) Rusli et al. [150], (l) Dominiak et al. [47], (m) Kabasares et al. [88].
† The reported errors for NGC 524 parameters are 3σ regions; we divide them by 3 to approximate the 1σ regions, as quoted for all other galaxies.

one-to-one relation with an intrinsic scatter term has roughly the same support as a linear relation with free slope, intercept, and intrinsic scatter. The current data therefore do not indicate statistically significant biases between the masses inferred from the two methods.

At our best estimates of $M_{\rm BH} = 3.0\times10^9 M_\odot$ and $D = 65.9$ Mpc, the NGC 315 SMBH has an angular shadow size of $\theta = 2\sqrt{27}GM_{\rm BH}/c^2D \approx 4.7\,\mu$as. Together with its relatively high millimeter flux, NGC 315 is a prime candidate target for future event horizon scale imaging missions (e.g., Johnson et al. [87]; Zhang et al. [199]; Ben Zineb, Ozel, and Psaltis [9]). A successful measurement of the shadow size would provide another independent estimate of this SMBH's mass.

Appendix

4.A Luminosity Density Profiles

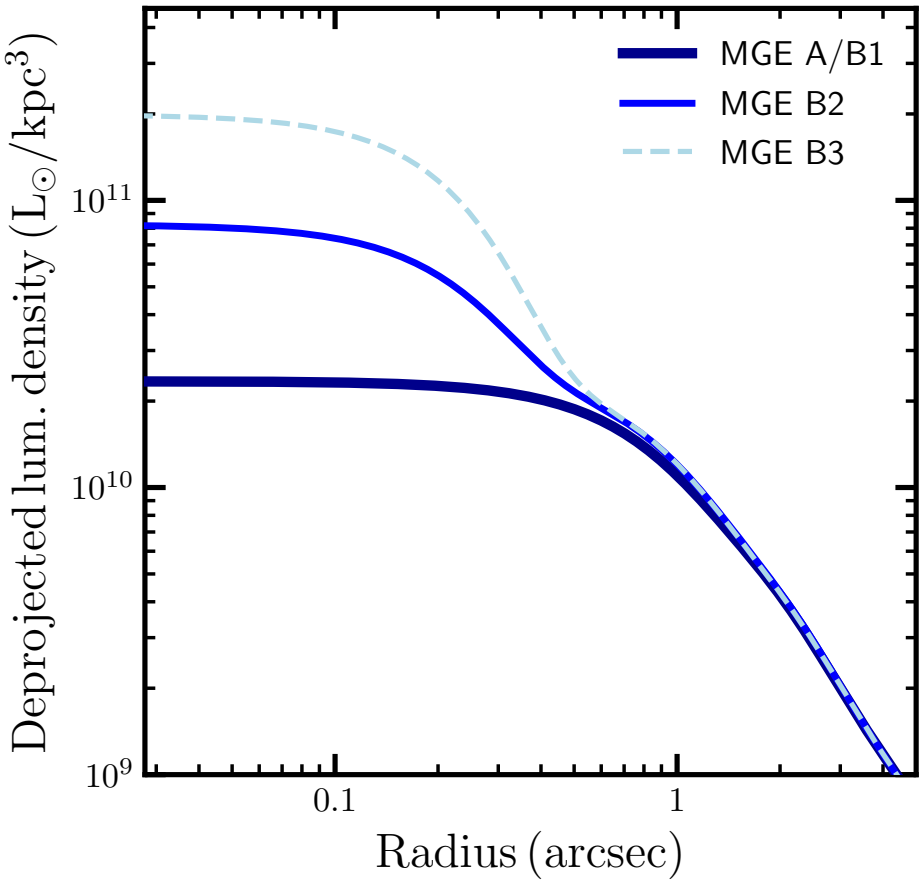

Figure 4.7: Comparison of the deprojected 3D luminosity density for the three MGE models of NGC 315 presented in Boizelle et al. [19]. The large bumps in the central 3D luminosity densities of model B2 and B3 are an artifact of the small widths of the central Gaussian component of these two models, $\sigma' = 0''.178$ and $0''.119$, respectively. In comparison, model A has $\sigma' = 0''.580$ for the central component and is well behaved upon deprojection.

Acknowledgements

We acknowledge support from NSF-AST-2206219, NSF AST-2206307, and the Heising-Simons Foundation. This work used the Extreme Science and Engineering Discovery Environment (XSEDE) at the San Diego Supercomputing Center through allocation AST180041, which is supported by NSF grant ACI-1548562. Portions of this research were conducted with the advanced computing resources provided by Texas A&M High Performance Research Computing. This work is based in part on data obtained at the international Gemini Observatory, a program of NSF's NOIRLab, which is managed by the Association of Universities for Research in Astronomy (AURA) under a cooperative agreement with the National Science Foundation on behalf of the Gemini partnership: the National Science Foundation (United States), the National Research Council (Canada), Agencia Nacional de Investigación y Desarrollo (Chile), Ministerio de Ciencia, Tecnología e Innovación (Argentina), Ministério da Ciência, Tecnologia, Inovações e Comunicações (Brazil), and Korea Astronomy and Space Science Institute (Republic of Korea). This work is based in part on observations made with the NASA/ESA Hubble Space Telescope, obtained at the Space Telescope Science Institute, which is operated by the Association of Universities for Research in Astronomy, Inc., under NASA contract NAS5-26555. These observations are associated with program GO-14219.

Chapter 5

SuperWISE: A WISE-Based Galaxy Catalog for Local Supermassive Black Hole Demographics

This chapter describes the construction of *SuperWISE*, an all-sky galaxy catalog developed for local SMBH demographics and future PTA multi-messenger applications. The catalog combines WISExSuperCOSMOS and 2MPZ into a single unified catalog of sky positions, photometric redshifts, and photometric measurements including WISE. We use the WISE photometry to estimate stellar masses, calibrate the resulting mass scale against independent K-band estimates where possible, and assign approximate SMBH masses using empirical black hole–host-galaxy scaling relations. As a validation step, we test the catalog against published local GSMF and BHMF measurements and find that it produces plausible reconstructions of both. This chapter is a work-in-progress of a full publication and will be submitted shortly after graduation.

5.1 Introduction

Pulsar timing arrays (PTAs) are increasingly sensitive to nanohertz gravitational waves from supermassive black hole binaries. Recent PTA studies, including the NANOGrav 15 yr analysis, have reported evidence for a stochastic gravitational-wave background with an amplitude consistent with expectations from the cosmic population of SMBH binaries [1]. As timing baselines grow and PTA sensitivity improves, the same data sets are expected to become sensitive to individual binaries [124, 132]. These first individual detections will be valuable multi-messenger targets, but their electromagnetic follow-up will be limited by the relatively large sky areas and broad distance uncertainties expected from PTA localization. Even optimistic localization regions can contain many plausible galaxies, motivating galaxy catalogs that reduce the host-galaxy search space using independent information about galaxy distance and mass [132].

The immediate goal of this work is to assemble a broad, all-sky sample with sky positions, photometric redshifts, WISE photometry, homogeneous stellar masses, and approximate SMBH masses to assist in PTA follow-up and localization. The catalog is built from WISExSuperCOSMOS and 2MPZ, with WISE-based stellar masses calibrated against an independent K-band mass scale. This combination is useful because PTA host identification requires both wide sky coverage and the retention of nearby massive galaxies, which are among the most likely hosts of the loudest binaries. Existing black hole–host-galaxy scaling relations then convert stellar masses into approximate black hole masses for population studies and localized PTA searches.

Throughout this work, we assume a flat ΛCDM cosmology with $\Omega_{\rm m} = 0.3$ and $H_0 = 70$ km s^{-1} Mpc^{-1}.

5.2 Data

The WISExSuperCOSMOS Survey

The backbone of our catalog is the WISExSuperCOSMOS Photometric Redshift Catalog (WSCOS; Bilicki et al. [13]), one of the largest all-sky photometric-redshift galaxy samples currently available. WSCOS combines infrared photometry from WISE (m_{W1} and m_{W2}; [197]) with optical photometry and morphology from SuperCOSMOS (B and R; [74]). The WISE bands provide sensitive mid-infrared measurements that are well matched to massive galaxies and less affected by modest Galactic extinction than optical data, while the SuperCOSMOS measurements improve star–galaxy separation and photometric-redshift performance. The catalog construction begins from more than 20 million candidate sources and applies magnitude, color, extinction, and angular masks to reduce stellar and Galactic contamination. The final masked WSCOS sample contains roughly 18.5 million galaxies, covers more than 70% of the sky, reaches $z \simeq 0.5$, and has a median redshift of $z \approx 0.2$.

The WSCOS catalog construction on its own applies several selection criteria to ensure data quality before the final photometric-redshift catalog is defined. These include Galactic latitude cuts of $|b| > 10°$ and $|b| > 17°$ near the Galactic center, magnitude limits of $B < 21$ (AB), $R < 19.5$ (AB), and $13.8 < m_{W1} < 17$ (Vega), and an extinction cut of $E(B - V) < 0.25$. Contamination is further reduced with quasar-cleaning cuts, adaptive position-dependent $(m_{W1} - m_{W2})_{\rm obs}$ cuts for stellar rejection, and a final angular mask. Photometric redshifts are then derived with the ANNz artificial neural-network framework using the four-band photometry (B, R, m_{W1}, m_{W2}), trained against GAMA-II spectroscopic redshifts [13]. The resulting catalog achieves a mean bias of $\sim 10^{-3}$, a normalized scatter of $\sigma_z \approx 0.033$, and fewer than 3% outliers beyond $3\sigma_z$.

All magnitudes in the WSCOS survey are corrected for Galactic extinction using the dust maps of Schlegel, Finkbeiner, and Davis [155]. The coefficients are revised following Schlafly and Finkbeiner [154], with $A_B/E(B-V) = 3.44$ and $A_R/E(B-V) = 2.23$ for SuperCOSMOS, and $A_{W1}/E(B-V) = 0.169$ and $A_{W2}/E(B-V) = 0.130$ for WISE [80].

WSCOS is therefore a natural backbone for an all-sky galaxy catalog. Its main drawback for the present application is the deliberate bright-end cut at $m_{W1} < 13.8$. That cut removes many nearby galaxies already represented in the 2MASS Extended Source Catalog and helps suppress bright WISE stellar contamination, but it also excludes exactly the kind of luminous local galaxies that are most relevant for PTA host searches. The 2MASS-based catalog introduced next fills in this bright nearby population.

The 2MASS Photometric Redshift Survey

The 2MASS Photometric Redshift catalog (2MPZ; Bilicki et al. [12]) provides a complementary all-sky sample at the bright, low-redshift end. 2MPZ is constructed by cross-matching the 2MASS Extended Source Catalog (XSC; [81, 167]) with WISE and SuperCOSMOS photometry, then estimating photometric redshifts with an artificial neural network trained on spectroscopic redshifts from SDSS, 6dFGS, and 2dFGRS. Because the sample begins with the 2MASS XSC, its depth is set primarily by the shallower 2MASS selection rather than by the deeper WISE photometry. The resulting catalog contains 928,352 galaxies in the version used here and provides nearly all-sky coverage outside the most strongly contaminated Galactic regions.

In broad terms, the 2MPZ selection used here follows the standard quality cuts described by Bilicki et al. [12], including a bright K_s-selected sample, extinction-corrected $J - K_s > 0$, detections in the multi-band optical/NIR/MIR photometry, and cuts on Galactic extinction and local stellar density to suppress stars and artifacts.

Photometric redshifts in 2MPZ achieve a normalized scatter of $\sigma_z \approx 0.015$ with very low outlier fractions for nearby galaxies. A subset of sources also have spectroscopic redshifts from the 2MASS Redshift Survey (2MRS; [79]), which provides external validation for $\sim$45,000 bright galaxies ($K_s \lesssim 11.75$). Where 2MRS and 2MPZ overlap, the photometric redshifts show excellent agreement with scatter consistent with the quoted $\sigma_z \simeq 0.015$.

Magnitudes in 2MPZ are corrected for Galactic extinction using the Schlegel, Finkbeiner, and Davis [155] dust maps, but the adopted coefficients differ from those used in WSCOS. For the WISE bands, Bilicki et al. [12] use $A_{W1}/E(B-V) = 0.231$ and $A_{W2}/E(B-V) = 0.194$ from Flaherty et al. [61]. For the 2MASS bands, the extinction corrections use the Cardelli, Clayton, and Mathis [35] law, corresponding approximately to $A_J/E(B-V) = 0.902$, $A_H/E(B-V) = 0.576$, and $A_{K_s}/E(B-V) = 0.367$. We do not attempt to rederive the parent-catalog photometry with consistent coefficients. Instead, the merged workflow keeps the native corrected magnitudes from each survey and, for the small set of duplicate objects discussed below, retains the WSCOS entry. The extinction corrections in the W1 band should be small (and our sample is preferentially in regions of low extinction), so we do not expect our results to depend significantly on these coefficients. Figure 5.1 and Figure 5.2 summarize the resulting redshift and WISE-photometry distributions. 2MPZ supplies the bright, nearby tail, while WSCOS dominates the fainter and more distant population.

Overlapping Sources and Ancillary Catalog Columns

The 2MPZ and WSCOS catalogs contain a modest number of overlapping sources. Using exact matches in the `wiseID` column for the local catalog versions used here, we identify 5,923 sources present in both. These overlapping galaxies are preferentially among the brightest sources in WSCOS ($m_{W1} \lesssim 14.5$) and the faintest sources in 2MPZ ($m_{W1} \gtrsim 13.8$), representing the narrow tail of parameter space where the two survey selection functions intersect.

To avoid double-counting, we remove these matching rows from the 2MPZ catalog in favor of the WSCOS entries, which use the revised Schlafly and Finkbeiner [154] extinction coefficients. Redshifts for duplicate sources agree well. In the local catalog versions used here, the duplicate sample has median $\Delta z = -0.006$ and an outlier fraction of $\sim$4% for $|\Delta z|/(1+z) > 0.1$.

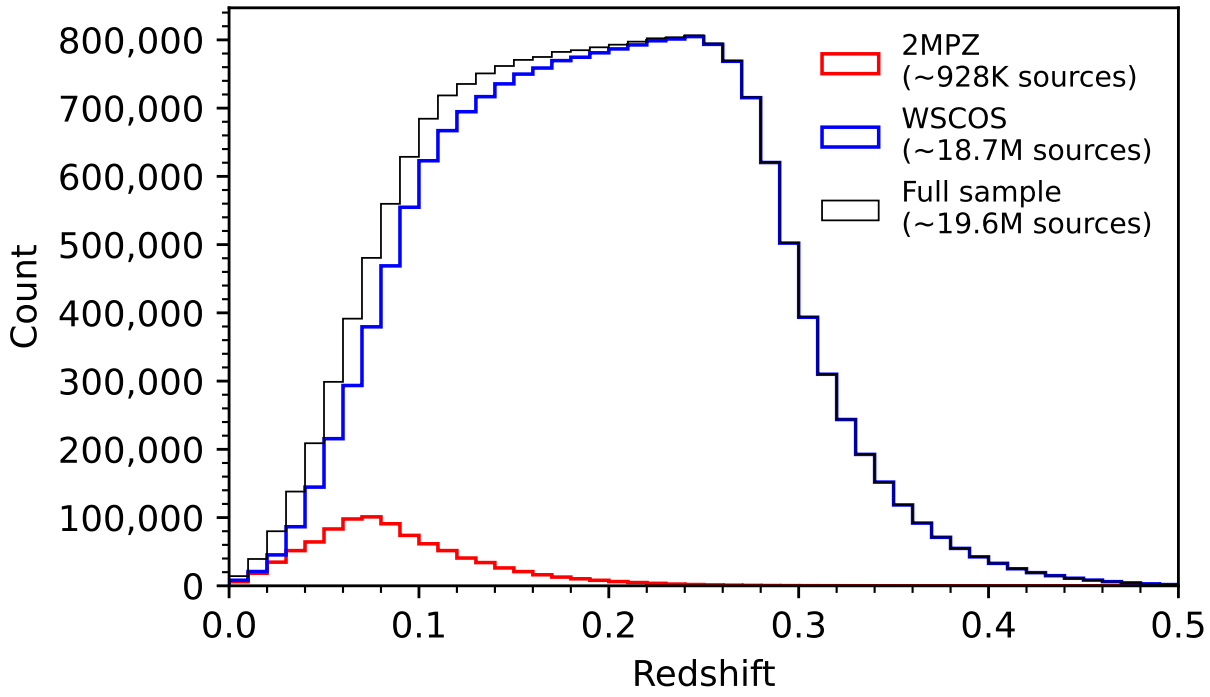

Figure 5.1: Redshift distribution for our final catalog of $\sim$19.6 million sources. The merged working catalog uses photometric-redshift fields from both parent surveys: the 2MPZ `ZPHOTO` column (renamed `zPhoto_Corr` in the notebook) and the WSCOS `zPhoto_Corr` column, both derived with empirically trained neural-network methods.

We retain several ancillary columns for later validation. For 2MPZ galaxies, the merged catalog preserves the spectroscopic-redshift column associated with the ANNz training and

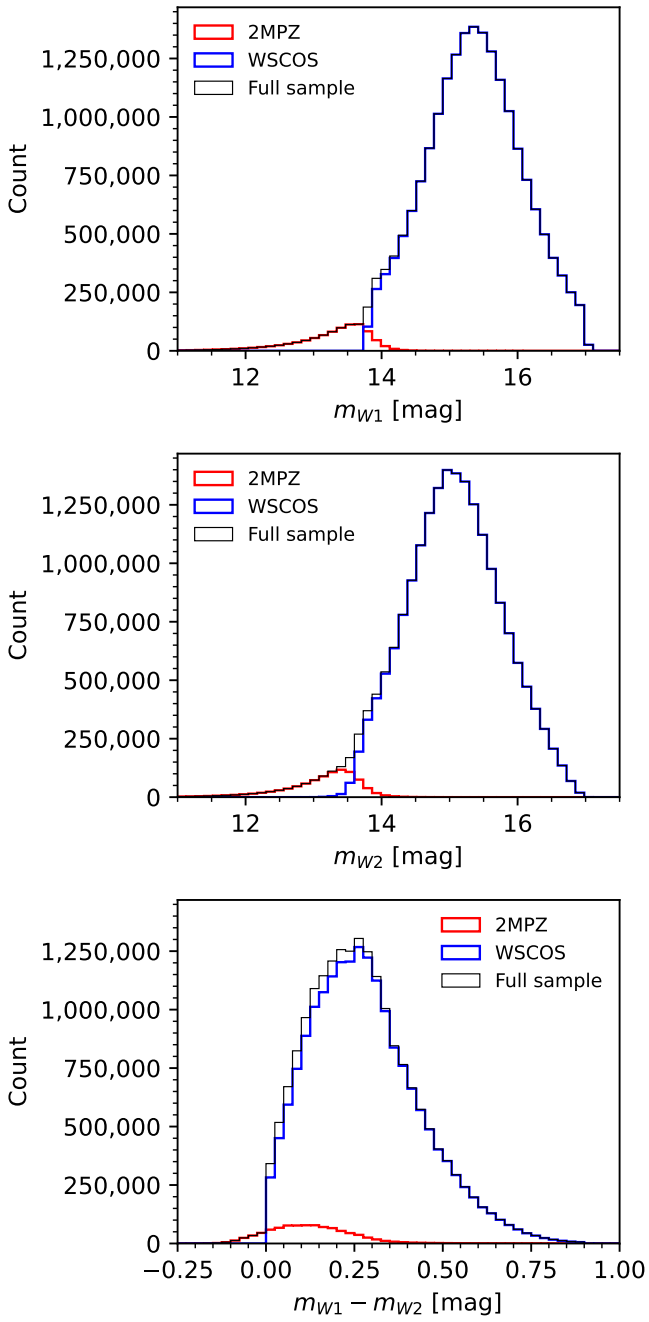

Figure 5.2: Distribution of observed m_{W1}, m_{W2}, and $(m_{W1} - m_{W2})_{\rm obs}$ values for the final sample of ∼19.6 million galaxies. 2MPZ preferentially contributes the brightest nearby galaxies, whereas WSCOS probes the much larger faint population. The overall shape of the distributions is dominated by the WSCOS sample.

Table 5.1: Properties of surveys used to construct our final catalog.

Sample	# of sources	$z_{\rm med}$
2MPZ	928,352	0.081
WISExSCOS	18,675,715	0.198
Combined	19,603,967	0.192

validation samples, but the stellar-mass calculations below use the photometric redshift field uniformly for both parent catalogs. We also cross-match the merged catalog to the MASSIVE Survey [113], a volume-limited sample of the most massive early-type galaxies within 108 Mpc, and recover 95 of its 116 galaxies. These matches carry available surface brightness fluctuation distances [84] and published dynamical black hole masses where available, providing direct checks on the high-mass end of the inferred black hole catalog.

5.3 WISE-based Stellar Masses

We estimate stellar masses from mid-infrared WISE m_{W1} (rest frame 3.4 μm) and m_{W2} (rest frame 4.6 μm) photometry. The m_{W1} band is a useful stellar-mass tracer because rest-frame 3–4 μm light is dominated by evolved stellar populations for most normal galaxies [83]. The $m_{W1} - m_{W2}$ color adds information about stellar population and dust-related changes in the mid-infrared mass-to-light ratio [38, 82].

The WISE-based stellar mass is written as

$$M_*^{\rm WISE} = L_{3.4\mu\ {\rm m}} \left(\frac{M_*}{L_{3.4\mu{\rm m}}} \right), \tag{5.1}$$

with the luminosity term given by the standard magnitude-to-luminosity conversion, $L_{3.4\mu{\rm m}} = 10^{-0.4\left(M_{3.4\mu\ {\rm m}} - M_{\odot,W1}\right)}$.

In this form, the calculation is expressed entirely in terms of rest-frame 3.4 μm and 4.6 μm quantities. The remainder of this section specifies how those rest-frame magnitudes are obtained from the observed WISE photometry by applying the distance modulus and the appropriate redshift-dependent k-corrections, after which the full stellar-mass estimator can be written in a single explicit working equation.

$W1$ k-Correction

For the m_{W1} band, the rest-frame 3.4 μm absolute magnitude is

$$M_{3.4\mu{\rm m}} = m_{W1} - \mu(z) - \mathcal{C}_{W1}(z), \qquad \mathcal{C}_{W1}(z) \equiv \frac{2.5\,\alpha z}{\ln 10}. \tag{5.2}$$

Here $\mu(z) \equiv 25 + 5\log_{10} d_L(z)$ is the distance modulus for luminosity distance d_L in Mpc, and $\mathcal{C}_{W1}(z)$ is the k-correction that converts observed m_{W1} photometry to the rest-frame

3.4 μm magnitude. Jarrett et al. [82] provides a convenient form for the k-correction, derived from synthetic photometry of galaxy templates over the redshift range $0 < z < 0.5$. This correction in flux form is $f_{3.4\mu\mathrm{m}} = f_{W1}e^{\alpha z}$ with $\alpha = -2.614$; Equation 5.2 uses the equivalent magnitude form. Since the SEDs of normal galaxies around the WISE bands generally decline with wavelength, galaxies at $z > 0$ appear brighter in observed $W1$ than they would in the rest-frame band. The $W1$ k-correction therefore makes the rest-frame $M_{3.4\mu\mathrm{m}}$ fainter.

Other near-infrared prescriptions give corrections of similar size over the low-redshift range relevant here. Kettlety et al. [90] used a passive-galaxy power-law SED for a selected GAMA sample at $z \leq 0.15$, obtaining $k_{W1} = -7.1\log_{10}(1+z)$. Bell et al. [8] reported a low-redshift near-infrared scaling $k(z) \simeq -(2.1 \pm 0.3)z$, while Glazebrook et al. [65] found an approximately linear low-redshift K-band correction, often written as $k(z) \simeq -2.25z$. These are broadly consistent with the low-redshift form of our adopted correction, $\mathcal{C}_{W1}(z) \simeq -2.84z$, while keeping the calibration tied directly to WISE templates.

Color-Based Mass-to-Light Calibration

A second ingredient in the WISE-based mass estimate is the calibration between rest-frame mid-infrared color and stellar mass-to-light ratio. Previous WISE studies have commonly parameterized this relation as a linear function of color,

$$\log_{10}\left(\frac{M_*}{L_{3.4\mu\mathrm{m}}}\right) = A_1\,(m_{3.4\mu\mathrm{m}} - m_{4.6\mu\mathrm{m}}) + A_0. \tag{5.3}$$

We adopt this empirical form, and in the next subsection describe how the observed $(m_{W1} - m_{W2})$ color is mapped to this rest-frame quantity before Equation 5.3 is applied catalog-wide.

Several calibrations of the coefficients A_0 and A_1 exist in the literature. The original calibration by Jarrett et al. [83], based on 17 nearby resolved galaxies, gave $A_0 = -0.246$ and $A_1 = -2.100$. Cluver et al. [38] recalibrated the relation using the much larger GAMA sample and found $A_0 = -0.03$ and $A_1 = -1.96$, while Jarrett et al. [82] later used the GAMA-KiDS-VIKING G23 field to obtain $A_0 = -0.376$ and $A_1 = -1.053$. The three calibrations differ most strongly for blue $W1 - W2$ colors, where the inferred mass-to-light ratio is highest. The Cluver et al. [38] relation gives larger $M_*/L_{3.4\mu\mathrm{m}}$ values than the Jarrett et al. [83] and Jarrett et al. [82] relations over much of the color range populated by this catalog. The differences reflect changes in the calibrating samples, stellar-population mix, total-flux measurements, and reference stellar masses across the three studies.

We choose to adopt the Cluver et al. [38] coefficients ($A_0 = -0.03$, $A_1 = -1.96$) for two reasons. First, Duey et al. [48] compare WISE-based stellar masses to independent Spitzer 3.6 μm-based masses and find that the Cluver et al. [38] calibration remains broadly consistent with their preferred stellar-mass scale, while the newer Jarrett et al. [82] calibration gives masses that are difficult to reconcile with their data (with Jarrett et al. [82] being generally undermassive). Second, Pálfi, Dálya, and Raffai [129] test fast infrared stellar-mass estimators for gravitational-wave host-galaxy applications and find that the Cluver et al. [38]

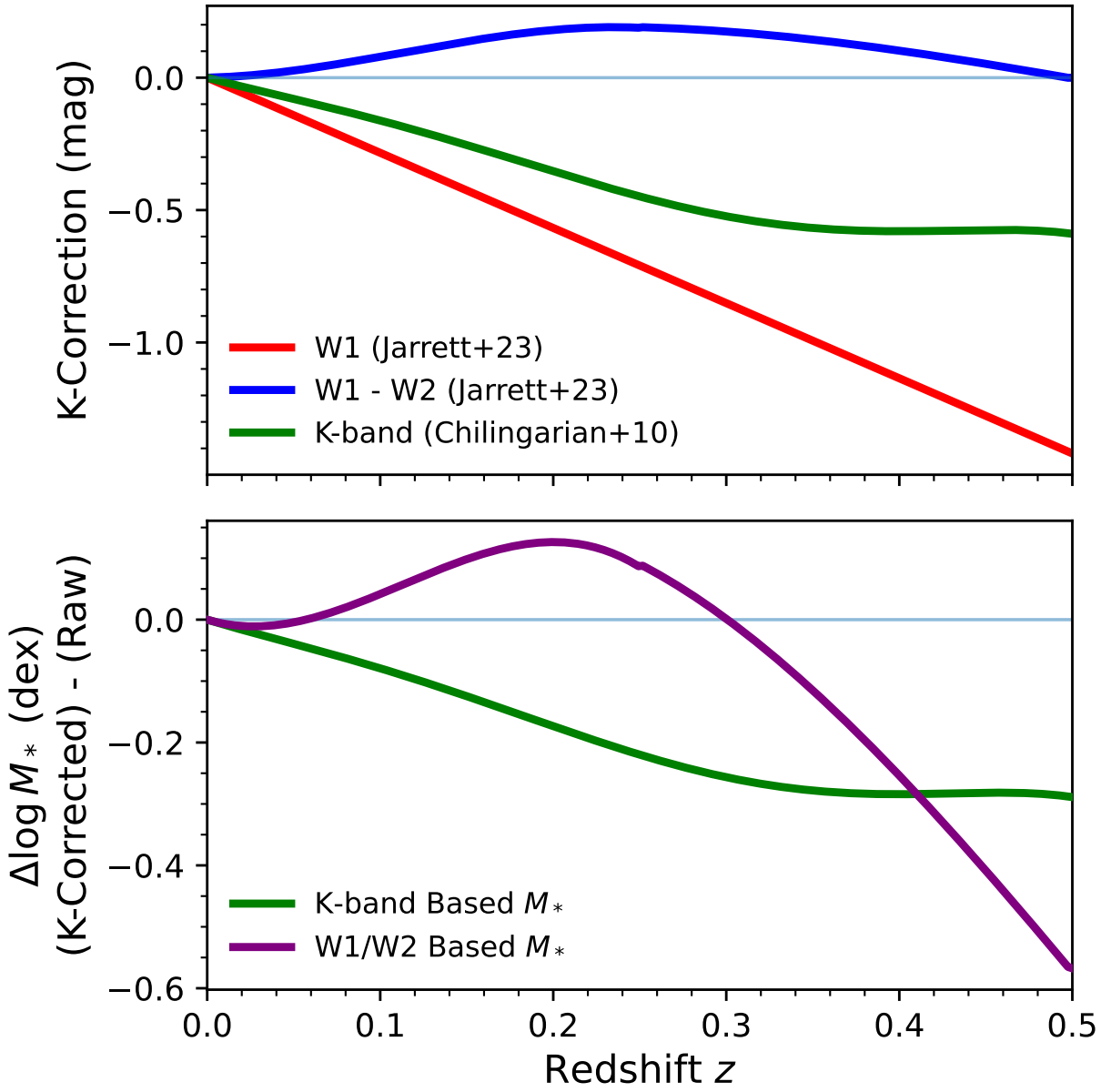

Figure 5.3: Differential k-correction effects showing the theoretical mass shift when k-corrections are applied. Top: component trends entering the WISE and K-band correction terms as a function of redshift (red: m_{W1} correction, blue: $(m_{W1} - m_{W2})$ color correction, green: K-band correction). The $W1$ and K-band terms have the same sign and generally make galaxies fainter in the rest frame, whereas the color correction acts in the opposite sense over most of the plotted range. Bottom: the corresponding net stellar-mass shifts, showing that the K-band method decreases monotonically with redshift while the combined WISE correction increases the inferred mass to $z \sim 0.3$ before turning over.

prescription gives smaller residual scatter and lower root-mean-square differences relative to GAMA reference stellar masses than the Jarrett et al. [83] method. These comparisons motivate using the Cluver et al. [38] relation rather than adopting the newest WISE calibration by default. However, as with any photometric stellar-mass calibration, the zero point of this relation also inherits the IMF assumptions of the reference stellar-population models used to define the calibration. We discuss the possibility and potential effects of IMF variation in the next section, though a full treatment of object-by-object analysis is beyond the scope of this paper.

We note that, following Jarrett et al. [82], the rest-frame color supplied to Equation 5.3 is clipped to the interval $[-0.2, 0.4]$. Their Figure 3 and accompanying text show that the calibrated $W1 - W2$ relation is constrained over this color interval; outside it the sample is sparse and the inferred $\Upsilon_{3.4\mu\mathrm{m}}$ is effectively limited rather than safely extrapolated. We adopt the same clipping to avoid extending the calibration into poorly sampled color regimes.

Figure 5.4 shows that the adopted Cluver et al. [38] relation is steeper than the Jarrett et al. [83] and Jarrett et al. [82] alternatives across the central color range, with the largest offsets at the blue, high-M/L end. Applying the clipped Cluver et al. [38] relation to the merged catalog produces a broad rest-frame color distribution and a correspondingly broad catalog-wide $M_*/L_{3.4\mu\mathrm{m}}$ distribution. As a population-level check, the bottom panel compares the catalog $M_*/L_{3.4\mu\mathrm{m}}$ distribution to the Kettlety et al. [90] passive-galaxy benchmark, $M_*/L_{W1} = 0.65 \pm 0.07$. The catalog distribution overlaps this benchmark but extends to both lower and higher M/L, as expected for an all-sky sample which has a variable mass-to-light ratio as a function of color (in contrast to Kettlety et al. [90] who quotes a single mass-to-light for all galaxies).

$m_{W1} - m_{W2}$ Color k-Correction

Jarrett et al. [82] also provide a piecewise polynomial correction derived from synthetic galaxy photometry, capturing the non-linear evolution of the observed color as mid-infrared features shift through the $W2$ band. This calibration reflects contributions from evolved stellar populations and warm dust, with separate regimes below and above $z = 0.25$ to account for changes in the dominant spectral features.

We write the rest-frame color correction as

$$(m_{3.4\mu\mathrm{m}} - m_{4.6\mu\mathrm{m}}) = (m_{W1} - m_{W2}) - \mathcal{C}_{W1-W2}(z), \tag{5.4}$$

where

$$\mathcal{C}_{W1-W2}(z) = \begin{cases} 0.142\,z + 9.193\,z^2 \\ \quad - 26.980\,z^3, & z < 0.25 \\ -\,0.040 + 2.258\,z \\ \quad - 6.306\,z^2 + 3.875\,z^3, & 0.25 \le z < 0.5. \end{cases} \tag{5.5}$$

Jarrett et al. [82] derived this approximation from template-based synthetic photometry and describe it as a convenient approximation to the full SED-based correction, but caution

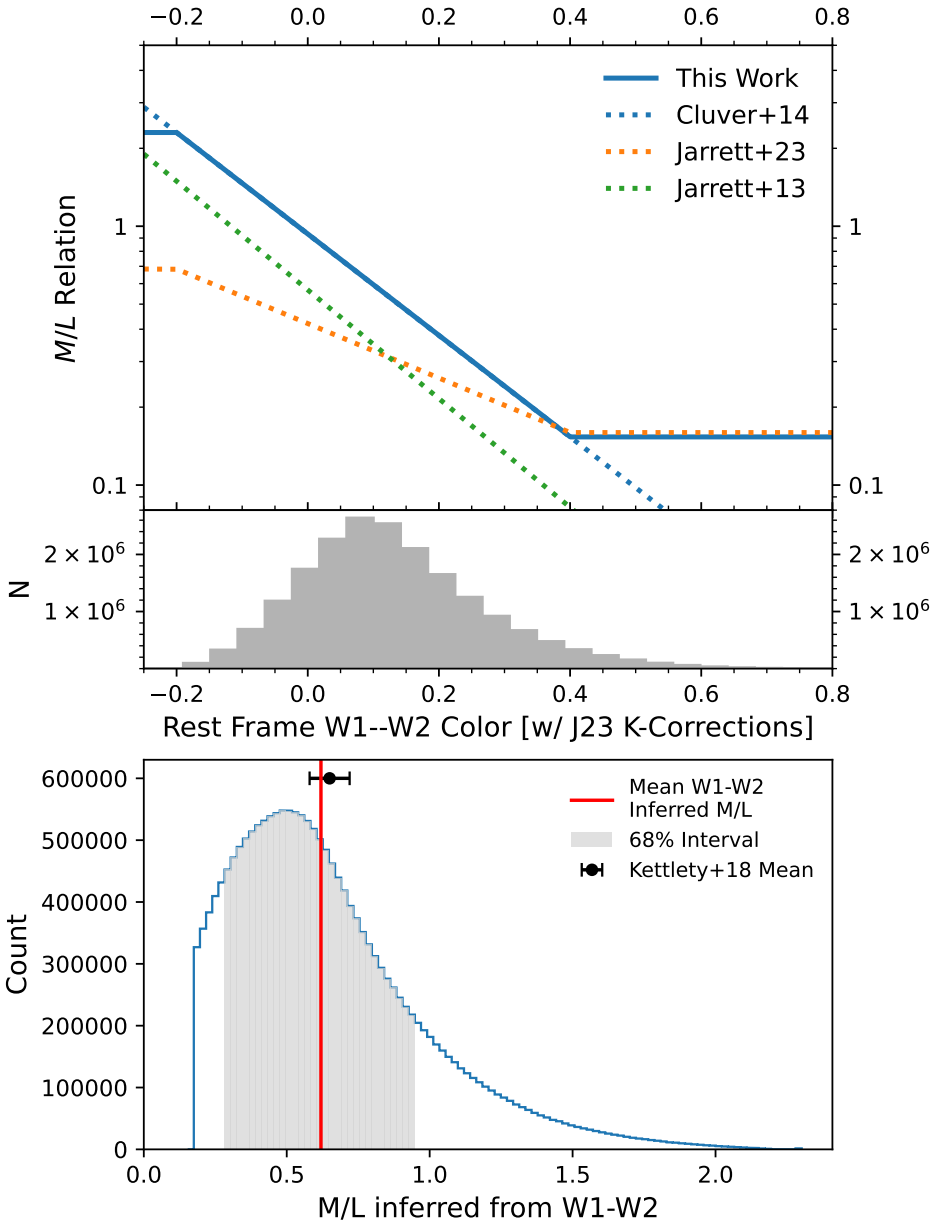

Figure 5.4: Comparison of mid-infrared mass-to-light calibrations, the full rest-frame color distribution, and the resulting catalog-wide mass-to-light distribution for the full merged WSCOS+2MPZ catalog. Top: $\log(M_*/L_{3.4\mu\mathrm{m}})$ versus rest-frame $(m_{W1} - m_{W2})$, showing the Cluver et al. [38] fiducial relation, the adopted clipped version used in this work, and the Jarrett et al. [83] and Jarrett et al. [82] alternatives. Middle: histogram of the full rest-frame color distribution for the merged catalog, shown over the same displayed color range as the top panel. Bottom: histogram of the corresponding $M_*/L_{3.4\mu\mathrm{m}}$ values for the full catalog; the red line marks the catalog mean, the gray shading marks the central 68% interval, and the shaded Kettlety et al. [90] band marks the passive-galaxy benchmark reported by Kettlety et al. [90].

that the k-correction to the color is, in general, galaxy dependent. Their Appendix A shows that the low-z behavior differs somewhat between early and late types, with the adopted polynomial based on an Sb template as a practical middle ground for normal galaxies. As with the $W1$ correction above, the intended calibration range is $0 < z < 0.5$; beyond that range, Jarrett et al. [82] recommend full SED modeling rather than polynomial extrapolation.

The top panel of Figure 5.3 shows the polynomial k-correction given by Equation 5.5. Over the plotted redshift range, $\mathcal{C}_{W1}(z)$ changes the rest-frame luminosity term, while $\mathcal{C}_{W1-W2}(z)$ changes the color supplied to Equation 5.3.

WISE-Based Stellar Masses

With the distance modulus and the WISE k-corrections in place, we can combine all the ingredients from the preceding sections into a single expression that maps observed WISE photometry and redshift directly to stellar mass.

$$\begin{aligned}\log_{10}(M_*^{\mathrm{WISE}}/M_\odot) = &-0.4\,(m_{W1} - \mu(z) - \mathcal{C}_{W1}(z) - M_{\odot,W1}) \\ &+ A_1\,[(m_{W1} - m_{W2}) - \mathcal{C}_{W1-W2}(z)] \\ &+ A_0.\end{aligned} \tag{5.6}$$

Equation 5.6 is the working formula adopted in the catalog construction. Here m_{W1} and m_{W2} are the observed apparent magnitudes, $\mu(z)$ is the standard distance modulus, $\mathcal{C}_{W1}(z)$ is the $W1$ correction defined in Equation 5.2, $\mathcal{C}_{W1-W2}(z)$ is the color correction defined in Equation 5.5, and $M_{\odot,W1} = 3.24$ is the solar absolute magnitude in $W1$ [83]. The coefficients A_0 and A_1 are the adopted parameters of the color-based mass-to-light calibration discussed in Section 5.3.

The catalog calculation clips the rest-frame color $(m_{W1} - m_{W2}) - \mathcal{C}_{W1-W2}(z)$ to $[-0.2, 0.4]$ before applying Equation 5.6. The lower panel of Figure 5.3 shows the combined mass effect of the WISE corrections. The W1/W2-based correction first raises $\log M_*^{\mathrm{WISE}}$ to $z \sim 0.3$ and then turns over. This non-monotonic behavior is driven by the polynomial form of $\mathcal{C}_{W1-W2}(z)$. At low and intermediate redshift the color term steepens the adopted M_*/L enough to outweigh the W1 luminosity dimming, whereas at higher redshift the flux correction dominates and the net mass shift decreases.

Figure 5.5 shows the resulting stellar-mass distribution for the full merged catalog in four redshift bins chosen to approximately balance the number of galaxies per bin. The bins are $0 \le z < 0.129$ (N = 4,908,624), $0.129 \le z < 0.192$ (N = 4,854,344), $0.192 \le z < 0.254$ (N = 4,952,984), and $z \ge 0.254$ (N = 4,883,422). The mass distribution shifts systematically to higher stellar masses with increasing redshift. This is expected for a flux-limited survey, since galaxies at larger distances must be intrinsically brighter, and therefore typically more massive, to remain above the survey limits.

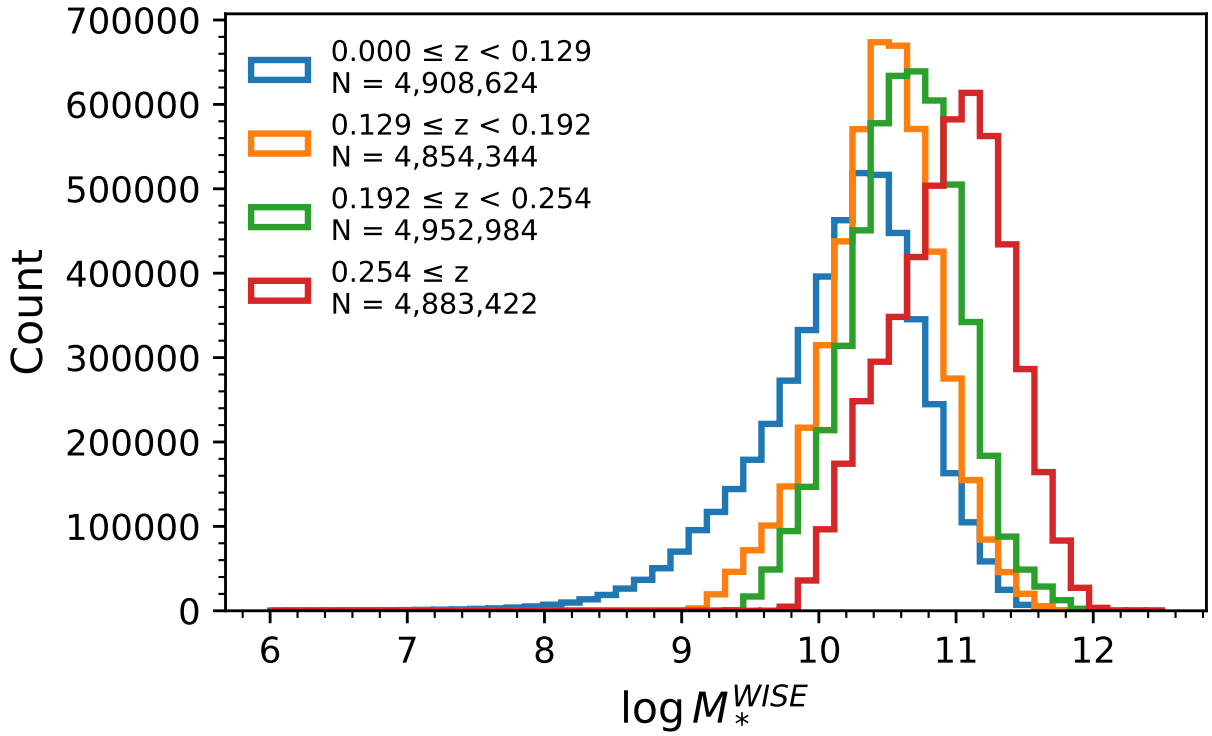

Figure 5.5: Distribution of $\log M_*^{\mathrm{WISE}}$ for the full merged WSCOS+2MPZ catalog, shown as counts in four approximately equal-count redshift bins: $0 \leq z < 0.129$, $0.129 \leq z < 0.192$, $0.192 \leq z < 0.254$, and $z \geq 0.254$. The progressive shift toward higher stellar masses with increasing redshift reflects the Malmquist bias of the flux-limited survey.

5.4 K-Band Stellar Masses and Consistency Check

K-Band Stellar Mass Calibration

To test the consistency of the WISE-based masses in Equation 5.6, we compare them to stellar masses derived from near-infrared 2MASS K-band photometry for the subset of galaxies that inherit usable XSC-derived K-band information from the 2MPZ side of the merged sample. This comparison is useful because the WISE and K-band estimators use different photometric bands and different empirical calibrations.

The two K-band calibrations used here were derived from distinct samples that span complementary luminosity ranges. The Cappellari [25] relation was calibrated using early-type galaxies for which no object reaches $M_K \lesssim -25.6$. Conversely, the Liepold and Ma [106] calibration is anchored to a subset of MASSIVE Survey galaxies [113], which by construction occupy the luminous nearby regime and contain essentially no sources fainter than $M_K \approx$

-25.6. The combined relation is thus:

$$\log_{10}(M_*^K/M_\odot) = \begin{cases} 11.92 - 0.49\,(M_{2.2\mu\mathrm{m}} + 26), & M_{2.2\mu\mathrm{m}} < -25.6 \\ 11.90 - 0.44\,(M_{2.2\mu\mathrm{m}} + 26), & M_{2.2\mu\mathrm{m}} \geq -25.6. \end{cases} \tag{5.7}$$

Both relations have comparable intrinsic scatter, with $\epsilon \approx 0.14$ dex for the Cappellari [25] calibration and $\epsilon \approx 0.16$ dex for the Liepold and Ma [106] calibration.

K-Band k-Correction

Because the K-band calibrations are defined in the rest frame, the observed 2MASS K_s magnitudes must be k-corrected before Equation 5.7 is applied. We write

$$M_{2.2\mu\mathrm{m}} = m_K - \mu(z) - \mathcal{C}_K(z), \tag{5.8}$$

and adopt the Chilingarian, Melchior, and Zolotukhin [37] polynomial

$$\mathcal{C}_K(z) = -1.75997z + 5.48023z^2 - 56.4175z^3 + 175.939z^4 - 160.754z^5. \tag{5.9}$$

The K-band correction is simpler than the combined WISE luminosity and color correction. Over the redshift range of this catalog it makes the rest-frame K-band magnitude fainter, lowering the inferred K-band stellar mass as shown by the green trend in the bottom panel of Figure 5.3.

Consistency Check Between WISE and K-Band Masses

Figure 5.6 compares the two mass-estimation methods for the subset of galaxies with both WISE photometry and usable XSC-derived K-band information. The upper panel shows the mass difference $\Delta \log_{10} M_* \equiv \log_{10} M_*^K - \log_{10} M_*^{\mathrm{WISE}}$ as a function of redshift. The data reveal a modest systematic offset between the two methods, with the K-band masses generally higher than the WISE-based estimates. We note that the tilted "tear-drop" shape in the panels is an artifact of the different survey depths; in general there should be a number of galaxies with lower WISE-based stellar masses in the panels, but these galaxies are not intrinsically bright enough and do not get detected in the parent surveys.

Several effects could contribute to the offset. First, the two estimates are tied to different calibrating data sets and different assumptions about stellar populations. Mid-infrared light is an efficient tracer of old stars, but the 3–5 μm bands can still receive contributions from thermally pulsing AGB stars, hot dust, and PAH emission, particularly in galaxies with recent star formation or non-negligible dust content [122, 128, 119]. Recent tests of infrared stellar-mass estimators by Pálfi, Dálya, and Raffai [129] find that WISE-based Jarrett et al. [82], Cluver et al. [38], and Kettlety et al. [90] methods tend to underestimate stellar masses for massive galaxies relative to GAMA reference masses, while the Cappellari [25] K-band method shows a weaker version of this trend. That behavior is qualitatively consistent

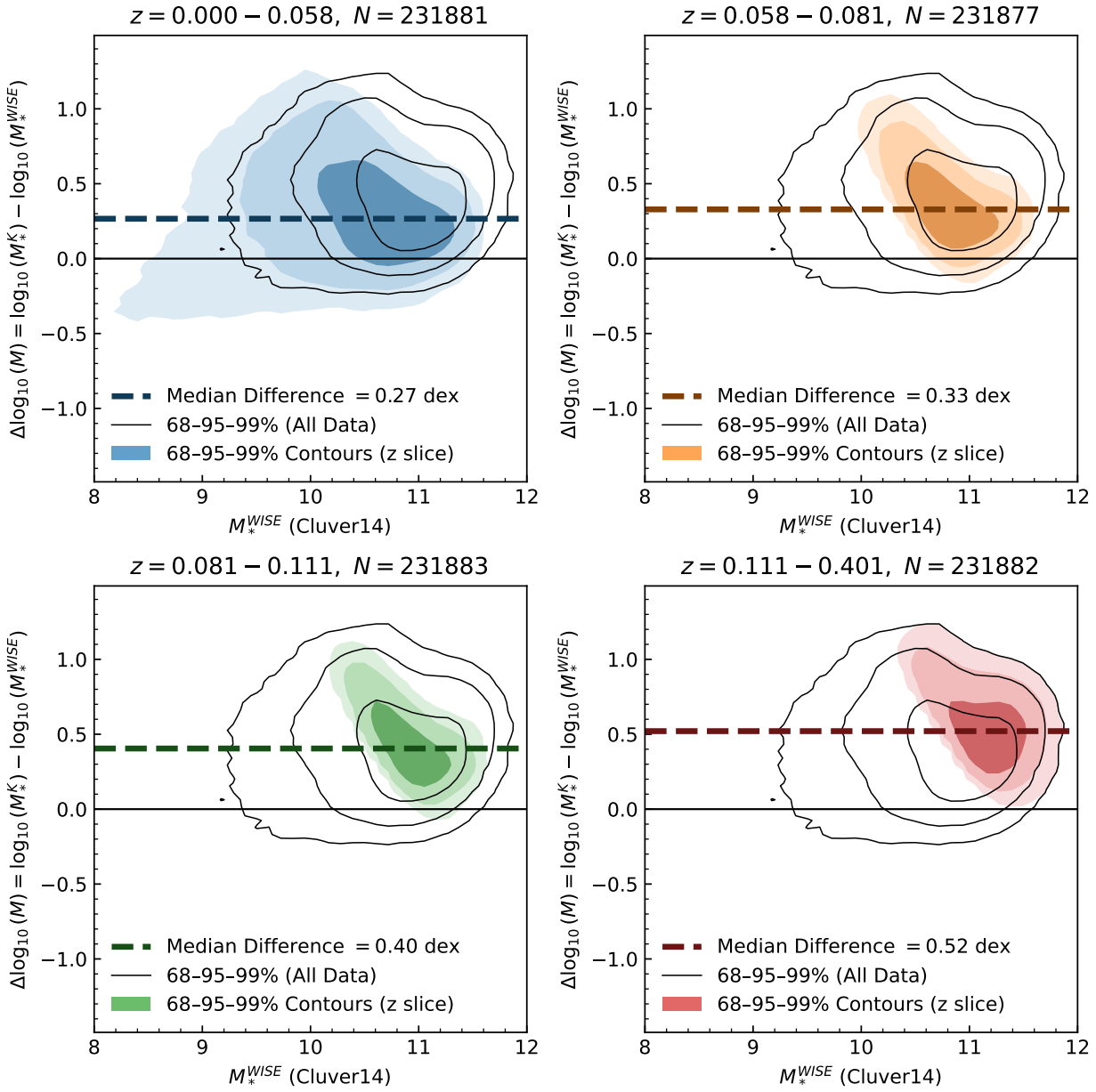

Figure 5.6: Mass difference (M_*^K minus $M_*^{\rm WISE}$, i.e. $\Delta \log_{10} M_* \equiv \log_{10} M_*^K - \log_{10} M_*^{\rm WISE}$) versus K-band stellar mass M_*^K for the 927,524-galaxy overlap sample with both 2MPZ K-band photometry and WISE $W1/W2$ measurements. Broadly speaking, there is a mass-dependent offset, with more massive systems exhibiting larger discrepancies between the two estimation methods. The four panels correspond to the redshift bins $0 \leq z < 0.058$, $0.058 \leq z < 0.081$, $0.081 \leq z < 0.111$, and $z \geq 0.111$. In each case, the pre-correction relation exhibits a positive slope with stellar mass, indicating a systematic bias in the WISE-based estimates. Overlaid is the best-fit ODR relation (solid line), which captures this trend.

with the positive $\Delta \log_{10} M_*$ seen here at the high-mass end. Finally, residual k-correction systematics may contribute to the redshift dependence because the WISE correction enters both the luminosity and the color-dependent M/L term.

An additional systematic worth highlighting, and which is especially relevant for the most massive galaxies, is the potential variation in the low-mass end of the stellar initial mass function (IMF). Low-mass stars contribute substantially to the stellar mass while adding comparatively little near- or mid-infrared light, so a more bottom-heavy IMF increases the stellar mass-to-light ratio at fixed luminosity. Several independent approaches have found evidence that massive early-type galaxies, especially systems with high velocity dispersion or old, alpha-enhanced stellar populations, can have heavier-than-Milky-Way IMF normalizations [34, 39, 169]. This is particularly relevant for the massive early-type galaxies that dominate the high-mass tail.

A second complication is that IMF variation may not be spatially uniform within a galaxy. Early spectroscopic evidence for IMF variation came from gravity-sensitive absorption features measured in the central regions of massive ETGs, where the inferred low-mass stellar content is often enhanced relative to a Milky-Way IMF [39, 169]. Recent work on the MASSIVE survey is especially relevant in this context, with Gu et al. [72] finding bottom-heavy central IMF normalizations for massive ETGs and an IMF mismatch that increases with velocity dispersion, stellar mass, and abundance indicators. The translation from these central IMF constraints to a total catalog stellar mass still depends on radial gradients in the stellar mass-to-light ratio [169], in contrast to the fixed mass-to-light ratio we are assuming in this work. If the most massive galaxies in the catalog have systematically heavier IMFs, a fixed-IMF WISE calibration would tend to underpredict their stellar masses, qualitatively matching the sense of the WISE-minus-K offset seen in Figure 5.6.

The K-band reference scale used here is calibrated against dynamical stellar masses rather than fixed-IMF stellar-population masses. It can therefore carry the average IMF-dependent stellar mass-to-light normalization of the dynamical calibration sample, rather than imposing a universal low-mass IMF through the photometric calibration itself. This does not make the K-band relation an object-by-object IMF measurement, since the calibration still depends on the galaxies used to define the relation and on the assumptions entering the dynamical stellar masses, but the distinction is important for interpreting the positive $M_*^K - M_*^{\rm WISE}$ offset at the high-mass end. The ODR correction applied below absorbs the net mass-dependent offset relative to the K-band reference scale, but it cannot distinguish IMF variation from photometric systematics, stellar-population effects, or calibration differences. Modeling IMF variation explicitly would require additional information, such as velocity dispersions, absorption-line constraints, or dynamical mass-to-light ratios, and is beyond the scope of this catalog-level analysis.

To account for this systematic behavior, we model the mass-dependent offset using orthogonal distance regression (ODR). Specifically, we fit a linear model of the form

$$\log_{10} M_*^K = a + b \log_{10} M_*^{\rm WISE}, \tag{5.10}$$

where a and b are free parameters determined from the low-redshift overlap sample with

finite WISE and K-band masses. In the fiducial ODR-corrected catalog used for the GSMF below, the fit is restricted to galaxies with $z < 0.05$, giving 167,021 calibration galaxies and best-fit parameters $a = -0.2505 \pm 0.0128$ and $b = 1.0515 \pm 0.0012$. This redshift cut keeps the calibration anchored to the nearby galaxies for which the K-band comparison is most directly relevant.

We then apply this relation as a correction to the WISE-based stellar masses, defining a corrected mass estimate via

$$\log_{10} M_*^{\mathrm{WISE},corr} = a + b \log_{10} M_*^{\mathrm{WISE}}. \tag{5.11}$$

By construction, this procedure brings the WISE-based masses into closer agreement with the K-band estimates, which we treat as the reference scale for the correction.

The impact of this correction is evident in Figure 5.7. Prior to correction, the residuals show a clear trend with stellar mass, with increasingly large offsets toward the high-mass end. After applying the ODR-based correction, this trend is substantially reduced. The distribution of $\Delta \log_{10} M_*$ becomes more symmetric about zero, indicating that the WISE-based masses have been brought into closer statistical agreement with the K-band reference scale.

Some residual structure persists at the highest masses, likely reflecting second-order effects not captured by the linear model, such as variations in stellar populations, photometric systematics, or differences between the WISE and K-band mass-to-light calibrations. Nonetheless, the corrected masses provide a substantially improved level of agreement across the full stellar mass range.

5.5 Construction of Local Mass Functions

Local Galaxy Stellar Mass Function

The corrected stellar masses can be used to construct a galaxy stellar mass function (GSMF) as a population-level check on the catalog. The GSMF is especially useful here because it tests the combined effect of the catalog selection, photometric redshifts, WISE mass calibration, and ODR correction against an external local benchmark. For the fiducial result shown below, we use the clipped Cluver et al. [38] WISE stellar masses after applying the ODR correction described in Section 5.4, and we restrict the displayed GSMF to only galaxies with $0 < z < 0.1$ for ease of comparison with other local measurements of the GSMF.

We estimate the GSMF using the standard $1/V_{\mathrm{max}}$ method. For each galaxy, we compute the maximum redshift z_{max} at which it would remain in the sample given the WISE $W1$ selection. The accessible comoving volume is then

$$V_{\mathrm{max},i} = f_\Omega \int_{z_{\mathrm{min}}}^{z_{\mathrm{max},i}} \frac{dV}{dz}\, dz, \tag{5.12}$$

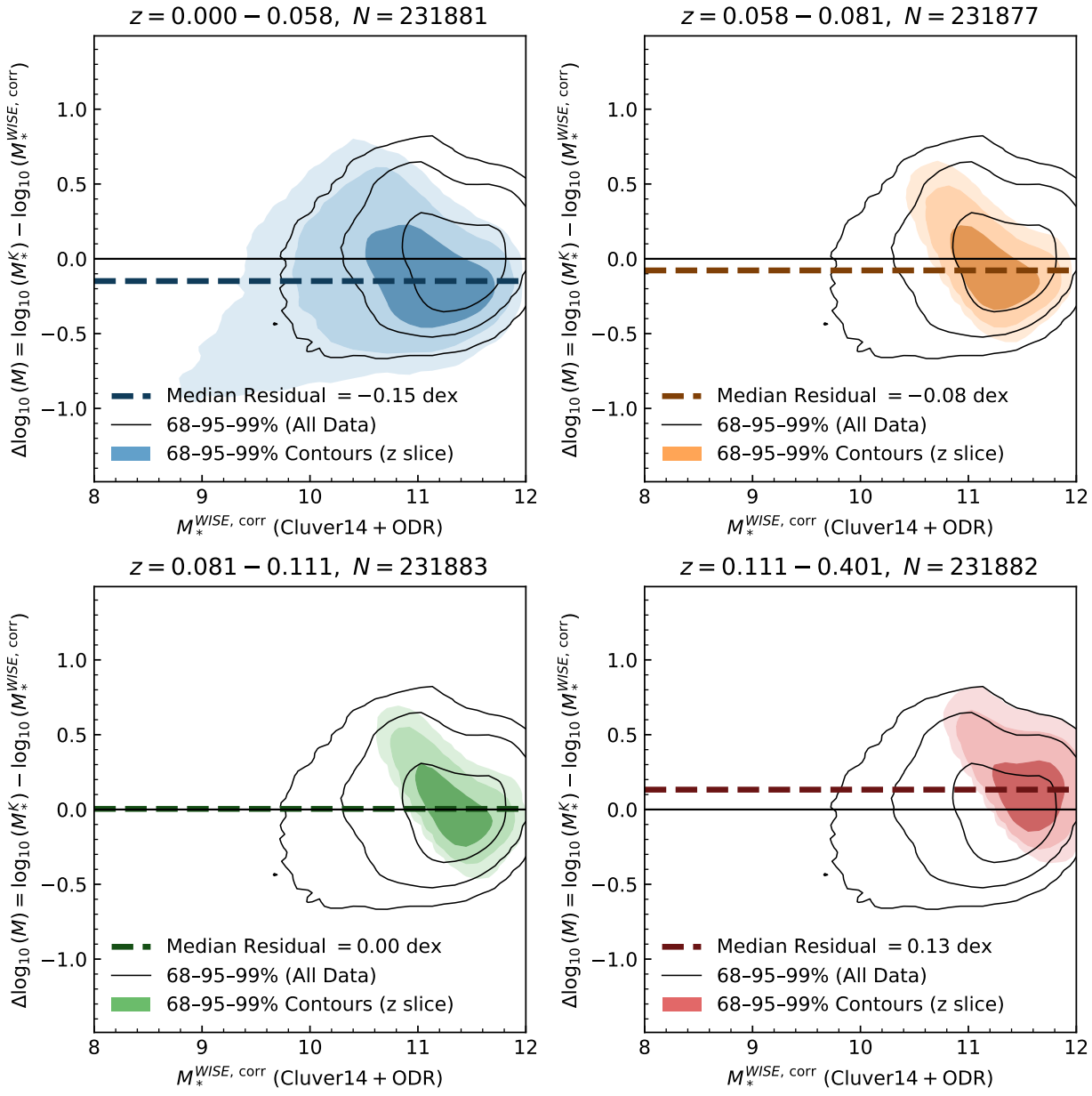

Figure 5.7: Same 927,524-galaxy overlap sample and redshift bins as Figure 5.6, but after applying the global ODR-based correction to the WISE masses. The mass-dependent trend is substantially flattened in each panel, leaving residuals that are more tightly centered on zero, with only modest structure persisting at the highest masses.

where f_Ω is the sky fraction after the survey mask and $z_{\rm min}$ is the lower redshift cut adopted for the mass-function calculation. We set $f_\Omega = 0.70$, matching the approximate high-Galactic-latitude sky coverage of the WSCOS parent catalog after masking. We use the WSCOS faint limit $W1_{\rm lim} = 17.0$, taken from Bilicki et al. [13]. The GSMF in a stellar-mass bin of width $\Delta \log_{10} M_*$ is then

$$\Phi(M_*)\,\Delta \log_{10} M_* = \sum_i \frac{1}{V_{{\rm max},i}}, \tag{5.13}$$

where the sum is over galaxies in that bin. We also apply a stellar-mass completeness cut following the approach of Pozzetti et al. [136]. Conceptually, this method asks what stellar mass each observed galaxy would have if its flux were moved to the survey limit at the same redshift, then uses the faintest galaxies in each redshift bin to define a conservative mass-completeness boundary. In practice, we select the faintest 20% of galaxies in $W1$ in each redshift bin and use the 95th percentile of their limiting masses as $M_{\rm lim}(z)$. For the fiducial ODR-corrected run, this gives $\log_{10} M_{\rm lim}/M_\odot = 9.32$ at $z = 0.05$ and 10.04 at $z = 0.1$. The completeness-filtered GSMF includes only galaxies above $M_{\rm lim}(z)$.

Figure 5.8 compares the resulting $0 < z < 0.1$ GSMF to the Liepold and Ma [106] $z = 0$ GSMF, who constructed a $z = 0$ GSMF by combining two complementary regimes. At lower masses, they adopt the census-based Leja et al. [103] GSMF, which is constrained by panchromatic SED modeling over a broad galaxy population. At the massive end, where large-volume local samples are required and standard photometric stellar masses become uncertain, Liepold and Ma [106] replace previous extrapolations with the volume-limited MASSIVE survey and stellar masses from detailed dynamical modeling or stellar-population modeling with a bottom-heavy IMF. Their resulting GSMF has a higher abundance above $M_* \gtrsim 10^{11.5} M_\odot$ than many earlier determinations and is therefore a particularly relevant benchmark for PTA applications, where the most massive galaxies dominate the expected high-$M_{\rm BH}$ population.

The two curves agree best near $\log_{10} M_*/M_\odot \simeq 10.2$–$10.6$. Below $\log_{10} M_*/M_\odot \simeq 10$, the catalog GSMF is lower, as expected for a WISE-selected catalog with a completeness boundary near $\log_{10} M_*/M_\odot \simeq 10$ at $z = 0.1$. At intermediate masses, $\log_{10} M_*/M_\odot \simeq 10.6$–$11.5$, the catalog lies above the Liepold and Ma [106] curve. The most relevant possible contributors are the ODR correction, residual incompleteness of the sample, selection-function effects in the merged parent catalogs, and systematic photometric-redshift errors. At the highest masses, the result is especially sensitive to photometric redshifts because a small number of rare luminous galaxies can move substantially in stellar mass when their distances change. These trends indicate that the catalog reproduces the broad local GSMF shape, while the remaining offsets are best interpreted as diagnostics of the catalog mass scale and selection function.

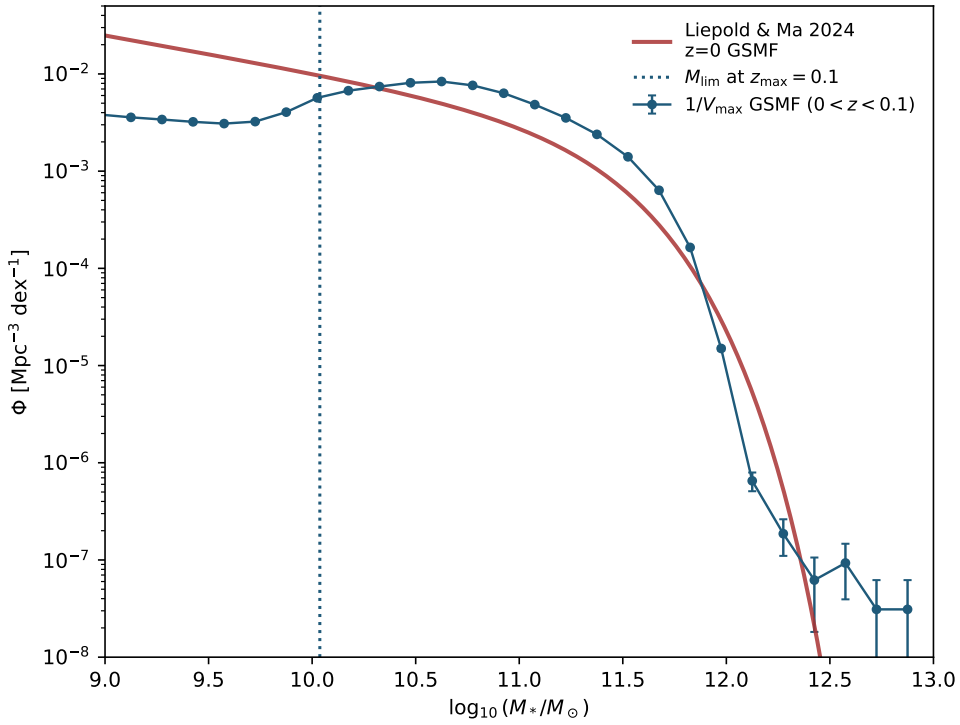

Figure 5.8: Galaxy stellar mass function (GSMF) estimated from the WSCOS+2MPZ catalog for $0 < z < 0.1$. The measurement uses ODR-corrected clipped Cluver et al. [38] stellar masses, a WISE-based $1/V_{\rm max}$ estimator, and a Pozzetti et al. [136]-style stellar-mass completeness cut. The vertical dotted line marks the completeness limit at $z_{\rm max} = 0.1$. The red curve shows the $z = 0$ GSMF from Liepold and Ma [106], which combines the Leja et al. [103] low- and intermediate-mass GSMF with the MASSIVE-survey constraint at the high-mass end.

Local Black Hole Mass Function

The black hole mass function (BHMF) is constructed by assigning black hole masses to the same galaxy sample used for the GSMF. As the external benchmark, we again use Liepold and Ma [106]. Their BHMF is derived from their $z = 0$ GSMF (again, anchored to the Leja et al. [103] GSMF at lower masses and to the MASSIVE survey at the high-mass end). This construction is directly motivated by the high-mass systems most relevant for nanohertz gravitational waves. In particular, Liepold and Ma [106] find an enhanced abundance of massive local galaxies and SMBHs relative to some earlier GSMF/BHMF determinations, with SMBHs above $\sim 10^{10} M_\odot$ remaining consistent with the small number of currently known extreme systems. They also note that the resulting local SMBH mass density is high compared to some accretion-based estimates, underscoring the known tension between relic BHMFs inferred from galaxy demographics and integrated quasar growth.

For the catalog-derived BHMF, black hole masses are assigned by drawing from the mean McConnell and Ma [118] black hole–bulge mass scaling relation. The catalog does not currently contain morphological decompositions or object-by-object bulge fractions, so we set $f_{\rm bulge} = 1$ and use the total stellar mass as the bulge mass. This assumption is reasonable for the massive early-type galaxies that dominate the high-$M_{\rm BH}$ tail, but it overestimates black hole masses for disk-dominated systems. The resulting BHMF can therefore be interpreted roughly as an upper limit where late-type galaxies contribute appreciably.

We draw from the mean McConnell and Ma [118] scaling relation,

$$\log_{10}\left(\frac{M_{\rm BH}}{M_\odot}\right) = \alpha + \beta \log_{10}\left(\frac{M_{\rm bulge}}{10^{11} M_\odot}\right) + \delta, \tag{5.14}$$

where we adopt $\alpha = 8.46$ and $\beta = 1.05$ and draw δ from a Gaussian with dispersion 0.34 dex. The shape of the BHMF, particularly at the massive end, is driven strongly by the size of this intrinsic scatter. Upward scatter from the much more numerous moderate-mass galaxies can increase the abundance of the rarest black holes more than downward scatter removes objects from the tail [73, 162, 165]. The BHMF is then estimated with the same galaxy-selection weights as the GSMF,

$$\Phi(M_{\rm BH})\,\Delta \log_{10} M_{\rm BH} = \sum_i \frac{1}{V_{{\rm max},i}}, \tag{5.15}$$

but now the sum is over galaxies whose seeded black hole masses fall in the corresponding $M_{\rm BH}$ bin. The vertical completeness marker in Figure 5.9 maps the stellar-mass completeness limit at $z_{\rm max} = 0.1$, $\log_{10} M_{*,\rm lim}/M_\odot = 10.08$, through the mean McConnell and Ma [118] relation, giving $\log_{10} M_{\rm BH,lim}/M_\odot = 7.50$.

Figure 5.9 shows the resulting BHMF for the ODR-corrected stellar masses with intrinsic scatter included. Between 10^7 and $10^8 M_\odot$, the catalog BHMF is below the Liepold and Ma [106] curve by a median of $\sim$0.21 dex, reflecting the same low-mass incompleteness visible in the GSMF. Between 10^8 and $10^{10} M_\odot$, the catalog lies above the Liepold and Ma [106] BHMF by $\sim$0.25–0.29 dex. This is the BHMF counterpart of the intermediate-mass GSMF excess and is amplified by the intrinsic scatter in the black-hole–host relation. At the highest plotted masses, 10^{10}–$10^{10.7} M_\odot$, the median offset is small, ~ -0.09 dex, and the curve falls rapidly with only a few high-weight objects contributing. The agreement at the extreme high-mass end depends on the assumed $f_{\rm bulge} = 1$, the adopted scaling relation, the scatter prescription, and photometric-redshift errors in the most luminous galaxies. Nevertheless, the exercise shows that the catalog produces a plausible high-mass BHMF when placed on the ODR-corrected stellar-mass scale, while also exposing the systematic sensitivity of the inferred SMBH abundance to the stellar-mass calibration.

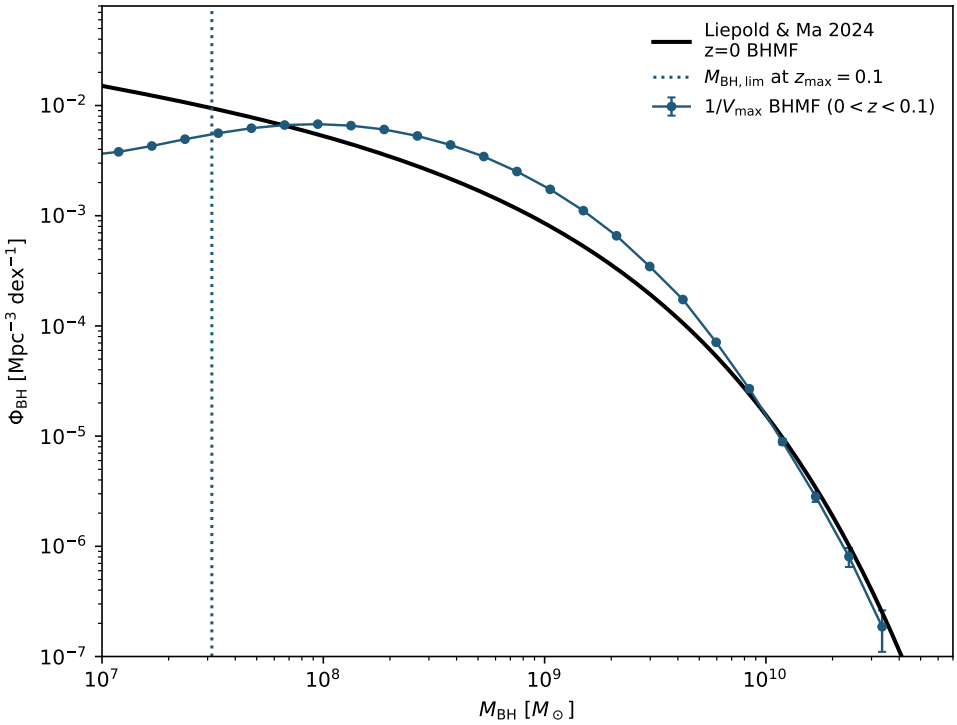

Figure 5.9: Black hole mass function inferred from the WSCOS+2MPZ stellar-mass catalog for $0 < z < 0.1$. The blue points use ODR-corrected clipped Cluver et al. [38] stellar masses, $f_{\rm bulge} = 1$, the mean McConnell and Ma [118] $M_{\rm BH}$–$M_{\rm bulge}$ relation, and 0.34 dex intrinsic scatter. The same WISE-based $1/V_{\rm max}$ weights and stellar-mass completeness cut used for the GSMF are applied before seeding black holes. The vertical dotted line marks the stellar-mass completeness limit at $z_{\rm max} = 0.1$ mapped through the mean $M_{\rm BH}$–$M_{\rm bulge}$ relation. The black curve shows the $z = 0$ BHMF from Liepold and Ma [106], derived from their Leja+MASSIVE GSMF and a black-hole–galaxy scaling relation.

5.6 Discussion

This chapter presents a PTA host-galaxy catalog built from WSCOS and 2MPZ. The catalog combines broad sky coverage, a large low-redshift sample, and WISE $W1/W2$ photometry. The WISE photometry is converted to stellar mass using a rest-frame $W1$ luminosity, a $W1-W2$ color-based mass-to-light ratio, and redshift-dependent k-corrections. The resulting catalog contains approximately 19.6 million galaxies and can be used for both local SMBH demographic studies and PTA host-galaxy filtering.

The comparison to K-band stellar masses provides the main internal check on the stellar-mass scale. For the subset of 927,524 galaxies with usable 2MPZ K-band photometry, the WISE- and K-band estimates show a mass-dependent offset, with WISE-based masses lower

at the high-mass end. Similar behavior has been seen in recent comparisons of infrared stellar-mass estimators, where WISE-based methods can underpredict the masses of massive galaxies relative to GAMA reference values [129]. We therefore apply an empirical correction to place the WISE-based catalog on a scale closer to the K-band estimates. This correction improves internal consistency while retaining the advantages of the WISE-based estimator for the full all-sky sample.

The GSMF and BHMF provide two population-level applications of the catalog. The GSMF is constructed with a $1/V_{\rm max}$ estimator using the parent-catalog selection functions and compared to published local GSMFs. Black hole masses are then seeded using a black hole–bulge mass relation with intrinsic scatter. Relevant sources of uncertainty include photometric redshifts, stellar mass-to-light calibration, possible IMF variation, bulge fraction, black hole scaling relation choice, and intrinsic scatter. These quantities are central to any use of the catalog in ranking candidate PTA hosts.

5.7 Summary

In this chapter, we constructed a low-redshift all-sky galaxy catalog for PTA applications by combining WSCOS and 2MPZ. The parent catalogs provide complementary magnitude ranges and WISE $W1/W2$ photometry, allowing stellar masses to be estimated for nearly 20 million galaxies. We applied WISE k-corrections, adopted a color-based WISE mass-to-light calibration, compared the resulting masses to an independent K-band mass scale, and used the overlap sample to define an empirical correction to the WISE-based stellar masses. We then constructed a GSMF with a $1/V_{\rm max}$ estimator and inferred a BHMF by assigning black hole masses from a black hole–bulge mass relation with intrinsic scatter. The catalog provides the core ingredients needed for PTA host-galaxy filtering, including sky position, redshift, stellar mass, and inferred SMBH mass for a large all-sky galaxy sample.

Appendix

5.A Notation

Table 5.2: Summary of selected notation used in this chapter.

Symbol	Definition
Photometric quantities	
m_{W1}	Observed apparent WISE $W1$ magnitude, on the Vega system and corrected for Galactic extinction in the parent catalogs.
m_{W2}	Observed apparent WISE $W2$ magnitude, on the Vega system and corrected for Galactic extinction in the parent catalogs.
$M_{3.4\mu\mathrm{m}}$	Rest-frame absolute $3.4\,\mu$m magnitude used to compute the WISE $W1$ luminosity.
$m_{3.4\mu\mathrm{m}} - m_{4.6\mu\mathrm{m}}$	Rest-frame WISE color used in the color-based mass-to-light calibration.
m_K	Observed apparent 2MASS K-band magnitude, on the Vega system and corrected for Galactic extinction.
$M_{2.2\mu\mathrm{m}}$	Rest-frame absolute $2.2\,\mu$m magnitude used in the K-band stellar-mass calibration.
Stellar-mass estimates	
M_*^{WISE}	Stellar mass inferred from WISE photometry using the adopted Cluver et al. [38] color–M_*/L calibration.
$M_*^{\mathrm{WISE,corr}}$	ODR-corrected WISE stellar mass placed on the K-band reference scale.
M_*^K	Stellar mass inferred from 2MASS K-band photometry using the piecewise calibration in Equation 5.7.
$\Delta \log_{10} M_*$	Difference between the K-band and WISE stellar-mass estimates, defined as $\log_{10} M_*^K - \log_{10} M_*^{\mathrm{WISE}}$.
k-corrections and distances	
$\mu(z)$	Distance modulus, $\mu(z) = 25 + 5\log_{10} d_L(z)$ for luminosity distance d_L in Mpc.
$\mathcal{C}_{W1}(z)$	WISE $W1$ k-correction used to convert observed m_{W1} to rest-frame $3.4\,\mu$m absolute magnitude.
$\mathcal{C}_{W1-W2}(z)$	WISE color k-correction used to map observed $m_{W1} - m_{W2}$ to rest-frame $m_{3.4\mu\mathrm{m}} - m_{4.6\mu\mathrm{m}}$.
$\mathcal{C}_K(z)$	K-band k-correction applied to the observed 2MASS K-band magnitude.
GSMF quantities	
$W1_{\mathrm{lim}}(z)$	Effective WISE $W1$ faint limit used in the $1/V_{\mathrm{max}}$ GSMF calculation.
$M_{\mathrm{lim}}(z)$	Stellar-mass completeness limit estimated with the Pozzetti et al. [136]-style limiting-mass method.
$V_{\mathrm{max},i}$	Maximum accessible comoving volume for galaxy i in the GSMF calculation.
f_Ω	Sky fraction used in the accessible-volume calculation. The fiducial value is $f_\Omega = 0.70$.
BHMF quantities	
M_{bulge}	Bulge stellar mass used in the black hole–host-galaxy scaling relation.
f_{bulge}	Bulge fraction, defined through $M_{\mathrm{bulge}} = f_{\mathrm{bulge}} M_*$.
δ	Random deviate representing the intrinsic scatter in the adopted black hole–bulge mass relation.

Chapter 6

Conclusion and Future Directions

This dissertation has explored two closely related problems in supermassive black hole astrophysics. The first is the measurement of black hole masses in individual massive galaxies, where the stellar motions must be interpreted through dynamical models that are flexible enough to represent the intrinsic structure of the galaxy. The second is the extension of these measurements to the broader galaxy population, where direct dynamical measurements are currently available for only a small number of systems and empirical estimates remain important for galaxy evolution and gravitational-wave astrophysics. Together, the chapters of this dissertation focus on connecting photometric and spectroscopic observations to the masses, shapes, and demographics of massive galaxies and their central black holes.

Chapter 1 introduced the observational and dynamical framework used throughout the dissertation. It reviewed the empirical connection between supermassive black holes and their host galaxies, the photometric modeling needed to represent the stellar mass distribution, the spectroscopic measurements used to recover stellar kinematics, and the sequence of dynamical methods that connect these observables to a gravitational potential. This background motivated the use of orbit-based Schwarzschild models, particularly in the triaxial regime, as the main tool for measuring black hole masses and intrinsic galaxy shapes in the following chapters.

Chapter 2 presented a triaxial Schwarzschild modeling analysis of NGC 2693, a nearby massive early-type galaxy in the MASSIVE survey. Using HST photometry and integral-field stellar kinematics extending from the central few hundred parsecs to large galactocentric radius, this chapter measured the central black hole mass, stellar mass-to-light ratio, dark matter halo, orbital structure, and intrinsic shape of the galaxy. The best-fit triaxial model gives $M_{\rm BH} = (1.7 \pm 0.4) \times 10^9\, M_\odot$ and shows that NGC 2693 is intrinsically triaxial despite its nearly axisymmetric projected appearance. Axisymmetric Schwarzschild and JAM models prefer larger black hole masses, although the results remain broadly consistent within the uncertainties. The comparison highlights the importance of allowing triaxial structure when interpreting stellar kinematics in massive galaxies.

Chapter 3 used mock observations to test the robustness of the *TriOS* triaxial Schwarzschild code. The chapter constructed realistic synthetic photometric and kinematic data sets with

known input masses and intrinsic shapes, then modeled these data using the same six-dimensional parameter searches applied to real galaxies. These tests show that the code can recover black hole mass, stellar mass-to-light ratio, dark matter content, and intrinsic shape without adding an explicit model-complexity penalty to the fitting procedure. The recovery of the mock galaxies provides an important validation step for the use of triaxial orbit modeling in the high-mass regime, where systematic modeling assumptions can be difficult to assess from real observations alone.

Chapter 4 applied triaxial Schwarzschild modeling to NGC 315, a giant radio galaxy with an existing black hole mass measurement from molecular gas dynamics. The stellar dynamical models use spatially resolved stellar kinematics and photometry to measure the black hole mass, stellar mass-to-light ratio, dark matter halo, and intrinsic shape. The best-fit models find $M_{\rm BH} = (3.0 \pm 0.3) \times 10^9\, M_\odot$ and indicate that NGC 315 is intrinsically triaxial and highly prolate. Because NGC 315 has both stellar- and gas-dynamical black hole mass measurements, it provides a valuable comparison between two independent techniques. In the small current sample of galaxies with both types of measurements, the stellar- and gas-dynamical masses show no statistically significant systematic offset.

Chapter 5 moved from detailed modeling of individual galaxies to population-level black hole mass estimates. This chapter constructed a large low-redshift galaxy catalog by combining WISExSuperCOSMOS and 2MPZ, estimating stellar masses from WISE photometry, and developing the framework for assigning black hole masses through empirical scaling relations. The current catalog contains approximately 19.6 million galaxies and is designed to support studies of the local black hole mass function as well as searches for host galaxies of nanohertz gravitational-wave sources. This work connects the direct dynamical measurements emphasized in the earlier chapters to the much larger galaxy samples needed for gravitational-wave follow-up.

The results of this dissertation add to a growing body of evidence that the most massive nearby galaxies often require models beyond simple axisymmetry. In NGC 2693 and NGC 315, the projected photometry alone does not fully convey the intrinsic three-dimensional structure inferred from the stellar dynamics. The mock tests show that this additional freedom can be constrained in controlled experiments, while the galaxy applications show that it can affect the interpretation of real black hole mass measurements. These results suggest that triaxial orbit modeling will remain important for calibrating the high-mass end of black hole–host-galaxy scaling relations, where the number of secure measurements is still limited and where systematic effects have an outsized impact on inferred trends.

Looking forward, the most useful progress will come from combining more direct black hole mass measurements with larger and more homogeneous galaxy catalogs. Improved integral-field spectroscopy, adaptive optics, and high-resolution observations from facilities such as JWST, ALMA, and future extremely large telescopes will make it possible to model the centers of more massive galaxies with the spatial resolution needed for robust black hole measurements. At the same time, all-sky photometric catalogs and empirical scaling relations will become increasingly important as pulsar timing arrays move toward identifying and localizing individual supermassive black hole binary candidates. The direct dynamical

measurements provide the calibration and physical interpretation, while the catalog-scale work provides the statistical reach needed for gravitational-wave applications. The long-term goal is a black hole census that is both dynamically grounded and large enough to connect individual galaxies, galaxy assembly, and the emerging low-frequency gravitational-wave sky.

Bibliography

[1] Gabriella Agazie et al. "The NANOGrav 15 yr Data Set: Evidence for a Gravitational-wave Background". In: *The Astrophysical Journal* 951 (July 2023), p. L8. DOI: 10.3847/2041-8213/acdac6.

[2] Gabriella Agazie et al. "The NANOGrav 15-year Data Set: Bayesian Limits on Gravitational Waves from Individual Supermassive Black Hole Binaries". In: *The Astrophysical Journal Letters* 951 (July 2023), p. L50. DOI: 10.3847/2041-8213/ace18a. arXiv: 2306.16222 [astro-ph, physics:gr-qc].

[3] Hirotugu Akaike. "Information theory as an extension of the maximum likelihood principle–In: Second International Symposium on Information Theory (Eds) BN Petrov, F". In: *Csaki. BNPBF Csaki Budapest: Academiai Kiado* (1973).

[4] Rene Andrae, Tim Schulze-Hartung, and Peter Melchior. "Dos and don'ts of reduced chi-squared". In: *arXiv e-prints*, arXiv:1012.3754 (Dec. 2010), arXiv:1012.3754. arXiv: 1012.3754 [astro-ph.IM].

[5] A. J. Barth, L. C. Ho, and W. L. W. Sargent. "A Study of the Direct Fitting Method for Measurement of Galaxy Velocity Dispersions". In: *AJ* 124 (Nov. 2002), pp. 2607–2614. DOI: 10.1086/343840. eprint: astro-ph/0209564.

[6] Aaron J. Barth et al. "MEASUREMENT OF THE BLACK HOLE MASS IN NGC 1332 FROM ALMA OBSERVATIONS AT 0.044 ARCSECOND RESOLUTION". In: *The Astrophysical Journal Letters* 822 (May 2016), p. L28. DOI: 10.3847/2041-8205/822/2/L28.

[7] M. C. Begelman, R. D. Blandford, and M. J. Rees. "Massive black hole binaries in active galactic nuclei". In: *Nature* 287 (Sept. 1980), pp. 307–309. DOI: 10.1038/287307a0.

[8] E. F. Bell et al. "The Optical and Near-Infrared Properties of Galaxies. I. Luminosity and Stellar Mass Functions". In: *ApJS* 149 (Dec. 2003), pp. 289–312. DOI: 10.1086/378847. eprint: arXiv:astro-ph/0302543.

[9] Yassine Ben Zineb, Feryal Ozel, and Dimitrios Psaltis. Dec. 2024. DOI: 10.48550/arXiv.2412.01904.

[10] R. Bender. "Unraveling the kinematics of early-type galaxies. Presentation of a new method and its application to NGC 4621." In: 229 (Mar. 1990), pp. 441–451.

[11] R. Bender, R. P. Saglia, and O. E. Gerhard. "Line-of-Sight Velocity Distributions of Elliptical Galaxies". In: *MNRAS* 269 (Aug. 1994), p. 785. DOI: 10.1093/mnras/269.3.785.

[12] Maciej Bilicki et al. "Two Micron All Sky Survey Photometric Redshift Catalog: A Comprehensive Three-dimensional Census of the Whole Sky". In: *ApJS* 210, 9 (Jan. 2014), p. 9. DOI: 10.1088/0067-0049/210/1/9. arXiv: 1311.5246 [astro-ph.CO].

[13] Maciej Bilicki et al. "WISE × SuperCOSMOS Photometric Redshift Catalog: 20 Million Galaxies over 3/pi Steradians". In: *ApJS* 225, 5 (July 2016), p. 5. DOI: 10.3847/0067-0049/225/1/5. arXiv: 1607.01182 [astro-ph.CO].

[14] J Binney and G de Vaucouleurs. "The apparent and true ellipticities of galaxies of different Hubble types in the Second Reference Catalogue". In: *Monthly Notices of the Royal Astronomical Society* 194 (1981), pp. 679–691.

[15] James Binney. "Testing for triaxiality with kinematic data". In: *MNRAS* 212 (Feb. 1985), pp. 767–781. DOI: 10.1093/mnras/212.4.767.

[16] James Binney and Scott Tremaine. *Galactic Dynamics*. 2nd ed. Princeton, NJ: Princeton University Press, 2008.

[17] John P. Blakeslee et al. "The Hubble Constant from Infrared Surface Brightness Fluctuation Distances". In: *ApJ* 911, 65 (Apr. 2021), p. 65. DOI: 10.3847/1538-4357/abe86a. arXiv: 2101.02221 [astro-ph.CO].

[18] Benjamin D. Boizelle et al. "A Precision Measurement of the Mass of the Black Hole in NGC 3258 from High-resolution ALMA Observations of Its Circumnuclear Disk". In: *The Astrophysical Journal* 881 (Aug. 2019), p. 10. DOI: 10.3847/1538-4357/ab2a0a.

[19] Benjamin D. Boizelle et al. "Black Hole Mass Measurements of Radio Galaxies NGC 315 and NGC 4261 Using ALMA CO Observations*". In: *The Astrophysical Journal* 908 (Feb. 2021), p. 19. DOI: 10.3847/1538-4357/abd24d.

[20] Mohamed Amine Bouhlel et al. "A Python surrogate modeling framework with derivatives". In: *Advances in Engineering Software* (2019), p. 102662. DOI: https://doi.org/10.1016/j.advengsoft.2019.03.005.

[21] Jo Bovy. *Dynamics and Astrophysics of Galaxies*.

[22] Maarten A. Breddels et al. "Orbit-based dynamical models of the Sculptor dSph galaxy". In: *Monthly Notices of the Royal Astronomical Society* 433 (July 2013), pp. 3173–3189. DOI: 10.1093/mnras/stt956.

[23] Mark den Brok et al. "Dynamical modelling of the twisted galaxy PGC 046832". In: *Monthly Notices of the Royal Astronomical Society* 508 (Sept. 2021), pp. 4786–4805. DOI: 10.1093/mnras/stab2852.

[24] Sarah Brough et al. "The SAMI Galaxy Survey: Mass as the Driver of the Kinematic Morphology-Density Relation in Clusters". In: *ApJ* 844, 59 (July 2017), p. 59. DOI: 10.3847/1538-4357/aa7a11. arXiv: 1704.01169 [astro-ph.GA].

[25] M. Cappellari. "Effect of Environment on Galaxies' Mass-Size Distribution: Unveiling the Transition from outside-in to inside-out Evolution". In: *ApJ* 778, L2 (Nov. 2013), p. L2. DOI: 10.1088/2041-8205/778/1/L2. arXiv: 1309.1136 [astro-ph.CO].

[26] M. Cappellari. "Measuring the inclination and mass-to-light ratio of axisymmetric galaxies via anisotropic Jeans models of stellar kinematics". In: *MNRAS* 390 (Oct. 2008), pp. 71–86. DOI: 10.1111/j.1365-2966.2008.13754.x. arXiv: 0806.0042.

[27] M. Cappellari and Y. Copin. "Adaptive spatial binning of integral-field spectroscopic data using Voronoi tessellations". In: *MNRAS* 342 (June 2003), pp. 345–354. DOI: 10.1046/j.1365-8711.2003.06541.x. eprint: astro-ph/0302262.

[28] M. Cappellari and E. Emsellem. "Parametric Recovery of Line-of-Sight Velocity Distributions from Absorption-Line Spectra of Galaxies via Penalized Likelihood". In: *PASP* 116 (Feb. 2004), pp. 138–147. DOI: 10.1086/381875. eprint: arXiv:astro-ph/0312201.

[29] M. Cappellari et al. "The ATLAS^{3D} project - XV. Benchmark for early-type galaxies scaling relations from 260 dynamical models: mass-to-light ratio, dark matter, Fundamental Plane and Mass Plane". In: *MNRAS* 432 (July 2013), pp. 1709–1741. DOI: 10.1093/mnras/stt562. arXiv: 1208.3522 [astro-ph.CO].

[30] Michele Cappellari. "Efficient multi-Gaussian expansion of galaxies". In: *MNRAS* 333 (2002), pp. 400–410. DOI: 10.1046/j.1365-8711.2002.05412.x.

[31] Michele Cappellari. "Efficient solution of the anisotropic spherically aligned axisymmetric Jeans equations of stellar hydrodynamics for galactic dynamics". In: *MNRAS* 494 (June 2020), pp. 4819–4837. DOI: 10.1093/mnras/staa959. arXiv: 1907.09894 [astro-ph.GA].

[32] Michele Cappellari. "Improving the full spectrum fitting method: accurate convolution with Gauss-Hermite functions". In: *MNRAS* 466 (Apr. 2017), pp. 798–811. DOI: 10.1093/mnras/stw3020. arXiv: 1607.08538 [astro-ph.GA].

[33] Michele Cappellari. "Measuring the inclination and mass-to-light ratio of axisymmetric galaxies via anisotropic Jeans models of stellar kinematics". In: *MNRAS* 390 (Oct. 2008), pp. 71–86. DOI: 10.1111/j.1365-2966.2008.13754.x. arXiv: 0806.0042 [astro-ph].

[34] Michele Cappellari et al. "Systematic variation of the stellar initial mass function in early-type galaxies". In: *Nature* 484 (Apr. 2012), pp. 485–488. DOI: 10.1038/nature10972. arXiv: 1202.3308 [astro-ph.CO].

[35] Jason A. Cardelli, Geoffrey C. Clayton, and John S. Mathis. "The Relationship between Infrared, Optical, and Ultraviolet Extinction". In: *ApJ* 345 (Oct. 1989), p. 245. DOI: 10.1086/167900.

[36] A. J. Cenarro et al. "Empirical calibration of the near-infrared Ca ii triplet - I. The stellar library and index definition". In: *MNRAS* 326 (Sept. 2001), pp. 959–980. DOI: 10.1046/j.1365-8711.2001.04688.x. eprint: astro-ph/0109157.

[37] Igor V. Chilingarian, Anne-Laure Melchior, and Ivan Yu. Zolotukhin. "Analytical approximations of K-corrections in optical and near-infrared bands". In: *MNRAS* 405 (July 2010), pp. 1409–1420. DOI: 10.1111/j.1365-2966.2010.16506.x. arXiv: 1002.2360 [astro-ph.CO].

[38] M. E. Cluver et al. "Galaxy and Mass Assembly (GAMA): Mid-infrared Properties and Empirical Relations from WISE". In: *ApJ* 782, 90 (Feb. 2014), p. 90. DOI: 10.1088/0004-637X/782/2/90. arXiv: 1401.0837 [astro-ph.GA].

[39] Charlie Conroy and Pieter van Dokkum. "The Stellar Initial Mass Function in Early-Type Galaxies From Absorption Line Spectroscopy. II. Results". In: *The Astrophysical Journal* 760 (Nov. 2012), p. 71. DOI: 10.1088/0004-637X/760/1/71. arXiv: 1205.6473 [astro-ph.CO].

[40] N. Cretton and E. Emsellem. "On the reliability of the black hole mass and mass-to-light ratio determinations with Schwarzschild models". In: *Monthly Notices of the Royal Astronomical Society* 347 (Jan. 2004), pp. L31–L35. DOI: 10.1111/j.1365-2966.2004.07374.x.

[41] N. Cretton et al. "Axisymmetric Three-Integral Models for Galaxies". In: *ApJS* 124 (Oct. 1999), pp. 383–401. DOI: 10.1086/313264. arXiv: astro-ph/9902034 [astro-ph].

[42] A. C. Crook et al. "Groups of Galaxies in the Two Micron All Sky Redshift Survey". In: *ApJ* 655 (Feb. 2007), pp. 790–813. DOI: 10.1086/510201. eprint: arXiv:astro-ph/0610732.

[43] Jared R. Davidson et al. "Circumnuclear Dust in Luminous Early-type Galaxies. I. Sample Properties and Stellar Luminosity Models". In: *The Astrophysical Journal* 972 (Sept. 2024), p. 127. DOI: 10.3847/1538-4357/ad5be4.

[44] Timothy A. Davis et al. "WISDOM Project – II. Molecular gas measurement of the supermassive black hole mass in NGC 4697". In: *Monthly Notices of the Royal Astronomical Society* 468 (July 2017), pp. 4675–4690. DOI: 10.1093/mnras/stw3217.

[45] De Francesco, G., Capetti, A., and Marconi, A. "Measuring supermassive black holes with gas kinematics: the active S0 galaxy NGC 3998". In: *A&A* 460 (2006), pp. 439–448. DOI: 10.1051/0004-6361:20065826.

[46] S. Djorgovski and M. Davis. "Fundamental properties of elliptical galaxies". In: *ApJ* 313 (Feb. 1987), pp. 59–68. DOI: 10.1086/164948.

[47] Pandora Dominiak et al. *WISDOM Project – XXIV. Cross-checking supermassive black hole mass estimates from ALMA CO gas kinematics and SINFONI stellar kinematics in the galaxy NGC 4751*. Apr. 2024. DOI: 10.48550/arXiv.2404.11260. arXiv: 2404.11260 [astro-ph].

[48] Francis Duey et al. "The Baryonic Tully Fisher Relation. II. Stellar Mass Models". In: *AJ* 169, 186 (Mar. 2025), p. 186. DOI: 10.3847/1538-3881/adaf21. arXiv: 2501.10919 [astro-ph.GA].

[49] Bililign T. Dullo and Alister W. Graham. "Depleted cores, multicomponent fits, and structural parameter relations for luminous early-type galaxies". In: *Monthly Notices of the Royal Astronomical Society* 444 (Nov. 2014), pp. 2700–2722. DOI: 10.1093/mnras/stu1590.

[50] E. Emsellem et al. "The ATLAS^{3D} project - III. A census of the stellar angular momentum within the effective radius of early-type galaxies: unveiling the distribution of fast and slow rotators". In: *MNRAS* 414 (June 2011), pp. 888–912. DOI: 10.1111/j.1365-2966.2011.18496.x. arXiv: 1102.4444 [astro-ph.CO].

[51] I. Ene et al. "The MASSIVE Survey XIII. Spatially Resolved Stellar Kinematics in the Central 1 kpc of 20 Massive Elliptical Galaxies with the GMOS-North Integral Field Spectrograph". In: *ApJ* 878, 57 (June 2019), p. 57. DOI: 10.3847/1538-4357/ab1f04. arXiv: 1904.08929.

[52] Irina Ene et al. "The MASSIVE Survey X. Misalignment between kinematic and photometric axes and intrinsic shapes of massive early-type galaxies". In: *MNRAS* 479 (2018), pp. 2810–2826. DOI: 10.1093/mnras/sty1649.

[53] Irina Ene et al. "The MASSIVE Survey XIV—Stellar Velocity Profiles and Kinematic Misalignments from 200 pc to 20 kpc in Massive Early-type Galaxies". In: *ApJ* 891, 65 (Mar. 2020), p. 65. DOI: 10.3847/1538-4357/ab7016. arXiv: 2001.11046 [astro-ph.GA].

[54] Event Horizon Telescope Collaboration et al. "First M87 Event Horizon Telescope Results. I. The Shadow of the Supermassive Black Hole". In: *ApJ* 875, L1 (Apr. 2019), p. L1. DOI: 10.3847/2041-8213/ab0ec7. arXiv: 1906.11238 [astro-ph.GA].

[55] Event Horizon Telescope Collaboration et al. "First sagittarius a* event horizon telescope results. I. The shadow of the supermassive black hole in the center of the milky way". In: 930 (May 2022), p. L12. DOI: 10.3847/2041-8213/ac6674.

[56] S. M. Faber et al. "The Centers of Early-Type Galaxies with HST. IV. Central Parameter Relations." In: *AJ* 114 (Nov. 1997), p. 1771. DOI: 10.1086/118606. eprint: arXiv:astro-ph/9610055.

[57] S. M. Faber and R. E. Jackson. "Velocity dispersions and mass-to-light ratios for elliptical galaxies". In: *ApJ* 204 (Mar. 1976), pp. 668–683. DOI: 10.1086/154215.

[58] J. Falcón-Barroso et al. "An updated MILES stellar library and stellar population models". In: *A&A* 532, A95 (Aug. 2011), A95. DOI: 10.1051/0004-6361/201116842. arXiv: 1107.2303.

[59] B. L. Fanaroff and J. M. Riley. "The morphology of extragalactic radio sources of high and low luminosity". In: *Monthly Notices of the Royal Astronomical Society* 167 (May 1974), 31P–36P. DOI: 10.1093/mnras/167.1.31P.

[60] L. Ferrarese and D. Merritt. "A Fundamental Relation between Supermassive Black Holes and Their Host Galaxies". In: *ApJ* 539 (Aug. 2000), pp. L9–L12. DOI: 10.1086/312838. eprint: astro-ph/0006053.

[61] K. M. Flaherty et al. "A Near- and Mid-Infrared Extinction Law in Indebetouw et al. (2005) and the Spitzer Cores to Disks Legacy Program". In: *ApJ* 663 (July 2007), pp. 1069–1082. DOI: 10.1086/518410. arXiv: 0706.3153 [astro-ph].

[62] C. Foster et al. "The SAMI Galaxy Survey: the intrinsic shape of kinematically selected galaxies". In: *Monthly Notices of the Royal Astronomical Society* 472 (Nov. 2017), pp. 966–978. DOI: 10.1093/mnras/stx1869.

[63] K. Gebhardt et al. "A Relationship between Nuclear Black Hole Mass and Galaxy Velocity Dispersion". In: *ApJ* 539 (Aug. 2000), pp. L13–L16. DOI: 10.1086/312840. eprint: astro-ph/0006289.

[64] K. Gebhardt et al. "Axisymmetric, Three-Integral Models of Galaxies: A Massive Black Hole in NGC 3379". In: *AJ* 119 (Mar. 2000), pp. 1157–1171. DOI: 10.1086/301240. eprint: astro-ph/9912026.

[65] Karl Glazebrook et al. "An imaging K-band survey - II. The redshift survey and galaxy evolution in the infrared". In: *MNRAS* 275 (July 1995), pp. 169–184. DOI: 10.1093/mnras/275.1.169.

[66] S. Gonzaga et al. *The DrizzlePac Handbook*. http://drizzlepac.stsci.edu. 2012.

[67] A. D. Goulding et al. "The MASSIVE Survey. IV. The X-ray Halos of the Most Massive Early-type Galaxies in the Nearby Universe". In: *ApJ* 826, 167 (Aug. 2016), p. 167. DOI: 10.3847/0004-637X/826/2/167. arXiv: 1604.01764.

[68] Charles F. Goullaud et al. "The MASSIVE Survey. IX. Photometric Analysis of 35 High-mass Early-type Galaxies with HST WFC3/IR". In: *ApJ* 856, 11 (Mar. 2018), p. 11. DOI: 10.3847/1538-4357/aab1f3.

[69] Alister W. Graham. "Core Depletion from Coalescing Supermassive Black Holes". In: *ApJ* 613 (Sept. 2004), pp. L33–L36. DOI: 10.1086/424928. arXiv: astro-ph/0503177 [astro-ph].

[70] Alister W. Graham et al. "A New Empirical Model for the Structural Analysis of Early-Type Galaxies, and A Critical Review of the Nuker Model". In: *AJ* 125 (June 2003), pp. 2951–2963. DOI: 10.1086/375320. arXiv: astro-ph/0306023 [astro-ph].

[71] Mark T. Graham et al. "SDSS-IV MaNGA: stellar angular momentum of about 2300 galaxies: unveiling the bimodality of massive galaxy properties". In: *MNRAS* 477 (July 2018), pp. 4711–4737. DOI: 10.1093/mnras/sty504. arXiv: 1802.08213 [astro-ph.GA].

[72] Meng Gu et al. "The MASSIVE Survey. XVI. The Stellar Initial Mass Function in the Center of MASSIVE Early-Type Galaxies". In: *The Astrophysical Journal* 932 (June 2022), p. 103. DOI: 10.3847/1538-4357/ac69ea. arXiv: 2110.11985 [astro-ph.GA].

[73] K. Gültekin et al. "The M-σ and M-L Relations in Galactic Bulges, and Determinations of Their Intrinsic Scatter". In: *ApJ* 698 (June 2009), pp. 198–221. DOI: 10.1088/0004-637X/698/1/198. arXiv: 0903.4897 [astro-ph.GA].

[74] N. C. Hambly et al. "The SuperCOSMOS Sky Survey - I. Introduction and description". In: *MNRAS* 326 (Oct. 2001), pp. 1279–1294. DOI: 10.1046/j.1365-8711.2001.04660.x.

[75] N. Häring and H.-W. Rix. "On the Black Hole Mass-Bulge Mass Relation". In: *ApJ* 604 (Apr. 2004), pp. L89–L92. DOI: 10.1086/383567. eprint: astro-ph/0402376.

[76] G. J. Hill et al. "Design, construction, and performance of VIRUS-P: the prototype of a highly replicated integral-field spectrograph for HET". In: *Society of Photo-Optical Instrumentation Engineers (SPIE) Conference Series*. Vol. 7014. Society of Photo-Optical Instrumentation Engineers (SPIE) Conference Series. Aug. 2008. DOI: 10.1117/12.790235.

[77] I. M. Hook et al. "The Gemini-North Multi-Object Spectrograph: Performance in Imaging, Long-Slit, and Multi-Object Spectroscopic Modes". In: *PASP* 116 (May 2004), pp. 425–440. DOI: 10.1086/383624.

[78] R. C. W. Houghton et al. "The central kinematics of NGC 1399 measured with 14 pc resolution". In: *MNRAS* 367 (Mar. 2006), pp. 2–18. DOI: 10.1111/j.1365-2966.2005.09713.x. arXiv: astro-ph/0510278 [astro-ph].

[79] J. P. Huchra et al. "The 2MASS Redshift Survey-Description and Data Release". In: *ApJS* 199, 26 (Apr. 2012), p. 26. DOI: 10.1088/0067-0049/199/2/26. arXiv: 1108.0669 [astro-ph.CO].

[80] R. Indebetouw et al. "The Wavelength Dependence of Interstellar Extinction from 1.25 to 8.0 Microns Using GLIMPSE Data". In: *ApJ* 619 (Feb. 2005), pp. 931–938. DOI: 10.1086/426679. arXiv: astro-ph/0406403.

[81] T. H. Jarrett et al. "2MASS Extended Source Catalog: Overview and Algorithms". In: *AJ* 119 (May 2000), pp. 2498–2531. DOI: 10.1086/301330.

[82] T. H. Jarrett et al. "A New Wide-field Infrared Survey Explorer Calibration of Stellar Mass". In: *ApJ* 946, 95 (Apr. 2023), p. 95. DOI: 10.3847/1538-4357/acb68f. arXiv: 2301.05952 [astro-ph.GA].

[83] T. H. Jarrett et al. "Extending the Nearby Galaxy Heritage with WISE: First Results from the WISE Enhanced Resolution Galaxy Atlas". In: *AJ* 145, 6 (Jan. 2013), p. 6. DOI: 10.1088/0004-6256/145/1/6.

[84] Joseph B. Jensen et al. "Infrared Surface Brightness Fluctuation Distances for MASSIVE and Type Ia Supernova Host Galaxies". In: *ApJS* 255, 21 (Aug. 2021), p. 21. DOI: 10.3847/1538-4365/ac01e7. arXiv: 2105.08299 [astro-ph.CO].

[85] Ruichen Jin, Wei Chen, and Agus Sudjianto. "An efficient algorithm for constructing optimal design of computer experiments". In: *Journal of Statistical Planning and Inference* 134 (2005), pp. 268–287. DOI: https://doi.org/10.1016/j.jspi.2004.02.014.

[86] Yunpeng Jin et al. "Evaluating the ability of triaxial Schwarzschild modelling to estimate properties of galaxies from the Illustris simulation". In: *MNRAS* 486 (July 2019), pp. 4753–4772. DOI: 10.1093/mnras/stz1170. arXiv: 1904.12942 [astro-ph.GA].

[87] Michael D. Johnson et al. "The Black Hole Explorer: motivation and vision". In: *Space Telescopes and Instrumentation 2024: Optical, Infrared, and Millimeter Wave*. Vol. 13092. SPIE, Aug. 2024, pp. 821–872. DOI: 10.1117/12.3019835.

[88] Kyle M. Kabasares et al. "Black Hole Mass Measurements of Early-type Galaxies NGC 1380 and NGC 6861 through ALMA and HST Observations and Gas-dynamical Modeling". In: *The Astrophysical Journal* 934 (Aug. 2022), p. 162. DOI: 10.3847/1538-4357/ac7a38.

[89] B. C. Kelly. "Some Aspects of Measurement Error in Linear Regression of Astronomical Data". In: *ApJ* 665 (Aug. 2007), pp. 1489–1506. DOI: 10.1086/519947. arXiv: 0705.2774.

[90] T. Kettlety et al. "Galaxy and mass assembly (GAMA): the consistency of GAMA and WISE derived mass-to-light ratios". In: *MNRAS* 473 (Jan. 2018), pp. 776–783. DOI: 10.1093/mnras/stx2379. arXiv: 1709.08316 [astro-ph.GA].

[91] Andrew King. "Black Holes, Galaxy Formation, and the M_{BH}-σ Relation". In: *ApJ* 596 (Oct. 2003), pp. L27–L29. DOI: 10.1086/379143. arXiv: astro-ph/0308342 [astro-ph].

[92] J. Kormendy. "Brightness distributions in compact and normal galaxies. II - Structure parameters of the spheroidal component". In: *ApJ* 218 (Dec. 1977), pp. 333–346. DOI: 10.1086/155687.

[93] J. Kormendy and L. C. Ho. "Coevolution (Or Not) of Supermassive Black Holes and Host Galaxies". In: *ARA&A* 51 (Aug. 2013), pp. 511–653. DOI: 10.1146/annurev-astro-082708-101811. arXiv: 1304.7762 [astro-ph.CO].

[94] Klaudia Kowalczyk, Ewa L. Łokas, and Monica Valluri. "Recovering the mass profile and orbit anisotropy of mock dwarf galaxies with Schwarzschild modelling". In: *Monthly Notices of the Royal Astronomical Society* 470 (June 2017), pp. 3959–3969. DOI: 10.1093/mnras/stx1520.

[95] Davor Krajnović et al. "A quartet of black holes and a missing duo: probing the low end of the M_{BH}-σ relation with the adaptive optics assisted integral-field spectroscopy". In: *MNRAS* 477 (July 2018), pp. 3030–3064. DOI: 10.1093/mnras/sty778. arXiv: 1803.08055 [astro-ph.GA].

[96] Davor Krajnović et al. "Climbing to the top of the galactic mass ladder: evidence for frequent prolate-like rotation among the most massive galaxies". In: *MNRAS* 477 (July 2018), pp. 5327–5337. DOI: 10.1093/mnras/sty1031. arXiv: 1802.02591 [astro-ph.GA].

[97] Davor Krajnović et al. "Determination of masses of the central black holes in NGC 524 and 2549 using laser guide star adaptive optics". In: *MNRAS* 399 (2009), pp. 1839–1857. DOI: 10.1111/j.1365-2966.2009.15415.x.

[98] Davor Krajnović et al. "Dynamical modelling of stars and gas in NGC 2974: determination of mass-to-light ratio, inclination and orbital structure using the Schwarzschild method". In: *MNRAS* 357 (Mar. 2005), pp. 1113–1133. DOI: 10.1111/j.1365-2966.2005.08715.x. arXiv: astro-ph/0412186 [astro-ph].

[99] Davor Krajnović et al. "Formation channels of slowly rotating early-type galaxies". In: *A&A* 635, A129 (Mar. 2020), A129. DOI: 10.1051/0004-6361/201937040. arXiv: 2001.11277 [astro-ph.GA].

[100] Pierre-Yves Lablanche et al. "The ATLAS^{3D} project - XII. Recovery of the mass-to-light ratio of simulated early-type barred galaxies with axisymmetric dynamical models". In: *MNRAS* 424 (Aug. 2012), pp. 1495–1521. DOI: 10.1111/j.1365-2966.2012.21308.x. arXiv: 1206.0291 [astro-ph.CO].

[101] R. A. Laing et al. "Multifrequency observations of the jets in the radio galaxy NGC 315". In: *Monthly Notices of the Royal Astronomical Society* 368 (May 2006), pp. 48–64. DOI: 10.1111/j.1365-2966.2006.10099.x.

[102] Charles L. Lawson and Richard J. Hanson. *Solving Least Squares Problems*. Society for Industrial and Applied Mathematics, 1995. DOI: 10.1137/1.9781611971217.

[103] Joel Leja et al. "A new census of the 0.2 ¡ z ¡ 3.0 universe. I. The stellar mass function". In: 893 (Apr. 2020), p. 111. DOI: 10.3847/1538-4357/ab7e27. arXiv: 1910.04168 [astro-ph.GA].

[104] Hongyu Li et al. "Assessing the Jeans Anisotropic Multi-Gaussian Expansion method with the Illustris simulation". In: *MNRAS* 455 (Feb. 2016), pp. 3680–3692. DOI: 10.1093/mnras/stv2565. arXiv: 1511.00789 [astro-ph.GA].

[105] Christopher M. Liepold et al. "The MASSIVE Survey. XV. A Stellar Dynamical Mass Measurement of the Supermassive Black Hole in Massive Elliptical Galaxy NGC 1453". In: *ApJ* 891, 4 (Mar. 2020), p. 4. DOI: 10.3847/1538-4357/ab6f71. arXiv: 2001.08753 [astro-ph.GA].

[106] Emily R. Liepold and Chung-Pei Ma. "Big Galaxies and Big Black Holes: The Massive Ends of the Local Stellar and Black Hole Mass Functions and the Implications for Nanohertz Gravitational Waves". In: *The Astrophysical Journal* 971 (Aug. 2024), p. L29. DOI: 10.3847/2041-8213/ad66b8.

[107] Emily R. Liepold, Chung-Pei Ma, and Jonelle L. Walsh. "A 22 Billion M⊙ Black Hole in Holmberg 15A with Keck KCWI Spectroscopy and Triaxial Orbit Modeling". In: *The Astrophysical Journal* 980 (Feb. 2025), p. 58. DOI: 10.3847/1538-4357/ada4b0.

[108] Emily R. Liepold, Chung-Pei Ma, and Jonelle L. Walsh. "Keck Integral-field Spectroscopy of M87 Reveals an Intrinsically Triaxial Galaxy and a Revised Black Hole Mass". In: *ApJ* 945, L35 (Mar. 2023), p. L35. DOI: 10.3847/2041-8213/acbbcf. arXiv: 2302.07884 [astro-ph.GA].

[109] Mathias Lipka and Jens Thomas. "A novel approach to optimize the regularization and evaluation of dynamical models using a model selection framework". In: *MNRAS* 504 (July 2021), pp. 4599–4625. DOI: 10.1093/mnras/stab1092. arXiv: 2104.10168 [astro-ph.GA].

[110] Mathias Lipka and Jens Thomas. "A novel approach to optimize the regularization and evaluation of dynamical models using a model selection framework". In: *Monthly Notices of the Royal Astronomical Society* 504 (May 2021), pp. 4599–4625. DOI: 10.1093/mnras/stab1092. arXiv: 2104.10168 [astro-ph.GA].

[111] Will Lockhart and Samuel E Gralla. "How narrow is the M87* ring – II. A new geometric model". In: *Monthly Notices of the Royal Astronomical Society* 517 (Dec. 2022), pp. 2462–2470. DOI: 10.1093/mnras/stac2743.

[112] S. I. Loubser et al. "Diversity in the stellar velocity dispersion profiles of a large sample of brightest cluster galaxies z $\leq$ 0.3". In: *MNRAS* 477 (June 2018), pp. 335–358. DOI: 10.1093/mnras/sty498. arXiv: 1802.07745.

[113] C.-P. Ma et al. "The MASSIVE Survey. I. A Volume-limited Integral-field Spectroscopic Study of the Most Massive Early-type Galaxies within 108 Mpc". In: *ApJ* 795, 158 (Nov. 2014), p. 158. DOI: 10.1088/0004-637X/795/2/158. arXiv: 1407.1054.

[114] J. Magorrian. "Constraining black hole masses from stellar kinematics by summing over all possible distribution functions". In: *Monthly Notices of the Royal Astronomical Society* 373 (Nov. 2006), pp. 425–434. DOI: 10.1111/j.1365-2966.2006.11054.x.

[115] J. Magorrian et al. "The Demography of Massive Dark Objects in Galaxy Centers". In: *AJ* 115 (June 1998), pp. 2285–2305. DOI: 10.1086/300353. eprint: astro-ph/9708072.

[116] A. Marconi and L. K. Hunt. "The Relation between Black Hole Mass, Bulge Mass, and Near-Infrared Luminosity". In: *ApJ* 589 (May 2003), pp. L21–L24. DOI: 10.1086/375804. eprint: astro-ph/0304274.

[117] Roeland P. van der Marel and Marijn Franx. "A new method for the identification of non-Gaussian line profiles in elliptical galaxies". In: *ApJ* 407 (Apr. 1993), p. 525. DOI: 10.1086/172534.

[118] N. J. McConnell and C.-P. Ma. "Revisiting the Scaling Relations of Black Hole Masses and Host Galaxy Properties". In: *ApJ* 764, 184 (Feb. 2013), p. 184. DOI: 10.1088/0004-637X/764/2/184. arXiv: 1211.2816 [astro-ph.CO].

[119] Stacy S. McGaugh and James M. Schombert. "Color-Mass-to-Light-Ratio Relations for Disk Galaxies". In: *AJ* 148, 77 (Nov. 2014), p. 77. DOI: 10.1088/0004-6256/148/5/77. arXiv: 1407.1839 [astro-ph.GA].

[120] M. D. McKay, R. J. Beckman, and W. J. Conover. "A Comparison of Three Methods for Selecting Values of Input Variables in the Analysis of Output from a Computer Code". In: *Technometrics* 21 (1979), pp. 239–245.

[121] M. D. McKay, R. J. Beckman, and W. J. Conover. "A comparison of three methods for selecting values of input variables in the analysis of output from a computer code". In: *Technometrics : a journal of statistics for the physical, chemical, and engineering sciences* 21 (1979), pp. 239–245.

[122] Sharon E. Meidt et al. "Reconstructing the Stellar Mass Distributions of Galaxies Using S^{4}G IRAC 3.6 and 4.5 μm Images. I. Correcting for Contamination by Polycyclic Aromatic Hydrocarbons, Hot Dust, and Intermediate-age Stars". In: *ApJ* 744, 17 (Jan. 2012), p. 17. DOI: 10.1088/0004-637X/744/1/17.

[123] Miloš Milosavljević and David Merritt. "Formation of Galactic Nuclei". In: *ApJ* 563 (Dec. 2001), pp. 34–62. DOI: 10.1086/323830. arXiv: astro-ph/0103350 [astro-ph].

[124] Chiara M. F. Mingarelli et al. "The local nanohertz gravitational-wave landscape from supermassive black hole binaries". In: *Nature Astronomy* 1 (Nov. 2017), pp. 886–892. DOI: 10.1038/s41550-017-0299-6.

[125] Noboru Murata, Shuji Yoshizawa, and Shun-ichi Amari. "Network information criterion-determining the number of hidden units for an artificial neural network model". In: *IEEE transactions on neural networks* 5 (1994), pp. 865–872.

[126] Julio F. Navarro, Carlos S. Frenk, and Simon D. M. White. "The Structure of Cold Dark Matter Halos". In: *The Astrophysical Journal* 462 (May 1996), p. 563. DOI: 10.1086/177173. arXiv: astro-ph/9508025 [astro-ph].

[127] B. Neureiter et al. "Accuracy and precision of triaxial orbit models I: SMBH mass, stellar mass, and dark-matter halo". In: *MNRAS* 519 (Feb. 2023), pp. 2004–2016. DOI: 10.1093/mnras/stac3652. arXiv: 2212.06173 [astro-ph.GA].

[128] Mark A. Norris et al. "Being WISE. I. Validating Stellar Population Models and M_*/L Ratios at 3.4 and 4.6 μm". In: *ApJ* 797, 55 (Dec. 2014), p. 55. DOI: 10.1088/0004-637X/797/1/55. arXiv: 1407.6005 [astro-ph.GA].

[129] M. Pálfi, G. Dálya, and P. Raffai. "Utilizing stellar mass estimates to identify gravitational wave host galaxies". In: *MNRAS* 539 (May 2025), pp. 1879–1893. DOI: 10.1093/mnras/staf537.

[130] C. Y. Peng et al. "Detailed Structural Decomposition of Galaxy Images". In: *AJ* 124 (July 2002), pp. 266–293. DOI: 10.1086/340952. eprint: astro-ph/0204182.

[131] Chien Y. Peng. "How Mergers May Affect the Mass Scaling Relation between Gravitationally Bound Systems". In: *ApJ* 671 (Dec. 2007), pp. 1098–1107. DOI: 10.1086/522774. arXiv: 0704.1860 [astro-ph].

[132] Polina Petrov et al. "Identifying the Host Galaxies of Supermassive Black Hole Binaries Found by Pulsar Timing Arrays". In: *The Astrophysical Journal* 976 (Nov. 2024), p. 129. DOI: 10.3847/1538-4357/ad7b14. arXiv: 2406.04409 [astro-ph.GA].

[133] D. Pfenniger. "The 3D dynamics of barred galaxies". In: *A&A* 134 (May 1984), pp. 373–386.

[134] Jacob Pilawa, Emily R. Liepold, and Chung-Pei Ma. "TriOS Schwarzschild Orbit Modeling: Robustness of Parameter Inference for Masses and Shapes of Triaxial Galaxies with Supermassive Black Holes". In: *The Astrophysical Journal* 966 (May 2024), p. 205. DOI: 10.3847/1538-4357/ad3935.

[135] Jacob D. Pilawa et al. "The MASSIVE Survey. XVII. A Triaxial Orbit-based Determination of the Black Hole Mass and Intrinsic Shape of Elliptical Galaxy NGC 2693". In: *ApJ* 928, 178 (Apr. 2022), p. 178. DOI: 10.3847/1538-4357/ac58fd. arXiv: 2111.13699 [astro-ph.GA].

[136] L. Pozzetti et al. "zCOSMOS - 10k-bright spectroscopic sample. The bimodality in the galaxy stellar mass function: exploring its evolution with redshift". In: 523 (Nov. 2010), A13. DOI: 10.1051/0004-6361/200913020. arXiv: 0907.5416 [astro-ph.CO].

[137] C. Pulsoni et al. "The stellar halos of ETGs in the IllustrisTNG simulations: The photometric and kinematic diversity of galaxies at large radii". In: *A&A* 641, A60 (Sept. 2020), A60. DOI: 10.1051/0004-6361/202038253. arXiv: 2004.13042 [astro-ph.GA].

[138] C. Pulsoni et al. "The stellar halos of ETGs in the IllustrisTNG simulations: The photometric and kinematic diversity of galaxies at large radii". In: *A&A* 641, A60 (Sept. 2020), A60. DOI: 10.1051/0004-6361/202038253. arXiv: 2004.13042 [astro-ph.GA].

[139] Matthew E Quenneville et al. "The MASSIVE survey – XVIII. Deep wide-field K-band photometry and local scaling relations for massive early-type galaxies". In: *Monthly Notices of the Royal Astronomical Society* 527 (Jan. 2024), pp. 249–264. DOI: 10.1093/mnras/stad3137.

[140] Matthew E. Quenneville, Christopher M. Liepold, and Chung-Pei Ma. "Dynamical Modeling of Galaxies and Supermassive Black Holes: Axisymmetry in Triaxial Schwarzschild Orbit Superposition Models". In: *ApJS* 254, 25 (June 2021), p. 25. DOI: 10.3847/1538-4365/abe6a0. arXiv: 2005.00542 [astro-ph.GA].

[141] Matthew E. Quenneville, Christopher M. Liepold, and Chung-Pei Ma. "Triaxial Orbit-based Dynamical Modeling of Galaxies with Supermassive Black Holes and an Application to Massive Elliptical Galaxy NGC 1453". In: *The Astrophysical Journal* 926 (Feb. 2022), p. 30. DOI: 10.3847/1538-4357/ac3e68.

[142] Matthew E. Quenneville, Emily R. Liepold, and Chung-Pei Ma. "Dynamical Modeling of Galaxies and Supermassive Black Holes: Axisymmetry in Triaxial Schwarzschild Orbit Superposition Models". In: *ApJS* 254, 25 (June 2021), p. 25. DOI: 10.3847/1538-4365/abe6a0. arXiv: 2005.00542 [astro-ph.GA].

[143] Matthew E. Quenneville, Emily R. Liepold, and Chung-Pei Ma. "Triaxial Orbit-based Dynamical Modeling of Galaxies with Supermassive Black Holes and an Application to Massive Elliptical Galaxy NGC 1453". In: *ApJ* 926, 30 (Feb. 2022), p. 30. DOI: 10.3847/1538-4357/ac3e68. arXiv: 2111.06904 [astro-ph.GA].

[144] Carl Edward Rasmussen and Christopher K. I. Williams. *Gaussian Processes for Machine Learning (Adaptive Computation and Machine Learning)*. The MIT Press, 2005.

[145] L. Ricci et al. "Exploring the disk-jet connection in NGC 315". In: *Astronomy and Astrophysics* 664 (Aug. 2022), A166. DOI: 10.1051/0004-6361/202243958.

[146] D. O. Richstone and S. Tremaine. "A general method for constructing spherical galaxy models". In: *ApJ* 286 (Nov. 1984), pp. 27–37. DOI: 10.1086/162572.

[147] D. O. Richstone and S. Tremaine. "Dynamical models of M 87 without a central black hole." In: *ApJ* 296 (Sept. 1985), pp. 370–378. DOI: 10.1086/163455.

[148] Hans-Walter Rix et al. "Dynamical Modeling of Velocity Profiles: The Dark Halo around the Elliptical Galaxy NGC 2434". In: *ApJ* 488 (Oct. 1997), pp. 702–719. DOI: 10.1086/304733. arXiv: astro-ph/9702126 [astro-ph].

[149] S. P. Rusli et al. "The central black hole mass of the high-σ but low-bulge-luminosity lenticular galaxy NGC 1332". In: *MNRAS* 410 (Jan. 2011), pp. 1223–1236. DOI: 10.1111/j.1365-2966.2010.17610.x. arXiv: 1009.0515 [astro-ph.CO].

[150] S. P. Rusli et al. "The Influence of Dark Matter Halos on Dynamical Estimates of Black Hole Mass: 10 New Measurements for High-σ Early-type Galaxies". In: *AJ* 146, 45 (Sept. 2013), p. 45. DOI: 10.1088/0004-6256/146/3/45. arXiv: 1306.1124 [astro-ph.CO].

[151] R. P. Saglia et al. "The SINFONI Black Hole Survey: The Black Hole Fundamental Plane Revisited and the Paths of (Co)evolution of Supermassive Black Holes and Bulges". In: *ApJ* 818, 47 (Feb. 2016), p. 47. DOI: 10.3847/0004-637X/818/1/47.

[152] P. Sánchez-Blázquez et al. "Medium-resolution Isaac Newton Telescope library of empirical spectra". In: *MNRAS* 371 (Sept. 2006), pp. 703–718. DOI: 10.1111/j.1365-2966.2006.10699.x. eprint: astro-ph/0607009.

[153] Giulia Santucci et al. "The SAMI Galaxy Survey: The Internal Orbital Structure and Mass Distribution of Passive Galaxies from Triaxial Orbit-superposition Schwarzschild Models". In: *ApJ* 930, 153 (May 2022), p. 153. DOI: 10.3847/1538-4357/ac5bd5. arXiv: 2203.03648 [astro-ph.GA].

[154] E. F. Schlafly and D. P. Finkbeiner. "Measuring Reddening with Sloan Digital Sky Survey Stellar Spectra and Recalibrating SFD". In: *ApJ* 737, 103 (Aug. 2011), p. 103. DOI: 10.1088/0004-637X/737/2/103. arXiv: 1012.4804 [astro-ph.GA].

[155] David J. Schlegel, Douglas P. Finkbeiner, and Marc Davis. "Maps of Dust Infrared Emission for Use in Estimation of Reddening and Cosmic Microwave Background Radiation Foregrounds". In: *ApJ* 500 (June 1998), pp. 525–553. DOI: 10.1086/305772. arXiv: astro-ph/9710327.

[156] A. Schulze and K. Gebhardt. "Effect of a Dark Matter Halo on the Determination of Black Hole Masses". In: *ApJ* 729, 21 (Mar. 2011), p. 21. DOI: 10.1088/0004-637X/729/1/21. arXiv: 1011.5077 [astro-ph.CO].

[157] Gideon Schwarz. "Estimating the Dimension of a Model". In: *The Annals of Statistics* 6 (1978), pp. 461–464. DOI: 10.1214/aos/1176344136.

[158] M. Schwarzschild. "A numerical model for a triaxial stellar system in dynamical equilibrium". In: *ApJ* 232 (Aug. 1979), pp. 236–247. DOI: 10.1086/157282.

[159] Martin Schwarzschild. "Self-consistent Models for Galactic Halos". In: *ApJ* 409 (June 1993), p. 563. DOI: 10.1086/172687.

[160] J. L. Sérsic. "Influence of the atmospheric and instrumental dispersion on the brightness distribution in a galaxy". In: *Boletin de la Asociacion Argentina de Astronomia La Plata Argentina* 6 (Feb. 1963), pp. 41–43.

[161] Anil C. Seth et al. "A supermassive black hole in an ultra-compact dwarf galaxy". In: *Nature* 513 (Sept. 2014), pp. 398–400. DOI: 10.1038/nature13762. arXiv: 1409.4769 [astro-ph.GA].

[162] F. Shankar et al. "Supermassive black hole demography: the match between the local and accreted mass functions". In: 354 (Nov. 2004), pp. 1020–1030. DOI: 10.1111/j.1365-2966.2004.08261.x. arXiv: astro-ph/0405585 [astro-ph].

[163] Ritei Shibata. "Statistical Aspects of Model Selection". In: *From Data to Model*. Berlin, Heidelberg: Springer Berlin Heidelberg, 1989, pp. 215–240. DOI: 10.1007/978-3-642-75007-6_5.

[164] Joseph Silk and Martin J. Rees. "Quasars and galaxy formation". In: *A&A* 331 (Mar. 1998), pp. L1–L4. arXiv: astro-ph/9801013 [astro-ph].

[165] Joseph Simon and Sarah Burke-Spolaor. "Constraints on Black Hole/Host Galaxy Co-evolution and Binary Stalling Using Pulsar Timing Arrays". In: *The Astrophysical Journal* 826 (July 2016), p. 11. DOI: 10.3847/0004-637X/826/1/11.

[166] Christos Siopis et al. "A STELLAR DYNAMICAL MEASUREMENT OF THE BLACK HOLE MASS IN THE MASER GALAXY NGC 4258". In: *The Astrophysical Journal* 693 (Mar. 2009), pp. 946–969. DOI: 10.1088/0004-637X/693/1/946.

[167] M. F. Skrutskie et al. "The Two Micron All Sky Survey (2MASS)". In: *AJ* 131 (Feb. 2006), pp. 1163–1183. DOI: 10.1086/498708.

[168] Mark D Smith et al. "WISDOM project – IV. A molecular gas dynamical measurement of the supermassive black hole mass in NGC 524". In: *Monthly Notices of the Royal Astronomical Society* 485 (May 2019), pp. 4359–4374. DOI: 10.1093/mnras/stz625.

[169] Russell J. Smith. "Evidence for Initial Mass Function Variation in Massive Early-Type Galaxies". In: *Annual Review of Astronomy and Astrophysics* 58 (Aug. 2020), pp. 577–615. DOI: 10.1146/annurev-astro-032620-020217.

[170] Joshua S. Speagle. "DYNESTY: a dynamic nested sampling package for estimating Bayesian posteriors and evidences". In: *MNRAS* 493 (Apr. 2020), pp. 3132–3158. DOI: 10.1093/mnras/staa278. arXiv: 1904.02180 [astro-ph.IM].

[171] Joshua S. Speagle. "DYNESTY: a dynamic nested sampling package for estimating Bayesian posteriors and evidences". In: *MNRAS* 493 (Apr. 2020), pp. 3132–3158. DOI: 10.1093/mnras/staa278. arXiv: 1904.02180 [astro-ph.IM].

[172] David J. Spiegelhalter et al. "Bayesian measures of model complexity and fit". In: *Journal of the Royal Statistical Society: Series B (Statistical Methodology)* 64 (2002), pp. 583–639. DOI: https://doi.org/10.1111/1467-9868.00353.

[173] David J. Spiegelhalter et al. "Bayesian measures of model complexity and fit". In: *Journal of the Royal Statistical Society: Series B (Statistical Methodology)* 64 (2002), pp. 583–639. DOI: https://doi.org/10.1111/1467-9868.00353.

[174] Sabine Thater et al. "Six new supermassive black hole mass determinations from adaptive-optics assisted SINFONI observations". In: *A&A* 625, A62 (May 2019), A62. DOI: 10.1051/0004-6361/201834808. arXiv: 1902.10175 [astro-ph.GA].

[175] The GRAVITY Collaboration et al. "A geometric distance measurement to the Galactic center black hole with 0.3% uncertainty". In: *Astronomy & Astrophysics* 625 (May 2019), p. L10. DOI: 10.1051/0004-6361/201935656.

[176] J. Thomas et al. "Dynamical modelling of luminous and dark matter in 17 Coma early-type galaxies". In: *MNRAS* 382 (Dec. 2007), pp. 657–684. DOI: 10.1111/j.1365-2966.2007.12434.x. arXiv: 0709.0691.

[177] Jens Thomas et al. "A 17-billion-solar-mass black hole in a group galaxy with a diffuse core". In: *Nature* 532 (Apr. 2016), pp. 340–342. DOI: 10.1038/nature17197.

[178] J. Tonry and M. Davis. "A survey of galaxy redshifts. I - Data reduction techniques". In: *The Astronomical Journal* 84 (Oct. 1979), pp. 1511–1525. DOI: 10.1086/112569.

[179] Roberto Trotta. "Bayes in the sky: Bayesian inference and model selection in cosmology". In: *Contemporary Physics* 49 (Mar. 2008), pp. 71–104. DOI: 10.1080/00107510802066753.

[180] Monica Valluri, David Merritt, and Eric Emsellem. "Difficulties with Recovering The Masses of Supermassive Black Holes from Stellar Kinematical Data". In: *The Astrophysical Journal* 602 (Feb. 2004), pp. 66–92. DOI: 10.1086/380896. arXiv: astro-ph/0210379.

[181] R. C. E. van den Bosch and P. T. de Zeeuw. "Estimating black hole masses in triaxial galaxies". In: *MNRAS* 401 (Jan. 2010), pp. 1770–1780. DOI: 10.1111/j.1365-2966.2009.15832.x. arXiv: 0910.0844 [astro-ph.CO].

[182] R. C. E. van den Bosch and P. T. de Zeeuw. "Estimating black hole masses in triaxial galaxies". In: *MNRAS* 401 (Jan. 2010), pp. 1770–1780. DOI: 10.1111/j.1365-2966.2009.15832.x. arXiv: 0910.0844 [astro-ph.CO].

[183] R. C. E. van den Bosch et al. "Triaxial orbit based galaxy models with an application to the (apparent) decoupled core galaxy NGC 4365". In: *MNRAS* 385 (Apr. 2008), pp. 647–666. DOI: 10.1111/j.1365-2966.2008.12874.x. arXiv: 0712.0113.

[184] Remco C. E. van den Bosch and Glenn van de Ven. "Recovering the intrinsic shape of early-type galaxies". In: *MNRAS* 398 (Sept. 2009), pp. 1117–1128. DOI: 10.1111/j.1365-2966.2009.15177.x. arXiv: 0811.3474 [astro-ph].

[185] Roeland P. van der Marel et al. "Improved Evidence for a Black Hole in M32 from HST/FOS Spectra. II. Axisymmetric Dynamical Models". In: *ApJ* 493 (Jan. 1998), pp. 613–631. DOI: 10.1086/305147. arXiv: astro-ph/9705081 [astro-ph].

[186] Eugene Vasiliev and Monica Valluri. "A new implementation of the Schwarzschild method for constructing observationally-driven dynamical models of galaxies of all morphological types". In: *The Astrophysical Journal* 889 (Jan. 2020), p. 39. DOI: 10.3847/1538-4357/ab5fe0. arXiv: 1912.04288 [astro-ph].

[187] Gerard de Vaucouleurs. "Recherches sur les nebuleuses extragalactiques". In: *Annales d'Astrophysique* 11 (Jan. 1948), p. 247.

[188] Melanie Veale et al. "The MASSIVE Survey - V. Spatially resolved stellar angular momentum, velocity dispersion, and higher moments of the 41 most massive local early-type galaxies". In: *MNRAS* 464 (Jan. 2017), pp. 356–384. DOI: 10.1093/mnras/stw2330. arXiv: 1609.00391 [astro-ph.GA].

[189] Melanie Veale et al. "The MASSIVE Survey - VII. The relationship of angular momentum, stellar mass and environment of early-type galaxies". In: *MNRAS* 471 (Oct. 2017), pp. 1428–1445. DOI: 10.1093/mnras/stx1639. arXiv: 1703.08573 [astro-ph.GA].

[190] Melanie Veale et al. "The MASSIVE survey - VIII. Stellar velocity dispersion profiles and environmental dependence of early-type galaxies". In: *MNRAS* 473 (Feb. 2018), pp. 5446–5467. DOI: 10.1093/mnras/stx2717. arXiv: 1708.00870 [astro-ph.GA].

[191] Melanie Veale et al. "The MASSIVE Survey – V. Spatially resolved stellar angular momentum, velocity dispersion, and higher moments of the 41 most massive local early-type galaxies". In: *Monthly Notices of the Royal Astronomical Society* 464 (Jan. 2017), pp. 356–384. DOI: 10.1093/mnras/stw2330. arXiv: 1609.00391 [astro-ph.GA].

[192] E. K. Verolme et al. "A SAURON study of M32: measuring the intrinsic flattening and the central black hole mass". In: *MNRAS* 335 (Sept. 2002), pp. 517–525. DOI: 10.1046/j.1365-8711.2002.05664.x. arXiv: astro-ph/0201086 [astro-ph].

[193] J. L. Walsh et al. "A Black Hole Mass Determination for the Compact Galaxy Mrk 1216". In: *ApJ* 835, 208 (Feb. 2017), p. 208. DOI: 10.3847/1538-4357/835/2/208. arXiv: 1612.02015.

[194] J. L. Walsh et al. "A Stellar Dynamical Mass Measurement of the Black Hole in NGC 3998 from Keck Adaptive Optics Observations". In: *ApJ* 753, 79 (July 2012), p. 79. DOI: 10.1088/0004-637X/753/1/79. arXiv: 1205.0816.

[195] Thomas K. Waters et al. "A Stellar Dynamical Mass Measurement of the Supermassive Black Hole in NGC 3258". In: *The Astrophysical Journal* 971 (Aug. 2024), p. 149. DOI: 10.3847/1538-4357/ad5a91.

[196] A.-M. Weijmans et al. "The ATLAS ^{3D} project - XXIV. The intrinsic shape distribution of early-type galaxies". In: *MNRAS* 444 (Nov. 2014), pp. 3340–3356. DOI: 10.1093/mnras/stu1603. arXiv: 1408.1099.

[197] Edward L. Wright et al. "The Wide-field Infrared Survey Explorer (WISE): Mission Description and Initial On-orbit Performance". In: *AJ* 140 (Dec. 2010), pp. 1868–1881. DOI: 10.1088/0004-6256/140/6/1868. arXiv: 1008.0031 [astro-ph.IM].

[198] Jianming Ye. "On Measuring and Correcting the Effects of Data Mining and Model Selection". In: *Journal of the American Statistical Association* 93 (1998), pp. 120–131. DOI: 10.1080/01621459.1998.10474094.

[199] Xinyue Alice Zhang et al. June 2024. DOI: 10.48550/arXiv.2406.17754.